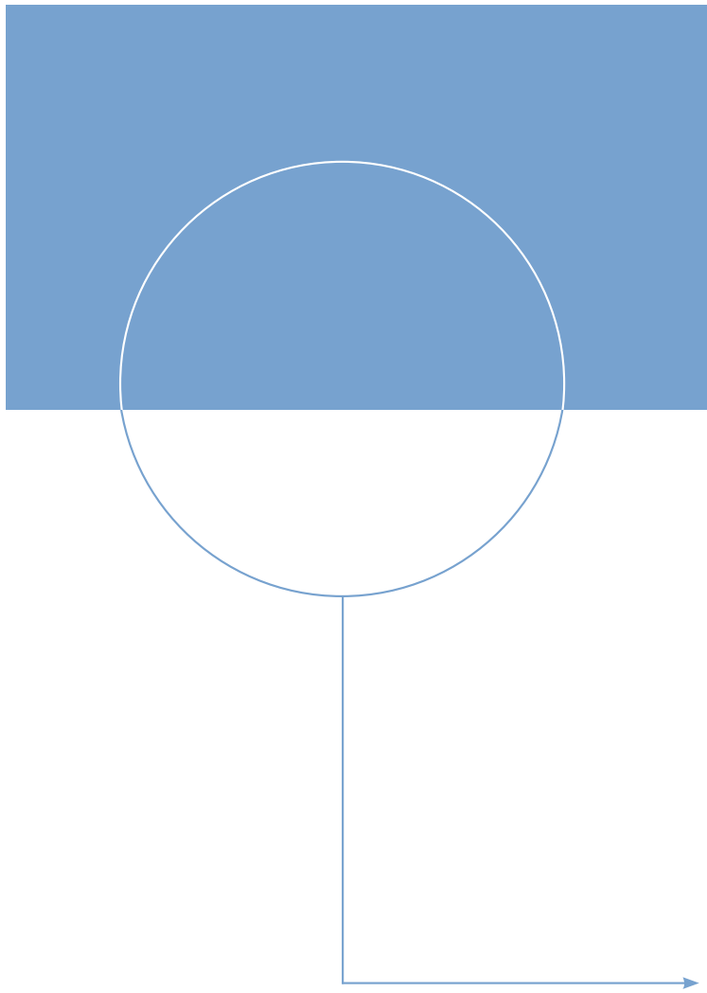

Master's thesis

2019

Kristian Naess

NTNU
Norwegian University of
Science and Technology
Faculty of Natural Sciences
Department of Physics

Kristian Naess

Thermoelectric Properties of (Anti)ferromagnet-Superconductor Hybrid Junctions

June 2019

NTNU
Norwegian University of
Science and Technology

NTNU
Norwegian University of
Science and Technology

NTNU

Norwegian University of
Science and Technology

Thermoelectric Properties of (Anti)ferromagnet-Superconductor Hybrid Junctions

Kristian Naess

MSc in Nanotechnology
Submission date: June 2019
Supervisor: Arne Brataas and Alireza Qaiumzadeh

Norwegian University of Science and Technology
Department of Physics

Abstract

The production of energy is partly responsible for the grave environmental issues the world faces today. Thermoelectric devices, and in particular heat-to-energy converters, are envisioned to have a huge positive impact on the environment by producing energy in a sustainable and non-polluting way. However, the current thermoelectrical devices does not have the necessary energy output and efficiency to compete against more traditional energy production techniques. Therefore, more research into thermoelectric materials is needed to create heat-to-energy converters that can compete in today's market.

This study investigates the thermoelectric properties of both the ferromagnet-superconductor (FS) hybrid junction and the antiferromagnet-superconductor (AS) hybrid junction in order to assess their values as thermoelectric materials, and thereby understand how useful they would be in thermoelectric devices. In the analysis of the FS junction, the thermal conductivity (TC), Seebeck coefficient (SkC) and figure of merit (FOM) are numerically calculated for varying Rashba and Dresselhaus spin-orbit coupling strength, temperature, scalar barrier strength and polarization. A successful realization of the Hamiltonian in matrix form, together with the derivation of eigenvectors and wave functions will serve as a first step toward a more profound understanding of the AS junction.

The study envisions electrons being shot into the (anti)ferromagnet, moving throughout the lattice structure and then hitting the interface between the magnet and superconductor. To mirror the behavior of the electron at the interface, a scalar barrier is included at the junction between the ferromagnet and superconductor. Antiferromagnets and superconductors often have similar lattice structures, and a scalar barrier is thus not taken into consideration for the AS junction. Further, Rashba and Dresselhaus spin-orbit interactions are incorporated in the ferromagnetic case to incorporate spin flipping processes. The mechanisms happening at the interface between the two materials are decisive for the thermoelectric properties of the material composition, and therefore make up a generous part of the calculations. Andreev reflection (AR), normal reflection (NR), tunneling as electron-like quasiparticles (TE), and tunneling as hole-like quasiparticles (TH) make up four possible scattering processes in the model used.

The results showed that AR probability was reduced at higher polarizations, effectively reducing TC. Further, TC was found to increase with increasing temperature, at which the magnitude of the superconducting gap was reduced. In addition, a higher scalar barrier resulted in a greater probability for NR. It should be noticed that the obtained results are in resemblance with the main results in [21], and that certain conditions and material combinations presented promising thermoelectric properties. FOM describes the conversion efficiency of thermoelectric devices,

and the analysis revealed that no spin-orbit coupling, scalar barrier strength $Z = 4$, polarization $P = 0.9$, and normalized temperature $\frac{T}{T_{crit}} \approx 0.4$ gave a FOM of around 5; a number that is considerably larger than what current thermoelectric devices possess. By incorporating both Rashba and Dresselhaus spin-orbit coupling, a figure of merit of 80 was theoretically predicted for a small range of λ_{RSO} values, indicating that very good thermoelectric devices can be made if it is possible to accurately control the ratio of Rashba to Dresselhaus spin-orbit coupling. This is satisfactory as good thermoelectric materials are important in the conversion of waste heat into electrical energy, and hence may have huge environmental significance.

Sammendrag

Denne masteroppgaven undersøker de termiske egenskapene til både en ferromagnet-superleder overgang og en antiferromagnet-superleder overgang. Målet med oppgaven er å utlede, grafisk fremstille og evaluere termisk ledningsevne (TC), Seebeck-koeffisienten (SkC) og godhetstallet (FOM) til disse to overgangene, for å vurdere deres kvalitet som termoelektrisk innretning. I ferromagnettilfellet ser vi på hvordan TC, SkC og FOM blir berørt av en samtidig inkludering av både Rashba- og Dresselhaus spinnbane-vekselvirkning. I antiferromagnettilfellet er det et gap i forskningslitteraturen relatert til oppførselen til Andreev refleksjon, og vi ønsker derfor å undersøke dette nærmere, sammen med en utregning av TC, SkC og FOM for denne materialforbindelsen.

Blonder-Tinkham-Klapwijk formalismen er utnyttet for å finne bølgefunksjonene for både (anti)ferromagneten og superlederen. Videre er grensebetingelser og *NSolve* funksjonen til den matematiske programvaren Mathematica utnyttet for å finne sannsynligheten for fire forskjellige spredningsprosesser; Andreev refleksjon, normal refleksjon, tunneling som elektronlik partikkel og tunneling som hullik partikkel. Disse sannsynlighetene spiller senere en viktig rolle i uttrykkene for TC, SkC og FOM.

Oppgaven viser at sannsynligheten for Andreev refleksjon er lavere desto høyere polarisasjonen er, og dermed vil en høy polarisasjon senke den termiske ledningsevnen. Videre vil termisk ledningsevne øke med økende temperatur, mens det superledende gapet, og dermed sannsynligheten for Andreev refleksjon, vil minske. Resultatene viser også at en større skalar barriere vil øke sannsynligheten for normal refleksjon. Et godt termoelektrisk materiale har et høyt godhetstall, og for ferromagnet-superleder overgangen fikk vi et godhetstall på 5 ved bruk av en skalar barriere $Z = 4$, polarisasjon $P = 0.9$ og normalisert temperatur $\frac{T}{T_{crit}} \approx 0.4$. Dette tallet er betydelig høyere enn hva man kan finne i dagens termoelektriske innretninger. For antiferromagnet-superleder overgangen fant vi Hamiltonian i matriseform, samt egenvektorer og bølgefunksjonene som beskriver partikkeloppførselen i både antiferromagneten og superlederen. Selv om videre forskning er nødvendig for å finne de endelige resultatene for TC, SkC og FOM vil forhåpentligvis utfallet av dette forskningsprosjektet være av stor verdi ved videre analyse av antiferromagnet-superleder overganger.

Preface

This master's thesis concludes a five-year integrated master's degree in Nanotechnology at the Norwegian University of Science and Technology (NTNU). The project is conducted at Center for Quantum Spintronics (QuSpin) under the supervision of Alireza Qaiumzadeh and Arne Brataas. The work presented here is an extension of my project thesis [50] from last semester, and therefore builds on its work. The master's thesis amounts to 30 ECTS credits.

I am grateful to Alireza Qaiumzadeh and Arne Brataas for valuable guidance. Further, I would like to thank Alireza, specifically, for always being helpful, patient and passionate about the work we have done. Our many discussions has taught me a lot about physics during the last two semesters. I would also use the opportunity to thank my family and friends for all support I have got during my five years at NTNU; you have made these years truly wonderful.

Contents

Chapter 1

Introduction

In 1821, Thomas Johann Seebeck discovered heat-to-energy conversion watching a magnetic needle being deflected in close proximity to a circuit made from two dissimilar conductors with junctions held at different temperatures [8]. A few years later, in 1934, Jean Peltier realized that the opposite, energy-to-heat conversion, was also achievable. When passing an electric current through a bimetallic circuit, he observed absorption of heat at one junction and rejection of heat at the other [14]. Today, these two mechanisms make up the thermoelectricity process [43].

With an increasing population that constantly demands more energy, raised attention related to the effect of energy production on today's environmental issues is observed [58, 18]. To cope with these challenges, more and more effort is focused into finding better thermoelectric materials, because such materials can make heat-to-energy converters more effective, increasing the utilization of the vast amounts of easy accessible waste energy in the world.

Three material properties that are important when describing thermoelectric materials are TC, SkC and FOM. TC can be used to describe the superconducting gap in a superconductor, while SkC and FOM are interesting from an application perspective. TC define a material's ability to conduct heat, and SkC describes the open circuit voltage over a junction, created by electron flow due to a thermal gradient. FOM is the ratio of the power extracted from a device to the required power provided to a device to maintain a given temperature difference. A higher FOM will make the conversion efficiency of a thermoelectric device higher [25], and scientists therefore search for material combinations with high FOM, preferably FOM > 1 [29].

It is hypothesized that the (anti)ferromagnet-superconductor hybrid junction can be a good thermoelectric material [21, 33]. At present, the energy cost of cooling down a material to the super-

conducting state is greater than the possible energy gain of utilizing FS based heat-to-electricity converters. However, if scientists are able to realize stable room temperature superconductors in the future, the situation might change. Currently, there are many physicists doing research in that area, and recent findings could indicate that stable room temperature superconductors might be seen earlier than previously thought [38].

The FS junction has gained interest due to an observed increase in thermoelectric effects, including a high calculated FOM [44, 37, 45, 21]. In ferromagnets, there is an asymmetry in the density of states that affects the AR at the interface between the ferromagnet and superconductor. At certain conditions AR will be reduced, resulting in an increased FOM, thereby justifying the junction's extensive publicity. In order to investigate the thermoelectric properties of FS or AS junction, researchers envision a two or three layer material composition. The upper layer is a ferromagnet or antiferromagnet, while the bottom layer is a superconductor. In between these two materials, a scalar barrier can be included to tune the physical parameters and add versatility.

Currently, a study of the FS hybrid junction presents results for the TC, SkC and FOM for the material combination [21]. By varying the Rashba spin-orbit coupling strength, polarization, scalar barrier strength, and temperature it is shown that the FS junction can achieve FOM > 1 under certain conditions. Also the conductance in a FS junction has been investigated along with the AR behaviour under differing polarization, scalar barrier strength, Rashba spin-orbit coupling strength, and Dresselhaus spin-orbit coupling strength [33]. Many aspects of the FS junction is already quite well known, but the simultaneous effect of Rashba and Dresselhaus spin-orbit coupling on the TC, SkC and FOM is yet to be investigated. There is also limited knowledge about the AS junction, and how AR behaves in such a junction. The AR behavior will be crucial in order to calculate TC, SkC and FOM of the AS junction, and thereby assess its quality as a thermoelectric material. Understanding AR behavior could also shine light on the proximity effect in an AS junction and develop the physical understanding of the material composition.

By building on current research and methodologies, this thesis aims to investigate the thermoelectric properties of the (anti)ferromagnet-superconductor hybrid junction to assess its quality as a thermoelectric material. In order to evaluate the FS junction, TC, SkC and FOM will be re-derived, but additional emphasis will be put on the effect of simultaneous Rashba and Dresselhaus spin-orbit coupling. For the AS junction, the objective is to derive the wave function describing the particle behavior in the material, since it is crucial in order to calculate TC, SkC and FOM. The matrix Hamiltonian describing the system plays a vital role in the derivation of the wave function, and obtaining this will therefore be a sub-objective for the thesis. The Hamiltonian will be used to find the eigenvectors and eigenvalues describing the antiferromagnet

and superconductor sides respectively, while the wave function itself will be build up of probability amplitudes, plane waves and eigenvectors. The wave function can be used together with boundary conditions to figure out the probabilities for the scattering processes, as well as TC, SkC and FOM.

The calculations in both the ferromagnetic and antiferromagnetic case are based on the famous Blonder, Tinkham and Klapwijk (BTK) formalism [10], which utilizes theory developed by Nikolay Bogolyubov and Pierre-Gilles deGennes (BdG). Baarden, Cooper and Schrieffer (BCS) theory is a Nobel prized endeavor, describing low temperature superconductivity, that plays an invaluable role in the derivation of the BdG equation. In the BTK formalism, a Hamiltonian is derived from which its eigenvectors are combined with plane waves and probability amplitudes to make a wave function describing particle behavior on both sides of the junction. Utilizing boundary conditions, the probability amplitudes are found, and then multiplied with wave vectors to give the probability for four different scattering processes that can occur at the interface; AR, NR, TE, and TH. These probabilities appear in the expressions for TC, SkC and FOM and are therefore essential in order to understand the junction.

The thesis will start off with an entire chapter dedicated to describe how utilizing the spin degree of freedom opens up a new world of opportunities in the field of spintronics. Thereafter, superconductivity is explained in great detail to build a solid understanding of the phenomenon. Next, the FS and AS hybrid junctions are studied to understand how useful they could be in thermoelectric devices. Further, the results' implications for further research will be discussed and a short summary will proceed in the end.

This master's thesis builds on the work of my project thesis "Thermoelectric Properties of Ferromagnet - Superconductor Hybrid Junctions" [50]. Chapter 1 Introduction, Chapter 2 Spintronics, Chapter 3 Superconductivity, Section 5.1 Schematic Overview of the Junction, Section 4.2 Scattering Mechanisms, and Section 4.4 Blonder-Tinkham-Klapwijk Formalism all originate from the project thesis, and are altered to a varying degree throughout this semester.

Chapter 2

Spintronics

Electronics has played an important role in the development of two of the greatest innovations in the history; the computer and mobile phone. Both these innovations would have rendered impossible without continuous progress in the field of physics. Over the last few decades, scientists have been researching the additional possibilities that the electron spin offers [71, 68]. By controlling the direction of the spin, in addition to the charge of the particle, new opportunities arises. These opportunities are exploited in spintronics; the study and utilization of spin in solid state physics.

The potential of spintronics has been explored in a vast range of research areas. An example of a spintronic device that is currently used is the memory-storage cell, which uses the spin degree of freedom to store data [52]. Another device that may take advantage of the spin is the quantum computer. Instead of using 0's and 1's as the units of information, spin up and spin down could be used. Among the advantages of utilizing this phenomenon is the low energy required to switch between the spin up and spin down state [19].

Quantum mechanics is a field of physics that is essential for the understanding of spintronics. It is made up of the body of scientific laws describing the behavior of particles that make up matter and energy. One of the most important properties of these particles is their spin, which plays a crucial role in magnetism. Another decisive attribute is the angular momentum, which describes the moment of inertia and angular velocity of an object. Together with the spin it shapes the foundation for spin-orbit coupling, an interesting phenomenon in spintronics.

2.1 Quantum Mechanics

Towards the end of the 19^{th} century and the beginning of the 20^{th} century, several physical phenomena had proven impossible to explain using classical mechanics. The most important ones included the photoelectric effect, the spectral lines of the hydrogen atom, Compton scattering, and black-body radiation [54]. All of these phenomena were described as the field of quantum mechanics was established. In 1900, Max Planck solved the black-body radiation problem by stating that the energy of light could only possess certain discrete values [40]. Albert Einstein extended this theory in 1905 by describing the photoelectric effect and introducing the photon [70]. These observations make up parts of the quantum mechanical basis, a basis that has been expanded to explain a broad range of problems that classical mechanics is not able to solve.

Scientists learned that matter can be divided into integer multiples of one quantum, which is the minimum quantity of a physical entity [70]. This discovery made it possible to explain situations that arise in extreme circumstances, such as when dealing with the speed of light or the size of an atom. Circumstances like these are often the subject of advanced research in for example physics, electronics, and materials science.

A quantum system is made up of a small fraction of the world. Each system has its own quantum numbers, telling us about the properties of that particular system. An electron in the hydrogen atom has four quantum numbers: the principal quantum number, the azimuthal quantum number, the magnetic quantum number, and the spin quantum number. The principal quantum number is denoted n and outline the energy of the electron, while the azimuthal quantum number is denoted l and specify the orbital angular momentum of the electron. The azimuthal component of the orientation of orbitals in space is described by the magnetic quantum number, which is denoted m_l. It affects the electron's energy when it is in a magnetic field. The spin quantum number describes the spin of the electron and is denoted m_s. It further indicates the energy, shape and orientation of the orbitals. The electron is an example of a fermion, a particle with half-integer spin that follows Fermi-Dirac statistics. Other fermions include the proton and neutron. Photons are well known examples of bosons. A boson has zero or integer spin and follows Bose-Einstein statistics.

Quantum numbers can be found by solving Schrödinger's equation for the hydrogen atom. In 1926, Erwin Schrödinger derived the equation that describes how a physical system changes over time [3]. The equation is given in one of its most famous forms below,

$$\left[-\frac{\hbar^2}{2m}\nabla^2 + V(\boldsymbol{r},t)\right]\Psi(\boldsymbol{r},t) = E\Psi(\boldsymbol{r},t), \tag{2.1}$$

where $\hbar$ is the reduced Planck constant, m is the particle mass and $V(\boldsymbol{r},t)$ is a nonuniform time dependent potential. Here $\boldsymbol{r} = \begin{bmatrix} x, y, z \end{bmatrix}$, $\Psi(\boldsymbol{r},t)$ is the wave function and E is the energy. A further overview of all the variables used in this thesis can be found in Appendix A. The Schrödinger equation is used to solve various physical situations. The delta potential barrier is such a situation, and is often used to describe physical barriers at the interface between two materials,

$$\delta(z) = \begin{cases} 0, & \text{if } z \neq 0 \\ \infty, & \text{if } z = 0 \end{cases}, \tag{2.2}$$

where z is the position in the $\hat{z}$-direction. The function is by definition normalized over all space: $\int_{-\infty}^{\infty} \delta(z)dz = 1$. Since this thesis investigates the physical situation at the interface between two materials, the delta potential barrier will be decisive when modelling these phenomena. The solution to the Schrödinger equation for the delta potential barrier includes both bound states ($E < 0$) and scattering states ($E > 0$). There will also be a finite probability for reflection off the barrier and transmission through the barrier.

The Schrödinger equation is non-relativistic and describes spinless particles. To describe physical situations even better, a relativistic approach is needed. The Dirac equation is a relativistic wave equation that describes particles with spin $\frac{1}{2}$, such as the electron [59]. The Dirac Hamiltonian can be found below,

$$\mathcal{H}_{Dirac} = c\boldsymbol{g} \cdot (\boldsymbol{p} - e\boldsymbol{A}_v) + hm_e c^2 + eV, \tag{2.3}$$

where c is the speed of light, $\boldsymbol{p}$ is the momentum vector, e is elementary charge, and $\boldsymbol{A}_v$ is the vector potential. Further $h = \begin{bmatrix} I & 0 \\ 0 & -I \end{bmatrix}$ and m_e is the electron rest mass. $\boldsymbol{g} = \begin{bmatrix} 0 & \boldsymbol{\sigma} \\ \boldsymbol{\sigma} & 0 \end{bmatrix}$, where the Pauli spin matrix vector $\boldsymbol{\sigma} = \begin{bmatrix} \sigma_x, \sigma_y, \sigma_z \end{bmatrix}$. The components are given by,

$$\sigma_x = \begin{bmatrix} 0 & 1 \\ 1 & 0 \end{bmatrix}, \sigma_y = \begin{bmatrix} 0 & -i \\ i & 0 \end{bmatrix}, \text{ and } \sigma_z = \begin{bmatrix} 1 & 0 \\ 0 & -1 \end{bmatrix}. \tag{2.4}$$

These Pauli matrices can also be expanded to the 4×4 Pauli spin matrices [31],

$$\tau_x = \begin{bmatrix} 0 & 0 & 1 & 0 \\ 0 & 0 & 0 & 1 \\ 1 & 0 & 0 & 0 \\ 0 & 1 & 0 & 0 \end{bmatrix}, \tau_y = \begin{bmatrix} 0 & 0 & 0 & 1 \\ 0 & 0 & -1 & 0 \\ 0 & -1 & 0 & 0 \\ 1 & 0 & 0 & 0 \end{bmatrix}, \text{ and } \tau_z = \begin{bmatrix} 1 & 0 & 0 & 0 \\ 0 & 1 & 0 & 0 \\ 0 & 0 & -1 & 0 \\ 0 & 0 & 0 & -1 \end{bmatrix}. \quad (2.5)$$

The Hamiltonian in equation 2.3 can be inserted into the Schrödinger equation giving the Dirac equation,

$$i\hbar\frac{\partial\psi}{\partial t} = [c\boldsymbol{g}\cdot(\boldsymbol{p} - e\boldsymbol{A}_v) + hm_ec^2 + eV]\psi. \quad (2.6)$$

Here, ψ is a wave function.

2.2 Spin

All matter is built up of elementary particles. Elementary particles can be divided them into fermions and bosons, where the most prominent difference between them is the spin (s); fermions have half-integer spin while bosons have integer spin. Spin is a measure of a particle's intrinsic angular momentum, the motion about its center of mass. In the case of an electron, $s = \frac{1}{2}$, meaning that an electron has to rotate two complete circles in order to reach the same wave-function again. In accordance with the Pauli exclusion principle, there is usually one electron with spin up ($m_s = \frac{1}{2}$) and one with spin down ($m_s = -\frac{1}{2}$) at the same level in a material. The Pauli exclusion principle states that two electrons cannot have all their quantum numbers equal [27].

For the case of two spin $\frac{1}{2}$ particles, the two can be in a spin triplet state or a spin singlet state, for which their total spin will be either 1 (triplet) or 0 (singlet) dependent on which state they are in. The correspondence between the state and spin of the electron pair is given by,

$$\left\{ \begin{array}{lcc} |11\rangle & = & \uparrow\uparrow \\ |10\rangle & = & \frac{1}{\sqrt{2}}(\uparrow\downarrow + \downarrow\uparrow) \\ |1\bar{1}\rangle & = & \downarrow\downarrow \end{array} \right\} s = 1 \text{ (triplet)} \quad (2.7)$$

and

$$\left\{ \; |00\rangle \quad = \quad \tfrac{1}{\sqrt{2}}(\uparrow\downarrow - \downarrow\uparrow) \; \right\} s = 0 \text{ (singlet)}. \tag{2.8}$$

Spin polarized transport describes a particle current in which the particle spins are aligned in the same direction. A polarized current like this will typically maintain the spin memory for a submicron range distance, the spin diffusion length [30]. By making devices with dimensions smaller than the diffusion length, spin-polarized current is exploited to utilize the spin information and control the spin states. In some situations, a spin polarized current may face a larger barrier if the spins are aligned in one direction rather than another.

Manipulating the spin of particles has been a research topic of high interest lately. Instead of using electrical charges, the particle's spin degree of freedom can be used to convey information. Spin manipulation has proven useful in e.g. quantum computers, encryption protocols and highly sensitive detectors. Devices based on this principle are usually less volatile and have low power consumption [66].

2.3 Magnetism

A phenomenon that is highly dependent on the spin degree of freedom is magnetism. Magnetism cause attractive and repulsive forces, and is due to electrical charges in motion or spin magnetic moments. Every object that produces a magnetic field can be described by a permanent or induced magnetic moment. This moment outline the magnetic strength and direction of the object. The density of these moments is expressed by the magnetization or magnetic polarization. This terminology should be distinguished from the spin polarization P, which is defined as the ratio of the density of states of spin up to spin down electrons at the Fermi level. Usually, the magnetic moments are either a result of motion of electrons in atoms, the spin of the electrons, or the spin of the nuclei. In the case of an external magnetic field or an unbalanced magnetic dipole moment there will often be a net magnetization. This magnetization does not need to be uniform, but can rather vary throughout the material. Mathematically, magnetization is a vector field, but sometimes only the magnitude of the magnetization $M(\boldsymbol{r}) = |\boldsymbol{M}(\boldsymbol{r})|$ is worked with. Together with the magnetic flux density magnitude, the magnetization magnitude plays an important role in the expression for magnetic susceptibility, which is given in SI units as [39],

$$\chi_m(\boldsymbol{r}) = \frac{\mu_{m0} M(\boldsymbol{r})}{B(\boldsymbol{r})}, \tag{2.9}$$

where $\chi_m(\boldsymbol{r})$ is the unitless position dependent magnetic susceptibility, μ_{m0} is the magnetic permeability in vacuum and $M(\boldsymbol{r})$ is a measure for the magnitude of the magnetization at position $\boldsymbol{r}$ with units $\frac{A}{m}$. $B(\boldsymbol{r})$ is the magnetic flux density magnitude $B(\boldsymbol{r}) = |\boldsymbol{B}(\boldsymbol{r})|$ at position $\boldsymbol{r}$, in units of $\frac{A}{m}$.

There are different types of magnetism, such as paramagnetism, diamagnetism, ferromagnetism, and antiferromagnetism among others. Paramagnetic materials have positive susceptibility, while diamagnetic materials have negative magnetic susceptibility. A paramagnetic material will therefore induce an internal magnetic field in the direction of the applied field. For a diamagnetic material an internal magnetic field will be induced in the opposite direction of the applied magnetic field. However, the spin direction of both types of materials will turn random when the applied field is turned off.

Two other types of magnetism is ferromagnetism and antiferromagnetism. Their behavior is described in greater detail by the Heisenberg Hamiltonian for localized electrons represented as [15],

$$\mathcal{H}_H = \frac{1}{2} \sum_{\substack{i,\,j \\ i \neq j}} J_{i,j} \boldsymbol{S}_i \cdot \boldsymbol{S}_j. \tag{2.10}$$

Here, i and j are different electrons, $\boldsymbol{S}_i$ is the spin operator of electron i, and $\boldsymbol{S}_j$ is the spin operator electron j. $\boldsymbol{S}_i \cdot \boldsymbol{S}_j$ is called the exchange interaction, describing the interaction between the spin of electron i and j. $\boldsymbol{S}^2_{i/j}\psi = \hbar^2 s(s+1)\psi$, which connects the spin operators to the spin of the particle. J_{ij} is the exchange constant describing the coupling between electron i and j. From the Heisenberg Hamiltonian, it can be understood that the Heisenberg model is discrete. Only nearest neighbors are considered here, because interactions between these are much stronger than interactions between particles separated by greater distances.

2.3.1 Ferromagnetism

Ferromagnets are known to have a spontaneous magnetic moment, which means that they have a magnetic moment even when there is no applied field. Because of this, it follows that electron

spin and magnetic moment are arranged in a regular manner. There is an energetically favorable magnetization direction called the easy axis, in which ferromagnets prefer to align with. This can be described by looking at the Heisenberg Hamiltonian in equation 2.10. For $J_{ij} < 0$, energy will be minimized with the spins being parallel, and a negative exchange constant is therefore characterizing a ferromagnet. This means that the majority of the lattice sites, which can be seen in Figure 2.1, are filled with particles with the same spin.

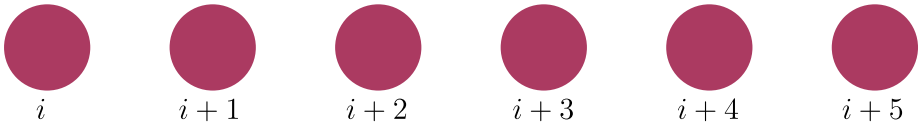

Figure 2.1: A schematic overview of the lattice structure in a ferromagnet. Here, i is an integer, and the burgundy circles are lattice sites, for which the distance between them is a.

In a ferromagnet the density of states for either spin up or spin down will be greater than the other, and thereby give a polarization between 0 and 1 in a ferromagnetic material. Spin up and spin down particles are usually divided into energy subbands, and there are both majority and minority spin subbands [51]. The majority spin subband contains more electrons than the minority and this is the reason for the spin polarization of ferromagnets. For ferromagnets, there will be a partially filled valence band for one spin direction, while for the other spin direction there will be a gap in the density of states. Typically, for very high polarizations, a ferromagnetic material will tend to be highly conductive for either spin up or spin down electrons and behave more like a semiconductor for the other one. In this case, the polarization $P = 1$ and the material is a half-metal, since it possesses both metallic and semiconducting behaviors.

As the Heisenberg Hamiltonian only describes electrons localized on atomic sites, a model describing magnetism arising from itinerant electrons was needed [60]. A well-known model that describes ferromagnetism for itinerant electrons is the Stoner band model, which can be explained in terms of the dispersion relations for spin up and spin down electrons given by [48],

$$E_{\uparrow}(k) = E_0(k) - I\frac{N_{\uparrow} - N_{\downarrow}}{N} \tag{2.11}$$

and

$$E_{\downarrow}(k) = E_0(k) + I\frac{N_{\uparrow} - N_{\downarrow}}{N}. \tag{2.12}$$

Here, $E_0(k)$ is the dispersion relation for spinless electrons, I is the Stoner parameter, $\frac{N_{\uparrow}}{N}$ is

the density of spin up electrons, and $\frac{N_\downarrow}{N}$ is the density of spin down electrons. The second part of these equations is called for the exchange term. An exchange interaction will only happen between identical particles, and can be seen for both bosons and fermions. The energy will be lower when the spins are aligned, favoring ferromagnetism.

Although the energy will be lower if all the spins are aligned, a ferromagnet is not always in the ground state. The way the magnetic moment will align itself depends on the type of material. In the case of an anisotropic material, the magnetic moment will usually align with the easy axis. Any deviations from this direction will result in an energy penalty in accordance with equation 2.13. For an isotropic material there is no energetically preferable direction unless there is an applied magnetic field, which can be seen from [34],

$$E_{pen} = A_s \int (\nabla \boldsymbol{M})^2 dV, \tag{2.13}$$

where A_s is the temperature dependent exchange stiffness constant, $\boldsymbol{M}$ is the uniform magnetization vector, and dV is an incremental volume.

The energy of a ferromagnet is dependent on the difference in direction of the magnetization and the structural axis of the material, which could result from spin-orbit interactions and be described by the anisotropy energy. Often a magnetic material is exposed to an external magnetic field, which will align all the spins in the material and effectively make all the magnetic domains become one.

2.3.1.1 The Ferromagnetic Phase Transition

Minimizing the total energy is one of the most important principles in thermodynamics along with the maximization of entropy [16]. Also crucial to understand thermodynamics is understanding phase transitions. A phase transition describes a change from one phase to another. Different phases often have different properties, and a phase transition can be driven by a change in the thermodynamic properties.

An important phase transition is the ferromagnetic phase transition. This is a ferroic transition in which the transition results in the development of a new macroscopic property that couples to an external field and hence reduce the point-group symmetry. The ferromagnetic phase transition is a second order phase transition, which means that the second order derivatives of the Gibbs free energy are discontinuous. For a first order transition the first order derivatives are discontinuous [55].

A ferromagnetic material will have all its spins aligned in the same direction at $T = 0$, while at high temperatures their spins will be aligned randomly. Hence the material will behave like a ferromagnet below a given temperature and like a paramagnet above that temperature. This temperature is called the Curie temperature T_C. The ferromagnetic phase transition is displayed in Figure 2.2, for which it can be seen that a too high temperature will make the material paramagnetic. An average magnetization of 1 means that all the spins are aligned in the same direction. The average magnetization is given by,

$$\langle \boldsymbol{M} \rangle = \frac{1}{N_p} \sum_{i=1}^{N} \boldsymbol{M}_i, \tag{2.14}$$

where $\boldsymbol{M}_i$ is the magnetization vector of particle i and N_p is the total number of particles. The point of interception on the $\frac{T}{T_C}$ axis is 1, as it is known that a ferromagnet is ferromagnetic for temperatures below the Curie temperature and paramagnetic for higher temperatures [39].

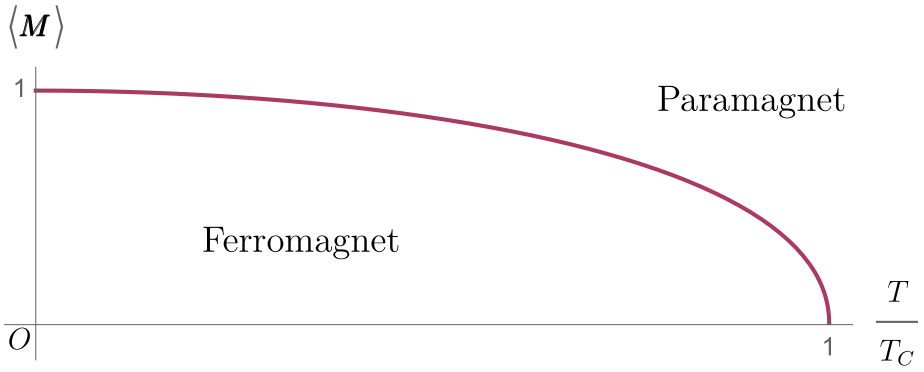

Figure 2.2: The phase transition between a paramagnet and ferromagnet. Here, $\langle \boldsymbol{M} \rangle$ is the average uniform magnetization field vector amplitude, T is the temperature, T_C is the Curie temperature, and O denotes the origin.

2.3.2 Antiferromagnetism

In the case of an antiferromagnet, the spins are ordered in an antiparallel manner, resulting in a zero net magnetic moment at temperatures below the Néel temperature. An antiferromagnetic material is antiferromagnetic when the temperature is below the Néel temperature, and paramagnetic when it is above [39]. Looking at the Heisenberg Hamiltonian in equation 2.10,

it becomes evident that for $J_{i,j} > 0$, the energy will be minimized when the spins follow an antiparallel pattern, resulting in an antiferromagnetic material.

Since the spins are aligned in an antiparallel manner in an antiferromagnet, it is often convenient to work with sublattices. In Figure **??**, the antiferromagnetic sublattice is displayed. There is two different sublattice sites A and B alternating along the lattice. Here, the majority of the particles at one sublattice site has the same spin, while the particles at the other sublattice site has the opposite spin.

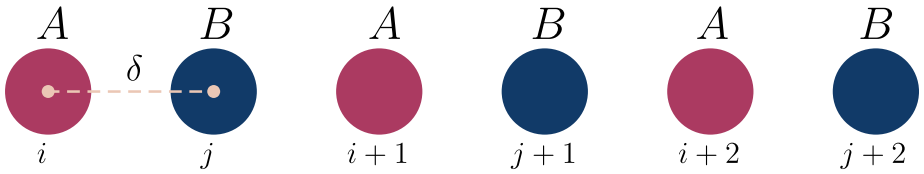

Figure 2.3: A schematic of the sublattice structure in an antiferromagnet. Here, i and j are integers, δ is the distance between two sublattice sites and A and B denote sublattice sites.

2.3.2.1 The Antiferromagnetic Phase Transition

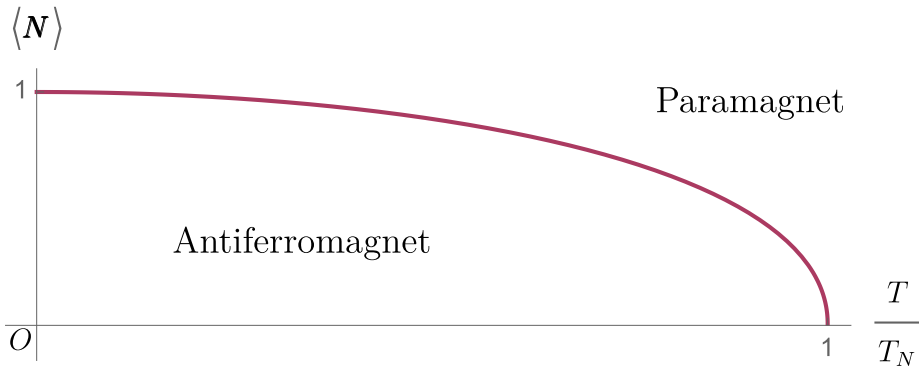

Figure 2.4: The phase transition between a paramagnet and antiferromagnet. Here, $\langle \boldsymbol{N} \rangle$ is the average uniform Néel vector amplitude, T is the temperature, T_N is the Néel temperature, and O denotes the origin.

In an antiferromagnet, the average magnetization vector $\langle \boldsymbol{M} \rangle$ will be zero, and magnetization is therefore not considered a good order parameter in the antiferromagnetic case. Instead the average Néel vector is considered,

$$\langle \boldsymbol{N} \rangle = \frac{1}{N_p} \sum_{i=1}^{N_p} \boldsymbol{N}_i, \tag{2.15}$$

where $\boldsymbol{N}_i = \frac{\boldsymbol{M}_A^i - \boldsymbol{M}_B^i}{|\boldsymbol{M}_A^i - \boldsymbol{M}_B^i|}$. Here A and B are the sublattice sites seen in Figure 2.3, for which an antiferromagnet will have electrons with alternating spin up and spin down. Typically, at $T < T_N$ an antiferromagnet will be antiferromagnetic, while at higher temperatures it will become paramagnetic. This is shown in Figure 2.4.

2.3.3 Practical Applications and Current Research

Magnetism has a wide range of practical applications. Among them are magnetic resonance imaging (MRI), disc drives, compasses, and loudspeakers. It is also a vivid field of research as scientists are investigating 2D magnetism and skyrmions among other things. Skyrmions are chiral magnetic structures where the spins are arranged in whirling configurations. They can be described as topological excitations present in ferromagnets and antiferromagnets among other materials, and can possibly be used in future data storage applications [12].

2.4 Spin-Orbit Coupling

Spin-orbit coupling addresses the interactions between the spin of a particle and its motion. Even without an external field, electrons moving in an electric field will experience a magnetic field in its frame of motion [46]. This spin-orbit field couples to the electron's magnetic moment. By adding the relativistic effects of spin-orbit coupling to the Schrödinger equation, it is possible to study the interactions between spin and orbital angular momentum. Lets look closer at the spin-orbit Hamiltonian given by,

$$\mathcal{H}_{SO} = -\lambda_{vac} \boldsymbol{\sigma} \cdot (\boldsymbol{k} \times \boldsymbol{\nabla} V), \tag{2.16}$$

where $\lambda_{vac} = \frac{e\hbar^2}{4m^2c^2} = 3.7 \times 10^{-6} A^2$, $\boldsymbol{\sigma}$ is the Pauli spin matrix vector, $\boldsymbol{k} = \left[k_x, k_y, k_z\right]$ is the wave vector and V is a potential. Taking a central potential $V = V(r)$, where $r = |\boldsymbol{r}|$ is the distance from the origin, and assuming $\boldsymbol{\nabla} \times \boldsymbol{E}_f = 0$, the Hamiltonian is given by,

$$\mathcal{H}_{SO} = \frac{e\hbar^2}{4m^2c^2}\boldsymbol{\sigma} \cdot (\boldsymbol{E}_f \times \boldsymbol{p}) = \frac{e\hbar(-\frac{1}{r}\frac{dV}{dr})\boldsymbol{\sigma} \cdot (\boldsymbol{r} \times \boldsymbol{p})}{4m^2c^2} = \frac{e}{2m^2c^2}\frac{1}{r}\frac{dV}{dr}\boldsymbol{S} \cdot \boldsymbol{L}. \tag{2.17}$$

Here, $\boldsymbol{S}$ is the spin, $\boldsymbol{L}$ is the angular momentum, m is the particle mass, c is the speed of light, $\boldsymbol{E}_f$ is the electric field, $\boldsymbol{p}$ is the momentum, and $\boldsymbol{r}$ is the position vector. This equation describes a general spin-orbit interaction, an interaction between the spin of a particle ($\boldsymbol{S}$) and its orbital angular momentum ($\boldsymbol{L}$). Two types of spin-orbit interactions are Rashba and Dresselhaus spin-orbit coupling.

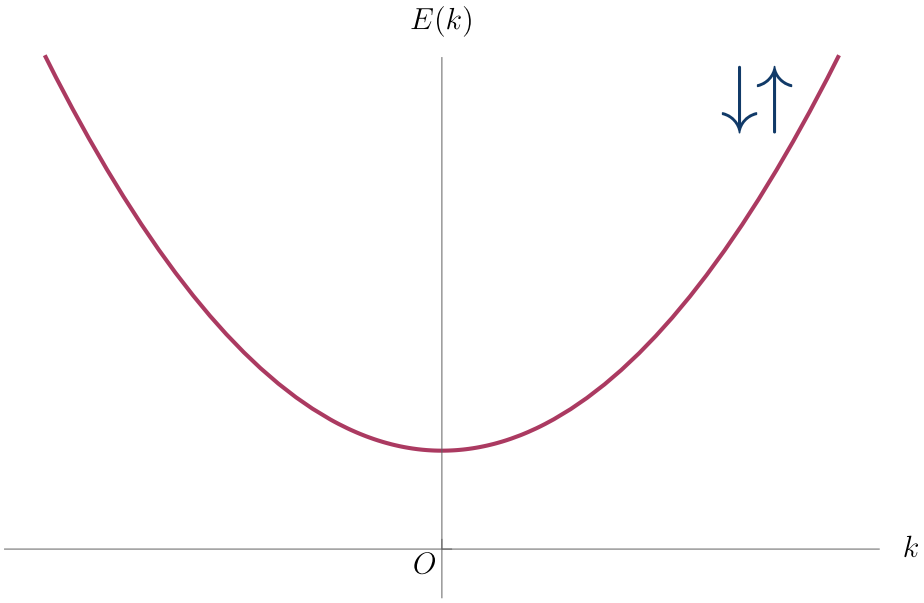

Figure 2.5: The energy band of a material with degenerate spin up and spin down bands. Here, $E(k)$ is the energy at wave vector magnitude $k = |\boldsymbol{k}|$ and O is the origin.

In Figure 2.5 the dispersion relation $E(k)$ of a material that is not exposed for spin-orbit coupling or the Zeeman effect is displayed. Now, lets look closer at how Rashba and Dresselhaus spin-orbit coupling change the dispersion relation in Figure 2.5.

2.4.1 Rashba Spin-Orbit Coupling

In crystals lacking structural inversion symmetry, an energy split in the spin subbands [46] can be observed. Rashba spin-orbit coupling is often seen in heterostructures where the system consists

of multiple layers of different materials. The Rashba Hamiltonian can be written as,

$$\mathcal{H}_R = \lambda_R(k_y\sigma_x - k_x\sigma_y), \tag{2.18}$$

where λ_R is the Rashba spin-orbit coupling constant, $k_y = |\boldsymbol{k}_y|$ is the wave vector amplitude in the $\hat{y}$-direction and $k_x = |\boldsymbol{k}_x|$ is the wave vector amplitude in the $\hat{x}$-direction. Inserting this into the total Hamiltonian for a two-dimensional electron gas (2DEG) confined to the xy-plane and using the spectral theorem, the following is obtained [41],

$$\mathcal{H}_R = \begin{bmatrix} \frac{\hbar^2 k^2}{2m} & \lambda_R(k_y + ik_x) \\ \lambda_R(k_y - ik_x) & \frac{\hbar^2 k^2}{2m} \end{bmatrix}, \tag{2.19}$$

where $k = |\boldsymbol{k}|$. Using Mathematica to diagonalize this matrix and solve for eigenvalues, the dispersion relation is given by,

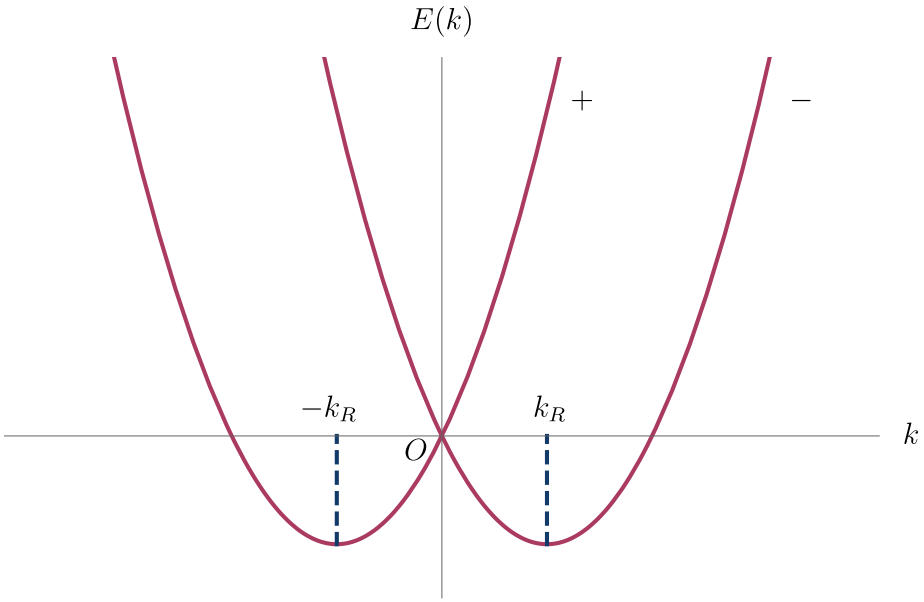

Figure 2.6: The energy band splitting due to Rashba spin-orbit coupling, for which the dispersion relation is rotationally symmetric about the z-axis. Further, k_R is the Rashba wave vector and O denotes the origin.

$$E_{\pm}(k) = \frac{\hbar^2}{2m}(k \pm k_R)^2 - \frac{\hbar^2 k_R^2}{2m}. \tag{2.20}$$

Here, $k_R = \frac{m\lambda_R}{\hbar^2}$ is the Rashba wave vector. Equation 2.20 is displayed in Figure 2.6. In the figure, it can be seen that the Rashba interactions displaced the energy bands in the k-direction. However, they are still degenerate at the origin, meaning that there is no difference between the energies of the electrons in the + and − bands as long as $k = 0$.

2.4.2 Dresselhaus Spin-Orbit Coupling

In 2D, the Dresselhaus Hamiltonian is given by,

$$\mathcal{H}_D = \lambda_D(k_x\sigma_x - k_y\sigma_y), \tag{2.21}$$

where λ_D is the Dresselhaus spin-orbit coupling parameter. The k-linear Dresselhaus term is relevant when the electrons are confined to a 2D semiconductor with bulk inversion asymmetry [65]. Inserting equation 2.21 into the total Hamiltonian for a two-dimensional electron gas (2DEG) the following will be obtained [41],

$$\mathcal{H}_D = \begin{bmatrix} \frac{\hbar^2 k^2}{2m} & \lambda_D(k_x + ik_y) \\ \lambda_D(k_x - ik_y) & \frac{\hbar^2 k^2}{2m} \end{bmatrix}, \tag{2.22}$$

where $k = |\boldsymbol{k}|$. To get the eigenvalues of the matrix, the *Eigensystem* function in Mathematica is used,

$$E_{\pm}(k) = \frac{\hbar^2}{2m}(k \pm k_D)^2 - \frac{\hbar^2 k_D^2}{2m}. \tag{2.23}$$

Here, $k_D = \frac{m\lambda_D}{\hbar^2}$ is the Dresselhaus wave vector. Equation 2.23 is showed in Figure 2.7. Here, the Dresselhaus spin-orbit interactions displaced the energy bands in the k-direction. Still, they are degenerate at the origin, implicating that there is no difference between the energies of the electrons in the + and − bands as long as $k = 0$.

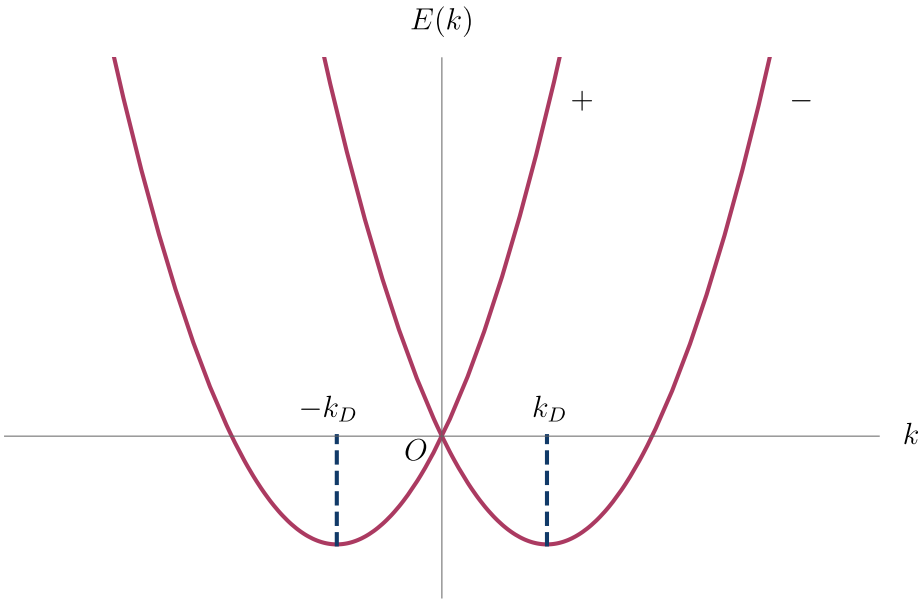

Figure 2.7: The energy band splitting due to Dresselhaus spin-orbit coupling. The dispersion relation is rotationally symmetric about the z-axis, and hence the y-component of the momentum is set to zero. Further, k_D is the Dresselhaus wave vector and O denotes the origin.

2.4.3 Zeeman Effect

The Zeeman effect describes how the energy levels of an atom are shifted when the atom is placed in a uniform external magnetic field. The Hamiltonian of a single electron in a magnetic field is given by [27],

$$\mathcal{H}_Z = -(\boldsymbol{\mu}_l + \boldsymbol{\mu}_s) \cdot \boldsymbol{B}_{ext}, \tag{2.24}$$

where $\boldsymbol{\mu}_l = -\frac{e}{2m}\boldsymbol{L}$, $\boldsymbol{\mu}_s = -\frac{e}{m}\boldsymbol{S}$ and $\boldsymbol{B}_{ext}$ is the external magnetic flux density. Rewriting equation 2.24, an expression for the Zeeman effect can be found as [27],

$$\mathcal{H}_Z = \frac{e}{2m}(\boldsymbol{L} + 2\boldsymbol{S}) \cdot \boldsymbol{B}_{ext}. \tag{2.25}$$

Now, considering an electron in a magnetic field, the Hamiltonian reads,

$$\mathcal{H}_Z = \mu_B B_{ext} \sigma_z, \tag{2.26}$$

where $\mu_B = \frac{e\hbar}{2m}$ and $B_{ext} = |\boldsymbol{B}_{ext}|$. Now, include the kinetic energy term in the Hamiltonian and write it in matrix form as [41],

$$\mathcal{H}_Z = \begin{bmatrix} \frac{\hbar^2 k^2}{2m} + \mu_B B_{ext} & 0 \\ 0 & \frac{\hbar^2 k^2}{2m} - \mu_B B_{ext} \end{bmatrix}, \tag{2.27}$$

giving the dispersion relation,

$$E_{\uparrow\downarrow}(k) = \frac{\hbar^2 k^2}{2m} \pm \mu_B B_{ext}. \tag{2.28}$$

From equation 2.28, it can be seen that the energy bands will be split for spin up and spin down electrons. This is displayed in Figure 2.8.

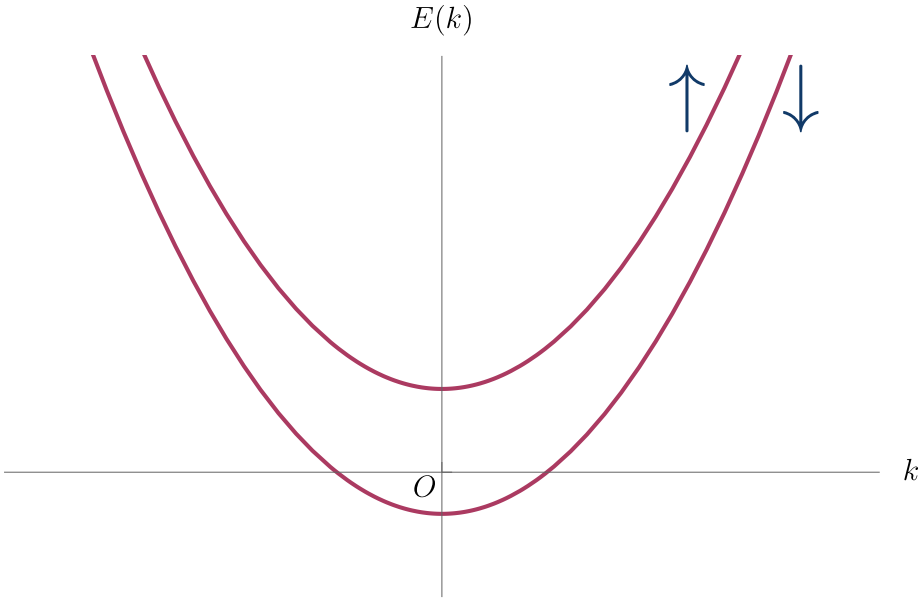

Figure 2.8: The energy band splitting due to the Zeeman effect. Here, O denotes the origin.

2.4.4 Zeeman Effect and Rashba Spin-Orbit Coupling

In Figure 2.8 it is shown that the Zeeman effect will split the energy degeneracy for spin up and spin down particles. Since spin up and spin down still is describing the situation well, the $\hat{z}$-component of the spin is considered a good quantum number. Rashba spin-orbit coupling, on the other hand, will mix spin up and spin down states and break the energy band degeneracy, see Figure 2.6. In this case, the z-component of the spin will not be a good quantum number. For Rashba spin-orbit interactions, the energy minima will be shifted in k value according to $k_R = \pm\frac{\lambda_R m}{\hbar^2}$, where λ_R is a constant describing the strength of the Rashba term in the Hamiltonian.

In Figure 2.9 the Rashba spin-orbit coupling and the Zeeman effect is combined. As can be seen from the graph, the z-component of spin is still not a good quantum number. The graph shows that, in addition to shifting the energy minima away from $k = 0$, an energy gap opens up at $k = 0$.

The figure can be explained by looking at the total Hamiltonian for the system, and consider a 2DEG for our calculations. The Zeeman Rashba Hamiltonian can be obtained as,

$$\mathcal{H}_{ZR} = \frac{\hbar^2 k^2}{2m} + \mu_B B_{ext}\sigma_z + \lambda_R(k_y\sigma_x - k_x\sigma_y). \tag{2.29}$$

In matrix form equation 2.29 becomes,

$$\mathcal{H}_{ZR} = \begin{bmatrix} \frac{\hbar^2 k^2}{2m} + \mu_B B_{ext} & \lambda_R(k_y + ik_x) \\ \lambda_R(k_y - ik_x) & \frac{\hbar^2 k^2}{2m} - \mu_B B_{ext} \end{bmatrix}. \tag{2.30}$$

Using Mathematica to diagonalize and find the eigenvalues of this matrix, the dispersion relation for a 2DEG exposed to both Rashba spin-orbit coupling and Zeeman effect is given by,

$$E_{\pm}(k) = \frac{\hbar^2 k^2}{2m} \pm \sqrt{\mu_B^2 B_{ext}^2 + \lambda_R^2 k^2}. \tag{2.31}$$

From equation 2.31, it can be seen that the equation will be equal to the dispersion relation in the Zeeman case, see equation 2.28, when $k \to 0$. When the external magnetic field $B_{ext} \to 0$ equation 2.31 will be equal to the dispersion relation for the Rashba case, see equation 2.20.

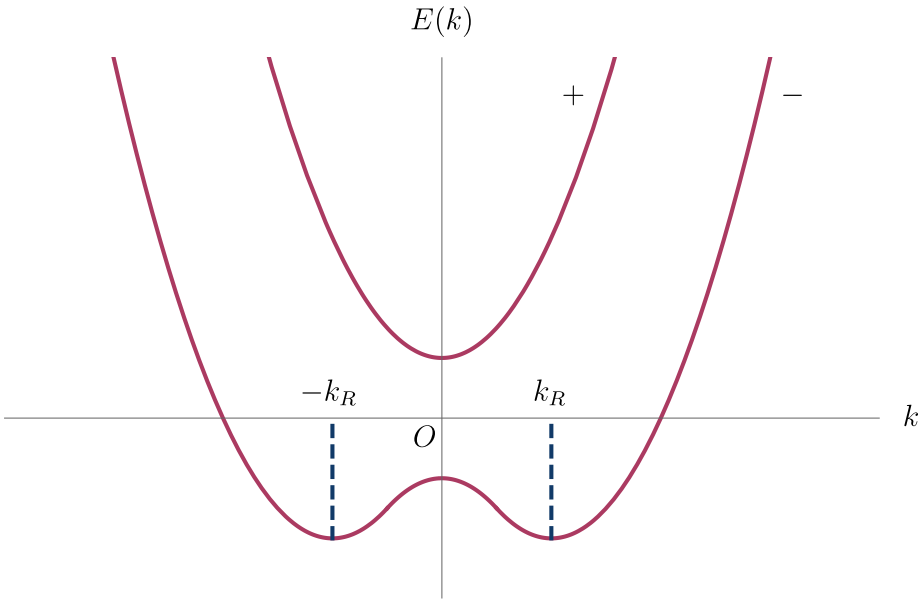

Figure 2.9: The non-degenerate energy bands of a material subject to both the Zeeman effect and Rashba spin-orbit coupling. Here, k_R is the Rashba wave vector and O denotes the origin.

2.5 Scattering

Scattering is an important phenomenon in physics and spintronics. It is defined as the process in which radiation deviate from the acquired straight path. Crucial in spintronics is understanding how the spin degree of freedom affect the electron behavior in physical situations. Scattering is such a situation where the spin might affect the process, as the spin might be flipped during a scattering process.

Two types of scattering are reflection and tunneling. Tunneling is the phenomenon where a particle is transmitted through a barrier that is classically forbidden. To escape a potential barrier V classically, the particle will need more energy than the potential barrier ($E > V$). In quantum mechanics, the particle will be able to escape the barrier with less energy ($E < V$), and this is called tunneling. The probability of escaping increases as the energy increases towards V. Particles have wavelike behavior, which means that when a particle wave encounter a thin barrier, the probability function might extend past the barrier. Because of this, if you send enough, some particles will move past the barrier and appear on the other side. Scanning tunneling microscope (STM) utilizes this principle by tunneling electrons from a tiny STM tip, through the air barrier,

and into the sample. Also some transistors have based their operating principle on tunneling.

In a scattering problem the scientist are usually interested in the amount of a wave that has reflected from or transmitted through a region. The equations explaining this challenge can be ordered into a matrix that is called the scattering matrix. From Figure 2.10, it can be seen that $G = X_{11}K + X_{12}W$ and $U = X_{21}K + X_{22}W$. This set of equations can be ordered into the scattering matrix, which describes the amplitudes of the outgoing waves in terms of the amplitudes of the incoming waves,

$$\begin{bmatrix} G \\ U \end{bmatrix} = \begin{bmatrix} X_{11} & X_{12} \\ X_{21} & X_{22} \end{bmatrix} \begin{bmatrix} K \\ W \end{bmatrix}. \tag{2.32}$$

This thesis is based on a scattering problem in which electrons are shot into a ferromagnet or antiferromagnet. Inside the magnet the electrons will hit ions, dislocations and other obstacles as they scatter their way through the material. When the electron reach the interface it could either be reflected back into the magnet or tunnel through the junction and into the superconductor.

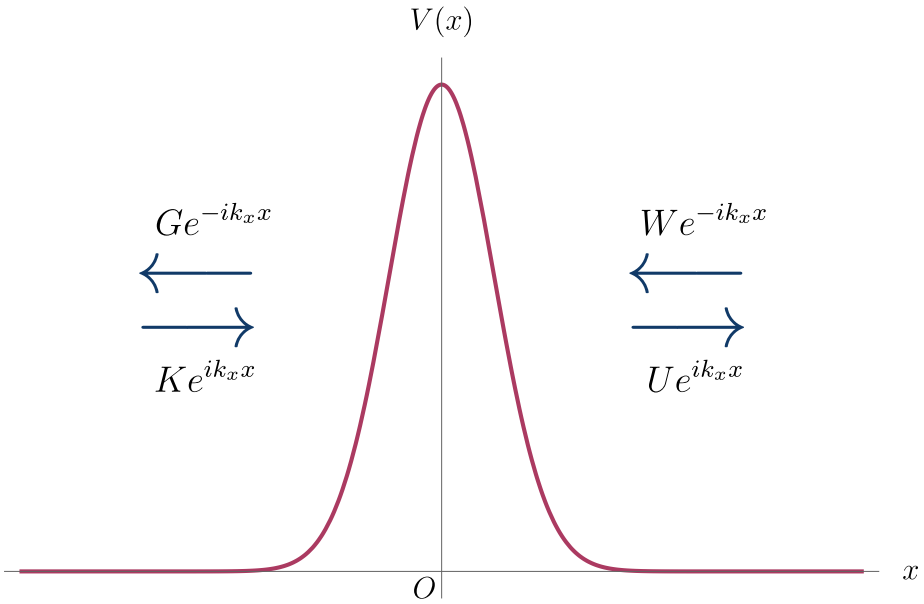

Figure 2.10: The incoming, reflected and transmitted wave functions from a Gaussian potential barrier. Here, G, K, W, and U are wave amplitudes and O is the origin. Depicted from reference [27].

Chapter 3

Superconductivity

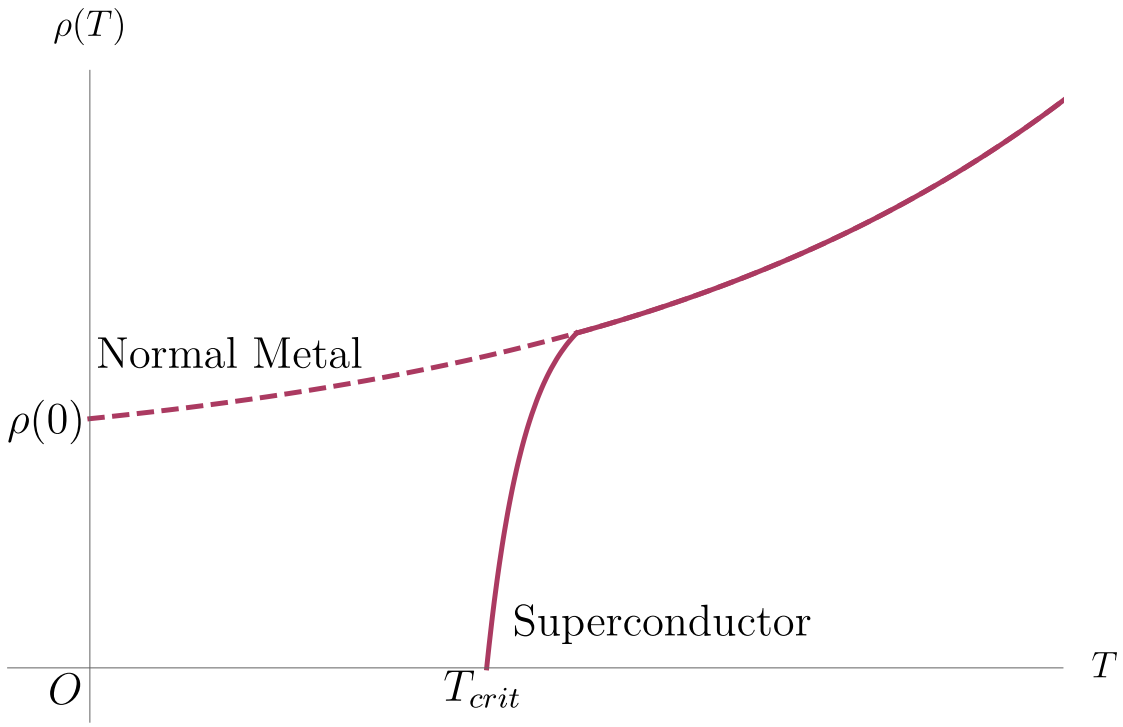

Figure 3.1: A phase diagram showing the resistivity of a superconductor and a metal with varying temperature. Here $\rho(0)$ is the resistivity at $T = 0$, T_{crit} is the critical temperature of the superconductor and O denotes the origin. Depicted from reference [62].

Superconductivity is a thermodynamic state characterized by two distinct phenomena; charged particles can move in a superconducting material with zero electrical resistance (supercurrent) and the material expels magnetic fields. Charged particles can move freely because the resistance suddenly drops to zero when the material is cooled to a very low temperature, see Figure 3.1. A superconductor reaches the superconducting state at temperatures below the critical temperature T_{crit}. The phenomenon was first observed in 1908 by Kamerlingh Onnes, when he realized that the resistivity of mercury fell to zero when the temperature was decreased to 4.1 K [13]. This was contrary to what happened to normal metals where the resistivity decreases with decreasing temperature, but saturates at a finite value at absolute zero. File and Mills have later investigated the decay time of superconductivity in a solenoid, and concluded that it was more than 100 000 years [23].

3.1 Meissner Effect

In 1933, Walther Meissner and Robert Ochsenfeld were measuring magnetic fields in a diverse set of materials. During their experiments, they discovered that the magnetic field approached zero in materials that were cooled down to their superconducting state [56]. This effect was later called the Meissner effect, and is present in all superconductors. It involves a magnetic field bending off the superconducting area, such that everywhere but that area is subject to a magnetic field. The Meissner effect is schematized in Figure 3.2.

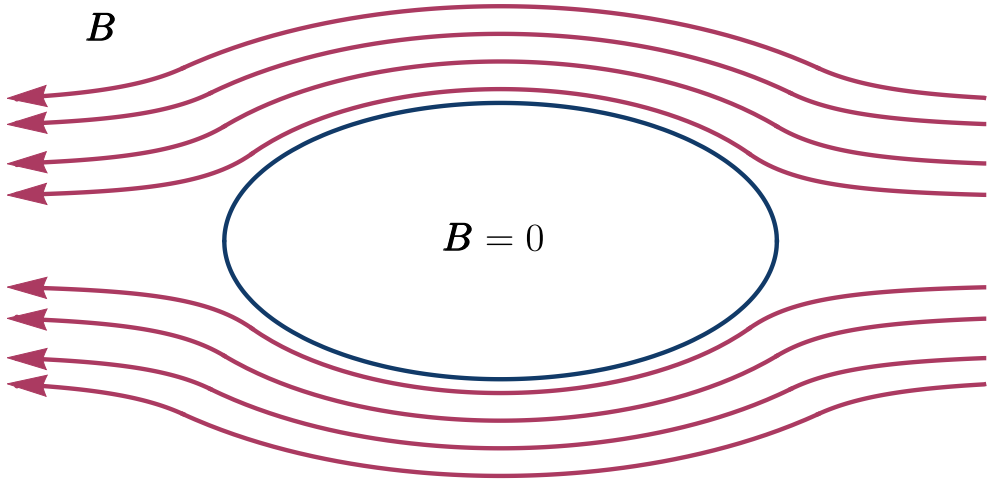

Figure 3.2: The repulsion of a magnetic flux density by a superconductor, also known as the Meissner effect. Depicted from reference [62].

From electromagnetism, it is known that $\boldsymbol{B} = \boldsymbol{H} + 4\pi\boldsymbol{M}$, in which $\boldsymbol{B}$ is the uniform magnetic flux density, $\boldsymbol{H}$ is the uniform magnetic field strength, and $\boldsymbol{M}$ is the uniform magnetization. It can be written $\boldsymbol{M} = \chi_m\boldsymbol{H}$, where χ_m is the magnetic susceptibility. This gives $\boldsymbol{B} = \boldsymbol{H} + 4\pi\chi_m\boldsymbol{H}$ or $\boldsymbol{B} = \mu_m\boldsymbol{H}$. Here, the magnetic permeability is $\mu_m = 1 + 4\pi\chi_m$. The magnetic flux inside a superconductor has to be zero, and hence $\mu_m = 0$ and $\chi_m = -\frac{1}{4\pi}$. From Section 2.3 it is remembered that $\chi_m < 0$ means that the material is diamagnetic. Further, thermodynamic theory explains how zero is the lowest value for the magnetic permeability that is consistent with thermodynamic stability. Hence a superconductor shows perfect diamagnetism. What will be encountered if the magnetization is measured at the surface of the superconductor, when varying the temperature, is that $\boldsymbol{M} = -\frac{\boldsymbol{H}}{4\pi}$ below T_{crit}, and then there will be an abrupt change for higher temperatures. In addition, it is known that a too strong magnetic field will usually be able to destroy the superconductivity, and thereby violate this principle. In other words, there is a critical magnetic field H_{crit}. Similarly, there is a critical current density J_{crit}.

Since electrons are able to move with no resistance in a superconductor, it will be easy for supercurrents to organize on the surface of these materials. When an external magnetic field is applied, these currents will then induce a magnetic field that cancel out the external magnetic field, thereby resulting in zero magnetic field inside a superconductor. There will also be no net magnetization or net current flowing inside a superconducting material in an ideal situation. In reality, there will always be a volume at the surface of the superconductor where there will be a magnetic field. This is described by London theory, which states that the magnetic field decreases exponentially with distance from the surface giving a zero magnetic field in the bulk.

3.2 Types of Superconductors

Superconductors can be classified in different ways. One way of classifying them is into type I and type II, and it has experimentally been shown that the Meissner effect behave differently in these. Type I and type II superconductors will be explained in greater detail in Subsection 3.2.1 and 3.2.2. Another categorization is based on temperature; there are low temperature and high temperature superconductors, for which low temperature superconductors usually have $T_{crit} < 20$ [61]. Further, there is a classification based on the wave function symmetry; the superconductors are divided into s-wave, d-wave and p-wave superconductors. The s-wave superconductor is symmetric and has the shape of s-orbitals. d-wave and p-wave superconductors have the shape of d and p orbitals, respectively.

3.2.1 Type I Superconductors

Type I superconductors are called soft superconductors. They exclude the magnetic field entirely until the field strength suddenly destroys the superconductivity, and the magnetic field penetrates the specimen completely. This is seen in Figure 3.3. Most pure materials are type I superconductors. By adding an alloying element, a type I superconductor can be changed to a type II. A superconductor is type I if the coherence length is longer than the penetration length.

One way to think about this is that whenever a superconductor is in near proximity to a magnetic field, there will be current starting to float at its surface. Since the electrons have no resistance they can move freely. This set up a magnetic field that cancels out the external field. As the external field strength increases the current density will increase and hence also the magnetization. Magnetic field and magnetization are connected via $\boldsymbol{M} = \chi_m \boldsymbol{H}$, and therefore the χ_m can be found for a superconductor by looking at the slope of its $M(H)$ graph. As discussed in Chapter 3 there will also be a critical temperature T_{crit} for which superconductivity is destroyed above. The relationship between critical temperature and critical magnetic field is shown in Figure 3.4.

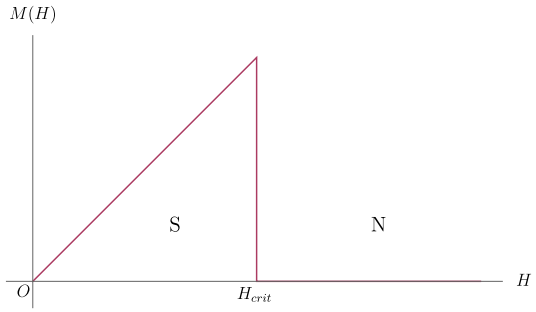

Figure 3.3: The relation between applied magnetic field H and magnetization $M(H)$ for a type I superconductor. The S stands for superconducting phase, while N stand for normal phase. Here, O denotes the origin.

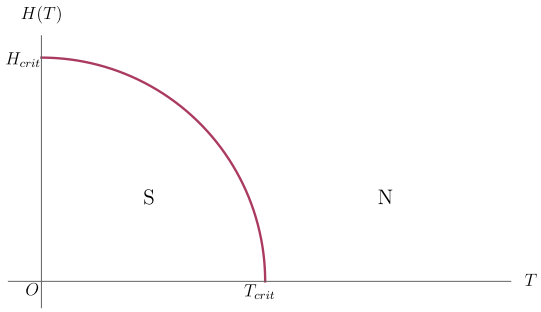

Figure 3.4: The phase transition between a normal metal and type I superconductor. The S stands for superconducting phase, while N stand for normal phase. Here, H_{crit} is the critical field and O is the origin.

3.2.2 Type II Superconductors

Often alloys or transition metals with high resistivity in the normal state, are type II superconductors. In these types of materials small circular vortices, in which the magnetic field can penetrate the material, is present, see Picture 3.1. For low magnetic fields, there is a similar

effect as for type I superconductors. When the magnetic field exceed the lower critical field H_{crit1}, the magnetic flux starts to penetrate into the circular voids. This is called the mixed state. At fields above the upper critical field H_{crit2}, the superconductivity breaks down, just as it does for fields above H_{crit} in the case of a type I superconductor, and this is called the normal state. This behavior is displayed in Figure 3.5, while Figure 3.6 reveals how the superconducting state breaks down at high temperatures and magnetic fields.

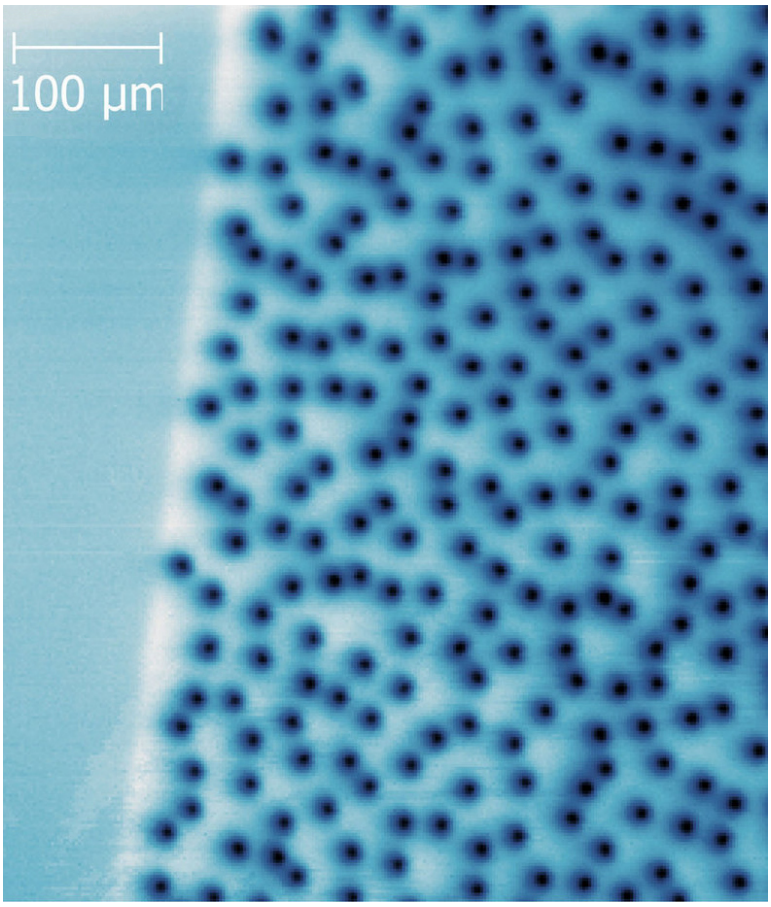

Picture 3.1: The vortices in YBCO, a type II superconductor. © Frederick S. Wells, Alexey V. Pan, X. Renshaw Wang, Sergey A. Fedoseev & Hans Hilgenkamp, CC Wikimedia.

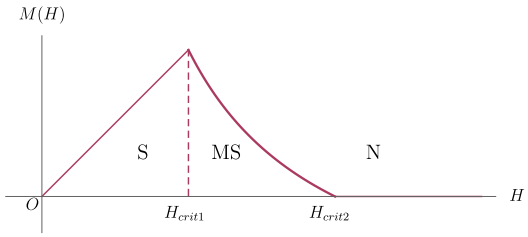

Figure 3.5: The relation between applied magnetic field H and magnetization $M(H)$ for a type II superconductor. The S stands for superconducting phase, MS for mixed state, and N stands for normal phase. Here, O denotes the origin.

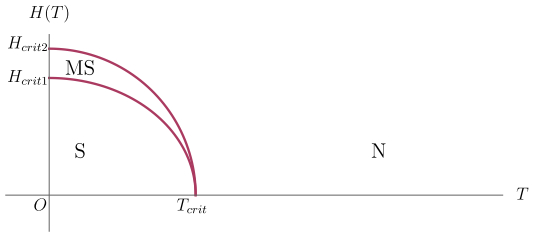

Figure 3.6: The phase transition between a normal metal and type II superconductor. The S stands for superconducting phase, MS for mixed state, and N stand for normal phase. Here, H_{crit1} is the lower critical field, H_{crit2} is the upper critical field and O is the origin.

3.3 Theory of S-Wave Superconductors

3.3.1 BCS Theory

In 1957, John Bardeen, Leon Cooper and Robert Schrieffer laid the foundation for the quantum theory of superconductivity [4]. Their BCS theory have proven very useful when describing low temperature superconductivity in various materials, and resulted in the Nobel Prize in 1972. BCS theory is similar to Hartree-Fock theory for the case when operators that add or remove a pair of fermions develop non-zero expectations.

To derive the BCS Hamiltonian, start by looking at the Hamiltonian for an electron in a superconductor which is given by,

$$\mathcal{H}_{e,S} = -\frac{\hbar^2\nabla^2}{2m} + V_{e-e} + V_{e-i}, \tag{3.1}$$

where V_{e-e} is the electron-electron interactions and V_{e-i} is the electron-ion interactions. Both of these interactions will be positive, as interactions between Cooper pair electrons and free electrons are neglected. V_{e-e} is hence only the internal interaction between electrons in a Cooper pair. Cooper pairs are described in more detail in Subsection 3.3.2. Taking this a step further, the Schrödinger equation for two particles attracted by a positive potential V can be obtained as,

$$\left[-\frac{\hbar^2\nabla^2_{\boldsymbol{r}_1}}{2m_1} - \frac{\hbar^2\nabla^2_{\boldsymbol{r}_2}}{2m_2} + V(\boldsymbol{r}_1 - \boldsymbol{r}_2)\right]\Psi(\boldsymbol{r}_1, \boldsymbol{r}_2) = E\Psi(\boldsymbol{r}_1, \boldsymbol{r}_2), \tag{3.2}$$

where m_1 is the mass of particle 1, m_2 is the mass of particle 2, $\boldsymbol{r}_1$ is the position of particle 1, $\boldsymbol{r}_2$ is the position of particle 2 and $V(\boldsymbol{r}_1 - \boldsymbol{r}_2)$ is a potential between particle 1 and 2. Considering electrons near the Fermi level in a superconductor and developing equation 3.2 further, it can be proved that any attractive potential will result in a bound state between the electrons. This is what a Cooper pair is. In a superconductor there is a superconducting gap and well-defined Fermi surface, which separate occupied states from unoccupied ones. The Cooper pairs are allowed to move inside this superconducting gap, while free electrons will have to be excited across the gap to be able to conduct electricity.

Now, expand equation 3.2 to a many body problem, and look at the mean-field Hamiltonian for

a superconductor (BCS Hamiltonian). This includes interactions between Cooper pair electrons and ions as well as internally in Cooper pairs. Interactions between different Cooper pairs are neglected. The potential between two electrons with momentum $\boldsymbol{k}$ and $\boldsymbol{k'}$ is given by,

$$V_{\boldsymbol{k}\boldsymbol{k'}} = \begin{cases} -V_0, & \text{if } |\xi_{\boldsymbol{k}}| < \hbar\omega_{Dye} \text{ and } |\xi_{\boldsymbol{k'}}| < \hbar\omega_{Dye} \\ 0, & \text{otherwise} \end{cases}, \tag{3.3}$$

where V_0 is a ground state potential, $\xi_{\boldsymbol{k}}$ is the energy of an electron with momentum $\boldsymbol{k}$ and ω_{Dye} is the Debye frequency. The BCS Hamiltonian is given as,

$$\mathcal{H}_{BCS} = \sum_{\boldsymbol{k},\sigma} \xi_{\boldsymbol{k}} c^{\dagger}_{\boldsymbol{k},\sigma} c_{\boldsymbol{k},\sigma} + \frac{1}{N_p} \sum_{\boldsymbol{k},\boldsymbol{k'}} V_{\boldsymbol{k},\boldsymbol{k'}} c^{\dagger}_{\boldsymbol{k},\uparrow} c^{\dagger}_{-\boldsymbol{k},\downarrow} c_{-\boldsymbol{k'},\downarrow} c_{\boldsymbol{k'},\uparrow}, \tag{3.4}$$

where N_p is the number of electrons, $c^{\dagger}_{\boldsymbol{k}\sigma}$ is the creation operator for an electron with spin σ and momentum $\boldsymbol{k}$. Further, $c_{\boldsymbol{k}\sigma}$ is the annihilation operator for an electron with spin σ and momentum $\boldsymbol{k}$ and $V_{\boldsymbol{k},\boldsymbol{k'}}$ is the Coulomb interaction between two electrons with momentum $\boldsymbol{k}$ and $\boldsymbol{k'}$ given by equation 3.3. Only electrons where $|\xi_{\boldsymbol{k}}| < \hbar\omega_{Dye}$ are considered as relevant. This cut-off is because there is a minimum wavelength λ_{Dye} that is sufficient to describe the motion of the ions in the lattice. Correspondingly, there is a maximum frequency for phonon oscillations ω_{Dye}, which is proportional to the number of atoms per volume [39]. In order to solve the BCS Hamiltonian, a set of assumptions and derivations will be needed. First, the superconducting gap $\Delta_{\boldsymbol{k}}$ at momentum $\boldsymbol{k}$ is defined as,

$$\Delta_{\boldsymbol{k}} = -\frac{1}{N_p} \sum_{\boldsymbol{k'}} V_{\boldsymbol{k},\boldsymbol{k'}} \langle c_{-\boldsymbol{k'},\downarrow} c_{\boldsymbol{k'},\uparrow} \rangle, \tag{3.5}$$

where N_p is the number of electrons. This definition will be combined with the ansatz given by,

$$\Delta_{\boldsymbol{k}} = \begin{cases} \Delta > 0, & \text{for } |\xi_{\boldsymbol{k}}| < \omega_{Dye} \\ 0, & \text{otherwise} \end{cases}, \tag{3.6}$$

to simplify the calculations. Further, Nikolay Bogoliubov introduced the Bogoliubov transformation to diagonalize the BCS Hamiltonian [62]. The transformation can be written as,

$$\begin{bmatrix} f_{\boldsymbol{k}\uparrow} \\ \\ f^{\dagger}_{-\boldsymbol{k}\downarrow} \end{bmatrix} = \begin{bmatrix} u^{*}_{\boldsymbol{k}} & -v_{\boldsymbol{k}} \\ \\ v^{*}_{\boldsymbol{k}} & u_{\boldsymbol{k}} \end{bmatrix} \begin{bmatrix} c_{\boldsymbol{k}\uparrow} \\ \\ c^{\dagger}_{-\boldsymbol{k}\downarrow} \end{bmatrix}, \tag{3.7}$$

where $v_{\boldsymbol{k}}$ and $u_{\boldsymbol{k}}$ are complex coefficients, and $f_{\boldsymbol{k}\uparrow}$ and $f^{\dagger}_{-\boldsymbol{k}\downarrow}$ are fermionic operators. To solve the BCS Hamiltonian, also four assumptions will be used:

1. Mean-field approximation
   (a) $QR \approx \langle Q\rangle R + Q\langle R\rangle - \langle Q\rangle\langle R\rangle$
   (b) $Q = c^{\dagger}_{\boldsymbol{k}\uparrow}c^{\dagger}_{-\boldsymbol{k}\downarrow}$
   (c) $R = c_{-\boldsymbol{k}'\downarrow}c_{\boldsymbol{k}'\uparrow}$
2. $\xi_{\boldsymbol{k}} = \xi_{-\boldsymbol{k}}$
3. $|\Delta_{\boldsymbol{k}}| = |\Delta_{-\boldsymbol{k}}|$
4. No interactions between Cooper pairs

Using the previously mentioned assumptions and definitions, equation 3.4 can be rewritten as,

$$\mathcal{H}_{BCS} = \sum_{\boldsymbol{k},\sigma} \xi_{\boldsymbol{k}} c^{\dagger}_{\boldsymbol{k},\sigma} c_{\boldsymbol{k},\sigma} + \sum_{\boldsymbol{k}} (\Delta^{\dagger}_{\boldsymbol{k}} c^{\dagger}_{\boldsymbol{k},\uparrow} c^{\dagger}_{-\boldsymbol{k},\downarrow} + \Delta_{\boldsymbol{k}} c_{-\boldsymbol{k},\downarrow} c_{\boldsymbol{k},\uparrow}), \tag{3.8}$$

where $\xi_{\boldsymbol{k}} = \frac{\hbar^2 k^2}{2m} - \mu_{sc}$. Now, the Bogoliubov transformations from equation 3.7 is used, demanding that $f_{\boldsymbol{k}\uparrow}$ and $f^{\dagger}_{-\boldsymbol{k}\downarrow}$ are fermionic operators following,

$$\{f_i, f^{\dagger}_j\} = f_i f^{\dagger}_j + f^{\dagger}_j f_i = \delta_{i,j}, \text{ and} \tag{3.9}$$

$$\{f^{\dagger}_i, f^{\dagger}_j\} = \{f_i, f_j\} = 0, \tag{3.10}$$

where $f^{\dagger}_{i/j}$ is the creation operator, $f_{i/j}$ is the annihilation operator and $\delta_{i,j}$ is the Kronecker delta given by $\delta_{i,j} = \begin{cases} 1, & \text{if } i = j \\ 0, & \text{if } i \neq j \end{cases}$.

Utilizing equation 3.7 the anticommutation relation is given by,

$$\begin{aligned}\{f_{\boldsymbol{k}\uparrow}, f^{\dagger}_{\boldsymbol{k}\uparrow}\} = f_{\boldsymbol{k}\uparrow}f^{\dagger}_{\boldsymbol{k}\uparrow} + f^{\dagger}_{\boldsymbol{k}\uparrow}f_{\boldsymbol{k}\uparrow} = (u^{*}_{\boldsymbol{k}}c_{\boldsymbol{k},\uparrow} - v_{\boldsymbol{k}}c^{\dagger}_{-\boldsymbol{k},\downarrow})(u_{\boldsymbol{k}}c^{\dagger}_{\boldsymbol{k},\uparrow} - v^{*}_{\boldsymbol{k}}c_{-\boldsymbol{k},\downarrow}) \\ + (u_{\boldsymbol{k}}c^{\dagger}_{\boldsymbol{k},\uparrow} - v^{*}_{\boldsymbol{k}}c_{-\boldsymbol{k},\downarrow})(u^{*}_{\boldsymbol{k}}c_{\boldsymbol{k},\uparrow} - v_{\boldsymbol{k}}c^{\dagger}_{-\boldsymbol{k},\downarrow}) = u^{*}_{\boldsymbol{k}}u_{\boldsymbol{k}}\{c_{\boldsymbol{k},\uparrow}, c^{\dagger}_{\boldsymbol{k},\uparrow}\} + v^{*}_{\boldsymbol{k}}v_{\boldsymbol{k}}\{c_{-\boldsymbol{k},\downarrow}, c^{\dagger}_{-\boldsymbol{k},\downarrow}\} \\ - u^{*}_{\boldsymbol{k}}v^{*}_{\boldsymbol{k}}\{c_{\boldsymbol{k},\uparrow}, c^{\dagger}_{-\boldsymbol{k},\downarrow}\} - v_{\boldsymbol{k}}u_{\boldsymbol{k}}\{c_{-\boldsymbol{k},\downarrow}, c^{\dagger}_{\boldsymbol{k},\uparrow}\} = |u_{\boldsymbol{k}}|^2 + |v_{\boldsymbol{k}}|^2 = 1,\end{aligned} \tag{3.11}$$

where the anticommutation relations in equation 3.9 and 3.10 are used. To proceed in the derivation of $u_{\boldsymbol{k}}$ and $v_{\boldsymbol{k}}$, exchange $c_{\boldsymbol{k},\uparrow}$ and $c_{-\boldsymbol{k},\downarrow}$ in the Hamiltonian with their fermionic counterparts $f_{\boldsymbol{k},\uparrow}$ and $f_{-\boldsymbol{k},\downarrow}$,

$$\begin{bmatrix} c_{\boldsymbol{k}\uparrow} \\ \\ c^{\dagger}_{-\boldsymbol{k}\downarrow} \end{bmatrix} = \begin{bmatrix} u_{\boldsymbol{k}} & v_{\boldsymbol{k}} \\ \\ -v^{*}_{\boldsymbol{k}} & u^{*}_{\boldsymbol{k}} \end{bmatrix} \begin{bmatrix} f_{\boldsymbol{k}\uparrow} \\ \\ f^{\dagger}_{-\boldsymbol{k}\downarrow} \end{bmatrix}. \tag{3.12}$$

Now, utilize the transformation in equation 3.12 to write the Hamiltonian in terms of $f_{\boldsymbol{k}\uparrow}$ and $f^{\dagger}_{-\boldsymbol{k}\downarrow}$,

$$\begin{aligned}\mathcal{H}_{BCS} = \sum_{\boldsymbol{k}}[&(\xi_{\boldsymbol{k}}|u_{\boldsymbol{k}}|^2 - \xi_{\boldsymbol{k}}|v_{\boldsymbol{k}}|^2 - \Delta^{*}_{\boldsymbol{k}}u_{\boldsymbol{k}}v_{\boldsymbol{k}} - \Delta_{\boldsymbol{k}}u^{*}_{\boldsymbol{k}}v^{*}_{\boldsymbol{k}})f^{\dagger}_{\boldsymbol{k},\uparrow}f_{\boldsymbol{k},\uparrow} \\ &+ (\xi_{\boldsymbol{k}}|u_{\boldsymbol{k}}|^2 - \xi_{\boldsymbol{k}}|v_{\boldsymbol{k}}|^2 - \Delta^{*}_{\boldsymbol{k}}u_{\boldsymbol{k}}v_{\boldsymbol{k}} - \Delta_{\boldsymbol{k}}u^{*}_{\boldsymbol{k}}v^{*}_{\boldsymbol{k}})f^{\dagger}_{-\boldsymbol{k},\downarrow}f_{-\boldsymbol{k},\downarrow} \\ &+ (\xi_{\boldsymbol{k}}u^{*}_{\boldsymbol{k}}v_{\boldsymbol{k}} + \xi_{\boldsymbol{k}}u^{*}_{\boldsymbol{k}}v_{\boldsymbol{k}} - \Delta^{*}_{\boldsymbol{k}}v^{2}_{\boldsymbol{k}} + \Delta_{\boldsymbol{k}}u^{*2}_{\boldsymbol{k}})f^{\dagger}_{\boldsymbol{k},\uparrow}f^{\dagger}_{-\boldsymbol{k},\downarrow} \\ &+ (\xi_{\boldsymbol{k}}u^{*}_{\boldsymbol{k}}v_{\boldsymbol{k}} + \xi_{\boldsymbol{k}}u^{*}_{\boldsymbol{k}}v_{\boldsymbol{k}} - \Delta^{*}_{\boldsymbol{k}}v^{2}_{\boldsymbol{k}} + \Delta_{\boldsymbol{k}}u^{*2}_{\boldsymbol{k}})f_{-\boldsymbol{k},\downarrow}f_{\boldsymbol{k},\uparrow}].\end{aligned} \tag{3.13}$$

By comparing this expression to the superconducting matrix in equation 4.28, it is realized that,

$$2\xi_{\boldsymbol{k}}u^{*}_{\boldsymbol{k}}v_{\boldsymbol{k}} - \Delta^{*}_{\boldsymbol{k}}v^{2}_{\boldsymbol{k}} + \Delta_{\boldsymbol{k}}v^{*2}_{\boldsymbol{k}} = 0. \tag{3.14}$$

Next, assume that $u_{\boldsymbol{k}}$, $v_{\boldsymbol{k}}$ and $\Delta_{\boldsymbol{k}}$ are real,

$$u_{\boldsymbol{k}} = |u_{\boldsymbol{k}}|e^{io},\ v_{\boldsymbol{k}} = |v_{\boldsymbol{k}}|e^{it}, \text{ and } \quad \Delta_{\boldsymbol{k}} = |\Delta_{\boldsymbol{k}}|e^{iw}, \tag{3.15}$$

where $o = t = w = 0$. Using this, equation 3.14 can further be developed to,

$$2\xi_{\boldsymbol{k}}|u_{\boldsymbol{k}}||v_{\boldsymbol{k}}| - |\Delta_{\boldsymbol{k}}|(|v_{\boldsymbol{k}}|^2 - |u_{\boldsymbol{k}}|^2). \tag{3.16}$$

Now, segment the two terms on each side of the equal sign and square,

$$4\xi_{\boldsymbol{k}}^2|u_{\boldsymbol{k}}|^2|v_{\boldsymbol{k}}|^2 = |\Delta_{\boldsymbol{k}}|^2(|v_{\boldsymbol{k}}|^2 - |u_{\boldsymbol{k}}|^2)^2. \tag{3.17}$$

Further, adding $4|\Delta|^2|u_{\boldsymbol{k}}|^2|v_{\boldsymbol{k}}|^2$ on both sides to get $(|v_{\boldsymbol{k}}|^2+|u_{\boldsymbol{k}}|^2)^2$ on the right side, the equation becomes,

$$4(\xi_{\boldsymbol{k}}^2 + |\Delta_{\boldsymbol{k}}|^2)|u_{\boldsymbol{k}}|^2|v_{\boldsymbol{k}}|^2 = |\Delta_{\boldsymbol{k}}|^2(|v_{\boldsymbol{k}}|^2 + |u_{\boldsymbol{k}}|^2)^2, \tag{3.18}$$

which again can be rewritten as,

$$4(\xi_{\boldsymbol{k}}^2 + |\Delta_{\boldsymbol{k}}|^2)|u_{\boldsymbol{k}}|^2|v_{\boldsymbol{k}}|^2 = |\Delta_{\boldsymbol{k}}|^2. \tag{3.19}$$

Rearranging the terms, it can be shown that,

$$|u_{\boldsymbol{k}}||v_{\boldsymbol{k}}| = \frac{|\Delta_{\boldsymbol{k}}|}{2\sqrt{(\xi_{\boldsymbol{k}}^2 + |\Delta_{\boldsymbol{k}}|^2)}}. \tag{3.20}$$

Inserting this into equation 3.17 gives,

$$|v_{\boldsymbol{k}}|^2 - |u_{\boldsymbol{k}}|^2 = \frac{\xi_{\boldsymbol{k}}}{\sqrt{(\xi_{\boldsymbol{k}}^2 + |\Delta_{\boldsymbol{k}}|^2)}}. \tag{3.21}$$

Now, combine equation 3.11 and 3.21 to get the final expression for the superconducting coherence factors $u_{\boldsymbol{k}}$ and $v_{\boldsymbol{k}}$,

$$|u_{\boldsymbol{k}}| = \sqrt{\frac{1}{2}(1 + \frac{\xi_{\boldsymbol{k}}}{\sqrt{\xi_{\boldsymbol{k}}^2 + \Delta_{\boldsymbol{k}}^2}})} \tag{3.22}$$

and

$$|v_{\boldsymbol{k}}| = \sqrt{\frac{1}{2}(1 - \frac{\xi_{\boldsymbol{k}}}{\sqrt{\xi_{\boldsymbol{k}}^2 + \Delta_{\boldsymbol{k}}^2}})}. \tag{3.23}$$

By inserting these expressions into equation 3.13, the Hamiltonian is given by,

$$\mathcal{H}_{BCS} = \sum_{\boldsymbol{k},\sigma} E_{\boldsymbol{k}} f^{\dagger}_{\boldsymbol{k},\sigma} f_{\boldsymbol{k},\sigma}, \tag{3.24}$$

where,

$$E_{\boldsymbol{k}} = \upsilon \sqrt{\xi_{\boldsymbol{k}}^2 + |\Delta_{\boldsymbol{k}}|^2}, \tag{3.25}$$

are the eigenvalues and $\upsilon = \pm 1$.

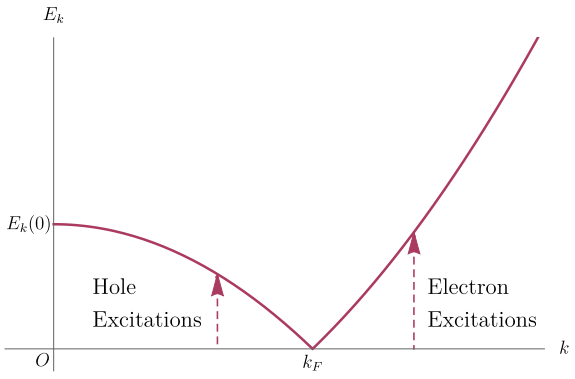

Figure 3.7: The dispersion relation for Bogoliubov quasiparticles, $E_{\boldsymbol{k}} = |\xi_{\boldsymbol{k}}|$. This is for a parabolic $\xi_{\boldsymbol{k}}$. Here k_F is the Fermi wave vector and O is the origin. Depicted from reference [62].

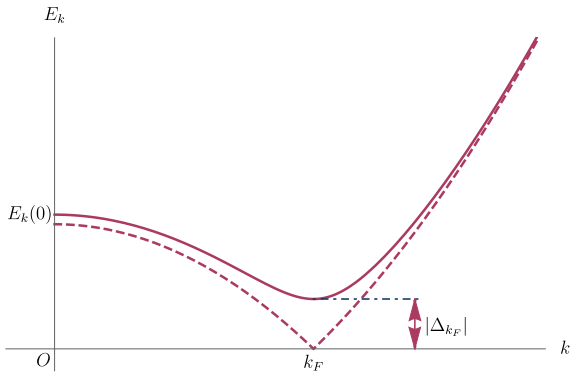

Figure 3.8: The dispersion relation for Bogoliubov quasiparticles, changed for superconductivity. $E_{\boldsymbol{k}} = \sqrt{\xi_{\boldsymbol{k}}^2 + |\Delta_{\boldsymbol{k}}|^2}$. This is for a parabolic $\xi_{\boldsymbol{k}}$. Here k_F is the Fermi wave vector and O is the origin. Depicted from reference [62].

First, lets look at the expressions in the normal metal limit $\Delta_{\boldsymbol{k}} = 0$,

$$\begin{cases} |u_{\boldsymbol{k}}|^2 = \frac{1}{2}(1 + \frac{\xi_{\boldsymbol{k}}}{|\xi_{\boldsymbol{k}}|}) = \begin{cases} 0 & \text{if } \xi_{\boldsymbol{k}} < 0 \text{ (h)} \\ 1 & \text{if } \xi_{\boldsymbol{k}} > 0 \text{ (e)} \end{cases} \\ |v_{\boldsymbol{k}}|^2 = \frac{1}{2}(1 - \frac{\xi_{\boldsymbol{k}}}{|\xi_{\boldsymbol{k}}|}) = \begin{cases} 1 & \text{if } \xi_{\boldsymbol{k}} < 0 \text{ (h)} \\ 0 & \text{if } \xi_{\boldsymbol{k}} > 0 \text{ (e)} \end{cases} \end{cases}, \tag{3.26}$$

from which it is understood that $u_{\boldsymbol{k}}$ denotes electron-like solutions and $v_{\boldsymbol{k}}$ denotes hole-like solutions. The results for the dispersion relation is schematized in Figure 3.7 and 3.8 for which $k = |\boldsymbol{k}|$.

As can be seen from Figure 3.7 it costs energy to create a hole in the Fermi sea and insert an electron into an empty state outside of the Fermi sea. The Fermi sea is the area to the left of k_F in Figure 3.7 and 3.8. In Figure 3.8 it can be observed that superconductivity creates an energy gap in the dispersion relation. In other words, the ground state is separated from excited states by a superconducting gap at the Fermi level. The critical magnetic field, thermal properties and most of the electromagnetic properties of a superconductor are highly dependent on the gap.

In order to investigate the superconducting gap further, insert the Bogoliubov transformations from equation 3.7 into equation 3.5. Further, assume a k-independent real gap and that the density of states is constant close to the Fermi energy to arrive at [62],

$$1 = V_0 D(E_F) \int_{-\omega_D}^{\omega_D} d\xi \frac{\tanh \frac{\beta}{2}\sqrt{\xi^2 + \Delta^2}}{2\sqrt{\xi^2 + \Delta^2}}, \tag{3.27}$$

where $D(E_F)$ is the density of states at the Fermi energy and $\beta = \frac{1}{k_B T}$. If this is evaluated numerically an expression for the superconducting gap for different temperatures will be obtained. This expression is displayed in Figure 3.9. Here, it can be observed that the gap decreases as the critical temperature of the superconductor is approached.

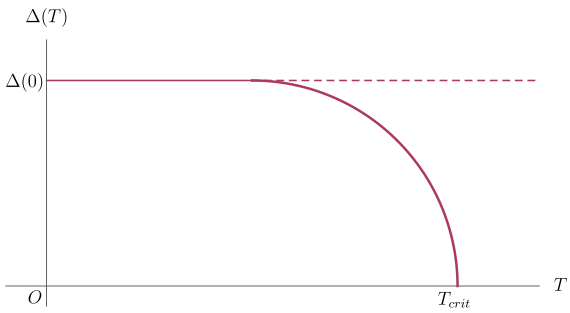

Figure 3.9: The superconducting gap under varying temperature. Here, $\Delta(T)$ is the superconducting gap at temperature T, $\Delta(0)$ is the superconducting gap at $T = 0$, T_{crit} is the critical temperature and O is the origin. Depicted from reference [62].

3.3.2 Cooper Pairs

When a superconducting material is cooled down to below T_{crit}, a fraction of the particles are observed in the same quantum state. This fraction is built up of electron pairs, so-called Cooper pairs. The electrons in a Cooper pair have opposite momentum and either parallel or antiparallel spin, giving a total spin of 0 or 1. These electron pairs are therefore composite bosons that do not have to obey the Pauli exclusion principle.

When an electron move in a lattice there will be attractive forces between it and the positive ions in the material, dislocating the ions slightly. The heavier the ion, the less the deformation of the lattice, see Figure 3.10. Later, the other electron in the Cooper pair will approach the same ions and experience attractive forces. This electron will take advantage of the deformed lattice to lower its energy [39], and therefore it will be energetically favorable for electrons to pair up as Cooper pairs. Since the position of the ions are dependent on the interactions with the first electron, there will be a connection between the electrons through lattice deformation. The electrons do not have to be extremely close to each other in order to experience this electron-lattice-electron interaction. Within the radius of a Cooper pair (approximately 1 µm) there are about 10^6 Cooper pairs [11]. Even a small attraction between two electrons will cause a paired state of the electrons to have energy $E < E_F$, meaning that the electrons are bound.

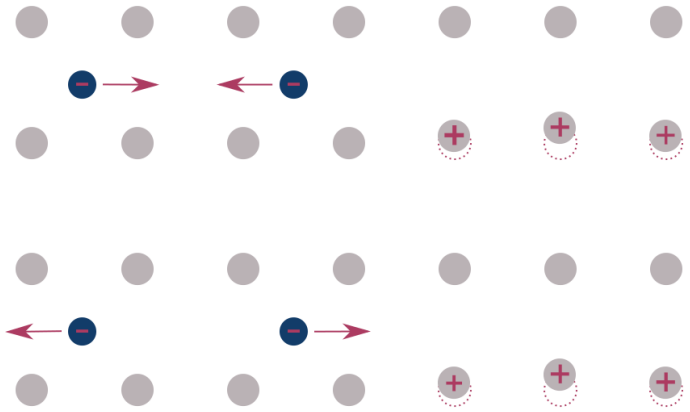

Figure 3.10: The Cooper pair effect on ions in the lattice. The blue circles are the electrons, while the grey circles are the positive ions.

Chapter 4

Ferromagnet-Superconductor Hybrid Junction

New and improved thermoelectric materials is and will be important in applications related to cooling, heating, electric power generation and hybrid applications [63]. With increased attention to environmental issues, improving recovery of waste heat energy has become a goal of numerous companies around the world. Thermoelectric materials will play an important role in the devices that are made with this objective, because of their abilities to convert heat to energy [9]. A selection of other possible applications for thermoelectric materials include heat recovery from vehicles, cooling electronic devices and thermo-photovoltaic cells.

In ferromagnets there is an asymmetry in the density of states; more electrons are aligned with their spin in one direction than the opposite. This affect AR [35] at the interface between a ferromagnet and a superconductor, and is a vital reason for why FS hybrid junctions have generated considerable research interest lately. Scientists have also observed a boost in thermoelectric effects, making the FS junction suitable for thermal transport [21].

Two other interesting phenomena in the FS junction is the oscillatory behavior of the superconducting pair amplitude and fermionic Majorana states. Evidence of the damping oscillatory behavior of the superconducting pair amplitude inside the ferromagnet is the 0-π transition, which can be seen in for example an SFS Josephson junction [1], and be utilized in quantum and digital circuits [22]. Fermionic Majorana states is a non-trivial effect that has been rumoured to happen at the interface between a superconductor and ferromagnet [20]. A Majorana fermion is a fermion that is its own antiparticle, and can, because of the non-abelian statistics they obey, potentially be used in topological quantum computers [57].

The tight binding model of the FS introduced in Subchapter 4.3 incorporates Rashba spin-orbit interactions. This is crucial for spin-flipping processes to occur at the interface. Spin manipulation is interesting because effects from spin splitting and spin polarized transport could enhance the thermal properties of a FS junction among other things. To assess the thermoelectric properties of the FS junction, TC, SkC and FOM will be calculated. TC describes a material's ability to transfer heat. SkC is the open circuit voltage developed over the junction due to electron flow caused by a thermal gradient. Finally, FOM is the power that will have to be provided to maintain a temperature difference across a material. Developing a material with high SkC and FOM can help making next-century's heat to energy converters.

4.1 Schematic Overview of the Junction

In this section the thermoelectric properties of the FS hybrid junction will be investigated. The model of the FS junction is schematized in Figure 4.1 with $z = 0$ at the interface between the ferromagnet and superconductor. To calculate TC, FOM and SkC of this FS junction, a tight binding model and modified BTK theory will be utilized.

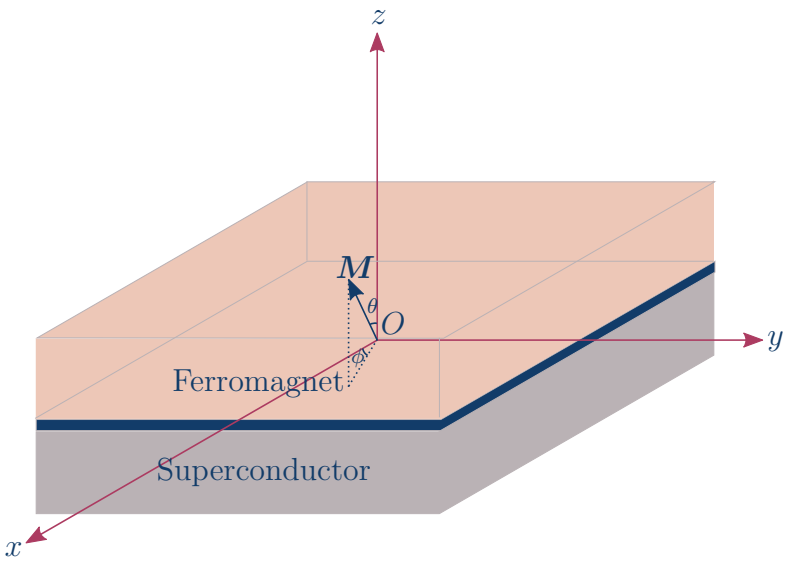

Figure 4.1: The model of the FS junction used in the calculations. Here, θ is the polar angle, ϕ is the azimuthal angle and O is the origin. Depicted from reference [33].

4.2 Scattering Mechanisms

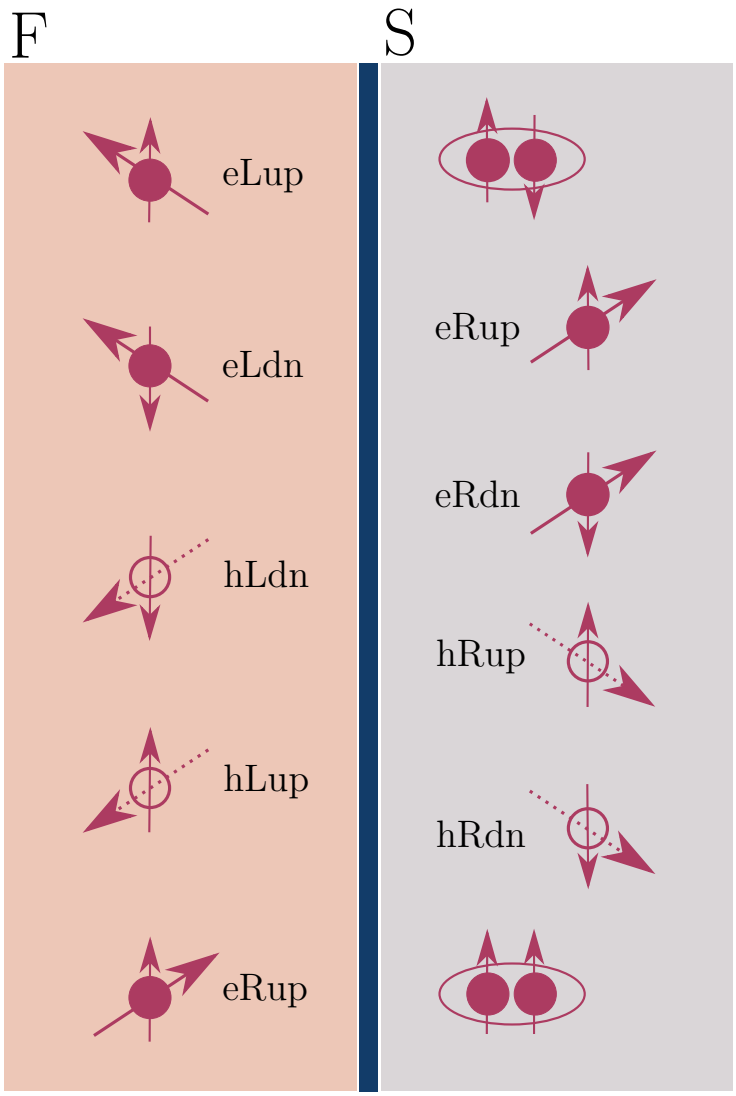

Figure 4.2: The possible scattering mechanisms in a FS hybrid structure. Here, e stand for electron and h for hole. L means that the particle is moving to the left, while R means that it moves to the right. Further, up means that the particle has spin up, and dn means that the particle has spin down. Depicted from reference [21, 33].

In order to understand the quality of the FS junction as a thermoelectric material, electrons are shot into the ferromagnet in the $-\hat{z}$-direction. The electrons will move throughout the ferromagnet and strike the interface between the ferromagnet and superconductor, where four different scattering processes can happen; AR, NR, TE, and TH. All these processes are shown in Figure 4.2, where eRup is the incoming electron in all four situations.

During AR, quasiparticle current in the normal state material is converted into supercurrent in the superconductor; one electron approaches the interface, two electrons will be transferred through the junction, and a hole is reflected back from the barrier in the same direction the electron came from. This is explained in Figure 4.2 where eRup on the ferromagnetic side is the incoming electron, hLup is the reflected hole and the Cooper pair is drawn as two solid circles inscribed inside an elliptical circle. Looking at the energy conservation, $E_{e,k} = E_{h,k} + 2\mu$ [10]. Here $E_{e,k}$ is the energy of an electron with momentum k, $E_{h,k}$ is the energy of a hole with momentum k and μ is the chemical potential. From this it follows that $|E_e| = |E_h|$, the hole is generated as far away from the chemical potential as the electron was. A similar type of reflection is the spin flip Andreev reflection (SAR). A SAR process is identical to an AR, but the spin of the reflected hole is opposite of the spin of the incoming electron.

Another important mechanism is NR. Here, the particle is reflected from the barrier with the same angle it had when it approached the barrier. Looking at Figure 4.2 eRup is the incoming electron, while eLup is the reflected electron. In a spin flip normal reflection (SNR), the particle is reflected with the spin flipped. Two other phenomena are TE and TH. In Figure 4.2 TE can be described by looking at eRup in the ferromagnetic side tunneling through the barrier and becoming eRup on superconducting side. TH is eRup on the ferromagnetic side becoming hRup on the superconducting side. During TE a charge of $-e$ will be transferred through the barrier. For TH, a charge of e will be transmitted through the barrier. Also for these processes there are spin flip variants: spin flip tunneling as electron-like quasiparticles (STE) and spin flip tunneling as hole-like quasiparticles (STH). The spin flipping processes, SAR, SNR, STE, and STH often arise from spin-orbit coupling effects at an interface.

4.3 Tight Binding Model

The derivation of the total Hamiltonian for the system starts by looking at the tight binding Hamiltonian for the ferromagnet,

$$\mathcal{H}_{FS} = \mathcal{H}_K + \mathcal{H}_{FM}\Theta(z) + \mathcal{H}_{SC}\Theta(-z) + \mathcal{H}_{int}\delta(z). \tag{4.1}$$

Here [42],

$$\mathcal{H}_{FM} = \mathcal{H}_{xc} + \mathcal{H}_{\mu}, \quad \mathcal{H}_K = -t_h \sum_{<i,j>,\delta,\sigma} c^{\dagger}_{i,\sigma} c_{j,\sigma}, \, , \qquad \Theta(z) = \begin{cases} 1 & \text{if } z > 0 \\ 0 & \text{otherwise} \end{cases},$$

$$\mathcal{H}_{SC} = \mathcal{H}_{\Delta} + \mathcal{H}_{\mu_{sc}}, \quad \mathcal{H}_{xc} = -\frac{\Delta_{xc}}{2} \sum_{i,\sigma} \boldsymbol{M} \cdot \boldsymbol{\sigma} c^{\dagger}_{i,\sigma} c_{i,\sigma}, \quad \mathcal{H}_{\Delta} = (\sigma \Delta c^{\dagger}_{i,\sigma} c^{\dagger}_{i,-\sigma} + \sigma \Delta^{\dagger} c_{i,\sigma} c_{i,-\sigma})$$

$$\mathcal{H}_{\mu} = \mu \sum_{i,\sigma} c^{\dagger}_{i,\sigma} c_{i,\sigma}, \quad \mathcal{H}_{\mu_{sc}} = \mu_{sc} \sum_{i,\sigma} c^{\dagger}_{i,\sigma} c_{i,\sigma}, \text{ and} \qquad \mathcal{H}_{int} = \sum_{i,\sigma} \boldsymbol{\omega} \cdot \boldsymbol{\sigma} c^{\dagger}_{i,\sigma} c_{i,\sigma} + Vd \sum_{i,\sigma} c^{\dagger}_{i,\sigma} c_{i,\sigma}.$$

Further, the connection between the exchange term and the Stoner parameter is $\Delta_{xc} = 2I \frac{N_{\uparrow} - N_{\downarrow}}{N}$, σ means spin up and $-\sigma$ means spin down, t_h is the hopping energy, μ is the chemical potential of the ferromagnet, μ_{sc} is the chemical potential of the superconductor, Δ is the superconducting gap, V is the potential at the interface, d is the width of the barrier, $c^{\dagger}$ is the creation operator, and c is the annihilation operator. Using $\boldsymbol{M} = \big[\sin\theta\cos\phi, \sin\theta\sin\phi, \cos\theta\big]$ and $\boldsymbol{\omega} = \big[\lambda_R k_y + \lambda_D k_x, -\lambda_R k_x - \lambda_D k_y, 0\big]$, the Hamiltonian is written utilizing creation and annihilation operators,

$$\begin{aligned}
\mathcal{H}_{FS} = & - t_h \sum_{<i,j>,\delta,\sigma} c^{\dagger}_{i,\sigma} c_{j,\sigma} + c^{\dagger}_{i,-\sigma} c_{j,-\sigma} - \mu \sum_{i,\sigma} (c^{\dagger}_{i,\sigma} c_{i,\sigma} + c^{\dagger}_{i,-\sigma} c_{i,-\sigma}) \Theta(z) \\
& - \mu_{sc} \sum_{i,\sigma} (c^{\dagger}_{i,\sigma} c_{i,\sigma} + c^{\dagger}_{i,-\sigma} c_{i,-\sigma}) \Theta(-z) - \frac{\Delta_{xc}}{2} \sum_{i,\sigma} (\cos\theta c^{\dagger}_{i,\sigma} c_{i,\sigma} + \sin\theta e^{-i\phi} c^{\dagger}_{i,-\sigma} c_{i,\sigma} \\
& + \sin\theta e^{i\phi} c^{\dagger}_{i,\sigma} c_{i,-\sigma} - \cos\theta c^{\dagger}_{i,-\sigma} c_{i,-\sigma}) \Theta(z) + \sum_{i,\sigma} (\sigma \Delta c^{\dagger}_{i,\sigma} c^{\dagger}_{i,-\sigma} + \sigma \Delta^{\dagger} c_{i,\sigma} c_{i,-\sigma}) \Theta(-z) \\
& + k_{\parallel} \sum_{i,\sigma} [(i\lambda_R e^{-i\phi} + \lambda_D e^{i\phi}) c^{\dagger}_{i,-\sigma} c_{i,\sigma} + (-i\lambda_R e^{i\phi} + \lambda_D e^{-i\phi}) c^{\dagger}_{i,\sigma} c_{i,-\sigma}] \delta(z) \\
& + Vd \sum_{i,\sigma} (c^{\dagger}_{i,\sigma} c_{i,\sigma} + c^{\dagger}_{i,-\sigma} c_{i,-\sigma}) \delta(z),
\end{aligned} \tag{4.2}$$

where $k_x = k_{\parallel} \cos\phi$ and $k_y = k_{\parallel} \sin\phi$. Next the Fourier transform is given by,

$$c_{i,\sigma} = \sum_{\boldsymbol{k}} c_{\boldsymbol{k}\sigma} e^{i\boldsymbol{k}\cdot\boldsymbol{r}_i}, \text{ and} \tag{4.3}$$

Now, insert equation 4.3 into the Hamiltonian setting $\Delta^{\dagger} = \Delta$,

$$
\begin{aligned}
\mathcal{H}_{FS} = & - t_h \sum_{\boldsymbol{k},\delta,\sigma} (c^{\dagger}_{\boldsymbol{k},\sigma} c_{\boldsymbol{k}',\sigma} e^{-i\boldsymbol{k}\cdot\boldsymbol{r}_i} e^{i\boldsymbol{k}'\cdot(\boldsymbol{r}_i+\boldsymbol{\delta})} + c^{\dagger}_{\boldsymbol{k},-\sigma} c_{\boldsymbol{k}',-\sigma} e^{-i\boldsymbol{k}\cdot\boldsymbol{r}_i} e^{i\boldsymbol{k}'\cdot(\boldsymbol{r}_i+\boldsymbol{\delta})}) \\
& - \mu \sum_{\boldsymbol{k},\sigma} (c^{\dagger}_{\boldsymbol{k},\sigma} c_{\boldsymbol{k}',\sigma} e^{-i\boldsymbol{k}\cdot\boldsymbol{r}_i} e^{i\boldsymbol{k}'\cdot\boldsymbol{r}_i} + c^{\dagger}_{\boldsymbol{k},-\sigma} c_{\boldsymbol{k}',-\sigma} e^{-i\boldsymbol{k}\cdot\boldsymbol{r}_i} e^{i\boldsymbol{k}'\cdot\boldsymbol{r}_i}) \Theta(z) \\
& - \mu_{sc} \sum_{\boldsymbol{k},\sigma} (c^{\dagger}_{\boldsymbol{k},\sigma} c_{\boldsymbol{k}',\sigma} e^{-i\boldsymbol{k}\cdot\boldsymbol{r}_i} e^{i\boldsymbol{k}'\cdot\boldsymbol{r}_i} + c^{\dagger}_{\boldsymbol{k},-\sigma} c_{\boldsymbol{k}',-\sigma} e^{-i\boldsymbol{k}\cdot\boldsymbol{r}} e^{i\boldsymbol{k}'\cdot\boldsymbol{r}_i}) \Theta(-z) \\
& - \frac{\Delta_{xc}}{2} \sum_{\boldsymbol{k},\sigma} (\cos\theta c^{\dagger}_{\boldsymbol{k},\sigma} c_{\boldsymbol{k}',\sigma} e^{-i\boldsymbol{k}\cdot\boldsymbol{r}_i} e^{i\boldsymbol{k}'\cdot\boldsymbol{r}_i} + \sin\theta e^{-i\phi} c^{\dagger}_{\boldsymbol{k},-\sigma} c_{\boldsymbol{k}',\sigma} e^{-i\boldsymbol{k}\cdot\boldsymbol{r}_i} e^{i\boldsymbol{k}'\cdot\boldsymbol{r}_i} \\
& + \sin\theta e^{i\phi} c^{\dagger}_{\boldsymbol{k},\sigma} c_{\boldsymbol{k}',-\sigma} e^{-i\boldsymbol{k}\cdot\boldsymbol{r}_i} e^{i\boldsymbol{k}'\cdot\boldsymbol{r}_i} - \cos\theta c^{\dagger}_{\boldsymbol{k},-\sigma} c_{\boldsymbol{k}',-\sigma} e^{-i\boldsymbol{k}\cdot\boldsymbol{r}_i} e^{i\boldsymbol{k}'\cdot\boldsymbol{r}_i}) \Theta(z) \\
& + \Delta \sum_{\boldsymbol{k},\sigma} (\sigma c^{\dagger}_{\boldsymbol{k},\sigma} c^{\dagger}_{\boldsymbol{k}',-\sigma} e^{-i\boldsymbol{k}\cdot\boldsymbol{r}_i} e^{-i\boldsymbol{k}'\cdot\boldsymbol{r}_i} + \sigma c_{\boldsymbol{k},\sigma} c_{\boldsymbol{k}',-\sigma} e^{i\boldsymbol{k}\cdot\boldsymbol{r}_i} e^{i\boldsymbol{k}'\cdot\boldsymbol{r}_i}) \Theta(-z) \\
& + k_{\parallel} \sum_{i,\sigma} [(i\lambda_R e^{-i\phi} + \lambda_D e^{i\phi}) c^{\dagger}_{\boldsymbol{k},-\sigma} c_{\boldsymbol{k}',\sigma} e^{-i\boldsymbol{k}\cdot\boldsymbol{r}} e^{i\boldsymbol{k}'\cdot\boldsymbol{r}_i} \\
& + (-i\lambda_R e^{i\phi} + \lambda_D e^{-i\phi}) c^{\dagger}_{\boldsymbol{k},\sigma} c_{\boldsymbol{k}',-\sigma} e^{-i\boldsymbol{k}\cdot\boldsymbol{r}_i} e^{i\boldsymbol{k}'\cdot\boldsymbol{r}_i}] \delta(z) \\
& + Vd \sum_{\boldsymbol{k},\sigma} (c^{\dagger}_{\boldsymbol{k},\sigma} c_{\boldsymbol{k}',\sigma} e^{-i\boldsymbol{k}\cdot\boldsymbol{r}_i} e^{i\boldsymbol{k}'\cdot\boldsymbol{r}_i} + c^{\dagger}_{\boldsymbol{k},-\sigma} c_{\boldsymbol{k}',-\sigma} e^{-i\boldsymbol{k}\cdot\boldsymbol{r}_i} e^{i\boldsymbol{k}'\cdot\boldsymbol{r}_i}) \delta(z).
\end{aligned}
\tag{4.4}
$$

By doing algebra the Hamiltonian becomes,

$$
\begin{aligned}
\mathcal{H}_{FS} = & - t_h \sum_{\boldsymbol{k},\sigma} \sum_{\boldsymbol{\delta}} e^{i\boldsymbol{k}'\cdot\boldsymbol{\delta}} (c^{\dagger}_{\boldsymbol{k},\sigma} c_{\boldsymbol{k}',\sigma} e^{i\boldsymbol{r}_i\cdot(\boldsymbol{k}'-\boldsymbol{k})} + c^{\dagger}_{\boldsymbol{k},-\sigma} c_{\boldsymbol{k}',-\sigma} e^{i\boldsymbol{r}_i\cdot(\boldsymbol{k}'-\boldsymbol{k})}) \\
& - \mu \sum_{\boldsymbol{k},\sigma} (c^{\dagger}_{\boldsymbol{k},\sigma} c_{\boldsymbol{k}',\sigma} e^{i\boldsymbol{r}_i\cdot(\boldsymbol{k}'-\boldsymbol{k})} + c^{\dagger}_{\boldsymbol{k},-\sigma} c_{\boldsymbol{k}',-\sigma} e^{i\boldsymbol{r}_i\cdot(\boldsymbol{k}'-\boldsymbol{k})}) \Theta(z) \\
& - \mu_{sc} \sum_{\boldsymbol{k},\sigma} (c^{\dagger}_{\boldsymbol{k},\sigma} c_{\boldsymbol{k}',\sigma} e^{i\boldsymbol{r}_i\cdot(\boldsymbol{k}'-\boldsymbol{k})} + c^{\dagger}_{\boldsymbol{k},-\sigma} c_{\boldsymbol{k}',-\sigma} e^{i\boldsymbol{r}_i\cdot(\boldsymbol{k}'-\boldsymbol{k})}) \Theta(-z) \\
& - \frac{\Delta_{xc}}{2} \sum_{\boldsymbol{k},\sigma} (\cos\theta c^{\dagger}_{\boldsymbol{k},\sigma} c_{\boldsymbol{k}',\sigma} e^{i\boldsymbol{r}_i\cdot(\boldsymbol{k}'-\boldsymbol{k})} + \sin\theta e^{-i\phi} c^{\dagger}_{\boldsymbol{k},-\sigma} c_{\boldsymbol{k}',\sigma} e^{i\boldsymbol{r}_i\cdot(\boldsymbol{k}'-\boldsymbol{k})} \\
& + \sin\theta e^{i\phi} c^{\dagger}_{\boldsymbol{k},\sigma} c_{\boldsymbol{k}',-\sigma} e^{i\boldsymbol{r}_i\cdot(\boldsymbol{k}'-\boldsymbol{k})} - \cos\theta c^{\dagger}_{\boldsymbol{k},-\sigma} c_{\boldsymbol{k}',-\sigma} e^{i\boldsymbol{r}_i\cdot(\boldsymbol{k}'-\boldsymbol{k})}) \Theta(z) \\
& + \Delta \sum_{\boldsymbol{k},\sigma} (\sigma c^{\dagger}_{\boldsymbol{k},\sigma} c^{\dagger}_{\boldsymbol{k}',-\sigma} e^{i\boldsymbol{r}_i\cdot(-\boldsymbol{k}'-\boldsymbol{k})} + \sigma c_{\boldsymbol{k},\sigma} c_{\boldsymbol{k}',-\sigma} e^{i\boldsymbol{r}_i\cdot(\boldsymbol{k}'+\boldsymbol{k})}) \Theta(-z)
\end{aligned}
\tag{4.5}
$$

$$
\begin{aligned}
&+ k_{\parallel} \sum_{i,\sigma} [(i\lambda_R e^{-i\phi} + \lambda_D e^{i\phi}) c^{\dagger}_{\boldsymbol{k},-\sigma} c_{\boldsymbol{k'},\sigma} e^{i\boldsymbol{r}_i \cdot (\boldsymbol{k'}-\boldsymbol{k})} \\
&+ (-i\lambda_R e^{i\phi} + \lambda_D e^{-i\phi}) c^{\dagger}_{\boldsymbol{k},\sigma} A_{\boldsymbol{k'},-\sigma} e^{i\boldsymbol{r}_i \cdot (\boldsymbol{k'}-\boldsymbol{k})}] \delta(z) \\
&+ Vd \sum_{\boldsymbol{k},\sigma} (c^{\dagger}_{\boldsymbol{k},\sigma} c_{\boldsymbol{k'},\sigma} e^{i\boldsymbol{r}_i \cdot (\boldsymbol{k'}-\boldsymbol{k})} + c^{\dagger}_{\boldsymbol{k},-\sigma} c_{\boldsymbol{k'},-\sigma} e^{i\boldsymbol{r}_i \cdot (\boldsymbol{k'}-\boldsymbol{k})}) \delta(z).
\end{aligned}
$$

Now, utilize the mathematical equality,

$$
\sum_i e^{i\boldsymbol{r_i} \cdot (\boldsymbol{k'}-\boldsymbol{k})} = \delta(\boldsymbol{k'} - \boldsymbol{k}), \tag{4.6}
$$

to progress with the derivation of the total Hamiltonian for the FS hybrid junction. Using equation 4.6, the Hamiltonian is given by,

$$
\begin{aligned}
\mathcal{H}_{FS} = &- t_h \sum_{\boldsymbol{k},\sigma} \sum_{\boldsymbol{\delta}} e^{i\boldsymbol{k}\cdot\boldsymbol{\delta}} (c^{\dagger}_{\boldsymbol{k},\sigma} c_{\boldsymbol{k},\sigma} + c^{\dagger}_{\boldsymbol{k},-\sigma} c_{\boldsymbol{k},-\sigma}) - \mu \sum_{\boldsymbol{k},\sigma} (c^{\dagger}_{\boldsymbol{k},\sigma} c_{\boldsymbol{k},\sigma} \\
&+ c^{\dagger}_{\boldsymbol{k},-\sigma} c_{\boldsymbol{k},-\sigma}) \Theta(z) - \mu_{sc} \sum_{\boldsymbol{k},\sigma} (c^{\dagger}_{\boldsymbol{k},\sigma} c_{\boldsymbol{k},\sigma} + c^{\dagger}_{\boldsymbol{k},-\sigma} c_{\boldsymbol{k},-\sigma}) \Theta(-z) \\
&- \frac{\Delta_{xc}}{2} \sum_{\boldsymbol{k},\sigma} (\cos\theta c^{\dagger}_{\boldsymbol{k},\sigma} c_{\boldsymbol{k},\sigma} + \sin\theta e^{-i\phi} c^{\dagger}_{\boldsymbol{k},-\sigma} c_{\boldsymbol{k},\sigma} + \sin\theta e^{i\phi} c^{\dagger}_{\boldsymbol{k},\sigma} c_{\boldsymbol{k},-\sigma} \\
&- \cos\theta c^{\dagger}_{\boldsymbol{k},-\sigma} c_{\boldsymbol{k},-\sigma}) \Theta(z) + \Delta \sum_{\boldsymbol{k},\sigma} (\sigma c^{\dagger}_{\boldsymbol{k},\sigma} c^{\dagger}_{-\boldsymbol{k},-\sigma} + \sigma c_{\boldsymbol{k},\sigma} c_{-\boldsymbol{k},-\sigma}) \Theta(-z) \\
&+ k_{\parallel} \sum_{i,\sigma} [(i\lambda_R e^{-i\phi} + \lambda_D e^{i\phi}) c^{\dagger}_{\boldsymbol{k},-\sigma} c_{\boldsymbol{k},\sigma} + (-i\lambda_R e^{i\phi} + \lambda_D e^{-i\phi}) c^{\dagger}_{\boldsymbol{k},\sigma} c_{\boldsymbol{k},-\sigma}] \delta(z) \\
&+ Vd \sum_{\boldsymbol{k},\sigma} (c^{\dagger}_{\boldsymbol{k},\sigma} c_{\boldsymbol{k},\sigma} + c^{\dagger}_{\boldsymbol{k},-\sigma} c_{\boldsymbol{k},-\sigma}) \delta(z).
\end{aligned} \tag{4.7}
$$

The kinetic energy of the itinerant electrons is,

$$
\gamma_{\boldsymbol{k}} = -t_h \sum_{\boldsymbol{\delta}} e^{i\boldsymbol{k}\cdot\boldsymbol{\delta}}. \tag{4.8}
$$

Then the total Hamiltonian is given by,

$$
\begin{aligned}
\mathcal{H}_{FS} = & \sum_{\boldsymbol{k},\sigma} \gamma_{\boldsymbol{k}} (c^{\dagger}_{\boldsymbol{k},\sigma} c_{\boldsymbol{k},\sigma} + c^{\dagger}_{\boldsymbol{k},-\sigma} c_{\boldsymbol{k},-\sigma}) - \mu \sum_{\boldsymbol{k},\sigma} (c^{\dagger}_{\boldsymbol{k},\sigma} c_{\boldsymbol{k},\sigma} \\
& + c^{\dagger}_{\boldsymbol{k},-\sigma} c_{\boldsymbol{k},-\sigma}) \Theta(z) - \mu_{sc} \sum_{\boldsymbol{k},\sigma} (c^{\dagger}_{\boldsymbol{k},\sigma} c_{\boldsymbol{k},\sigma} + c^{\dagger}_{\boldsymbol{k},-\sigma} c_{\boldsymbol{k},-\sigma}) \Theta(-z) \\
& - \frac{\Delta_{xc}}{2} \sum_{\boldsymbol{k},\sigma} (\cos\theta c^{\dagger}_{\boldsymbol{k},\sigma} c_{\boldsymbol{k},\sigma} + \sin\theta e^{-i\phi} c^{\dagger}_{\boldsymbol{k},-\sigma} c_{\boldsymbol{k},\sigma} + \sin\theta e^{i\phi} c^{\dagger}_{\boldsymbol{k},\sigma} c_{\boldsymbol{k},-\sigma} \\
& - \cos\theta c^{\dagger}_{\boldsymbol{k},-\sigma} c_{\boldsymbol{k},-\sigma}) \Theta(z) + \Delta \sum_{\boldsymbol{k},\sigma} (\sigma c^{\dagger}_{\boldsymbol{k},\sigma} c^{\dagger}_{-\boldsymbol{k},-\sigma} + \sigma c_{\boldsymbol{k},\sigma} c_{-\boldsymbol{k},-\sigma}) \Theta(-z) \\
& + k_{\parallel} \sum_{i,\sigma} [(i\lambda_R e^{-i\phi} + \lambda_D e^{i\phi}) c^{\dagger}_{\boldsymbol{k},-\sigma} c_{\boldsymbol{k},\sigma} + (-i\lambda_R e^{i\phi} + \lambda_D e^{-i\phi}) c^{\dagger}_{\boldsymbol{k},\sigma} c_{\boldsymbol{k},-\sigma}] \delta(z) \\
& + Vd \sum_{\boldsymbol{k},\sigma} (c^{\dagger}_{\boldsymbol{k},\sigma} c_{\boldsymbol{k},\sigma} + c^{\dagger}_{\boldsymbol{k},-\sigma} c_{\boldsymbol{k},-\sigma}) \delta(z).
\end{aligned} \tag{4.9}
$$

The basis used in the calculations is,

$$
\boldsymbol{\chi}_{FS} = \begin{bmatrix} c^{\dagger}_{e,\sigma} \\ c^{\dagger}_{e,-\sigma} \\ c_{h,-\sigma} \\ c_{h,\sigma} \end{bmatrix}, \tag{4.10}
$$

where σ is the spin. To proceed, rewrite the Hamiltonian with only the terms that are in the basis and their Hermitian conjugates. This is done by looking up the fermionic anticommutator relations given by equation 3.9 and 3.10. Summing over $\boldsymbol{k}$ and σ and utilizing the commutator and anticommutator relations, the Hamiltonian is given by,

$$
\begin{aligned}
\mathcal{H}_{FS} = & \gamma_{\boldsymbol{k}} (c^{\dagger}_{e,\sigma} c_{e,\sigma} + c^{\dagger}_{e,-\sigma} c_{e,-\sigma}) - \gamma_{-\boldsymbol{k}} (c_{h,\sigma} c^{\dagger}_{h,\sigma} + c_{h,-\sigma} c^{\dagger}_{h,-\sigma}) \\
& - \mu (c^{\dagger}_{e,\sigma} c_{e,\sigma} + c^{\dagger}_{e,-\sigma} c_{e,-\sigma} - c_{h,\sigma} c^{\dagger}_{h,\sigma} - c_{h,-\sigma} c^{\dagger}_{h,-\sigma}) \Theta(z) \\
& - \mu_{sc} (c^{\dagger}_{e,\sigma} c_{e,\sigma} + c^{\dagger}_{e,-\sigma} c_{e,-\sigma} - c_{h,\sigma} c^{\dagger}_{h,\sigma} - c_{h,-\sigma} c^{\dagger}_{h,-\sigma}) \Theta(-z)
\end{aligned}
$$

$$
\begin{aligned}
&- \frac{\Delta_{xc}}{2}(\cos\theta c^{\dagger}_{e,\sigma}c_{e,\sigma} + \sin\theta e^{-i\phi}c^{\dagger}_{e,-\sigma}c_{e,\sigma} + \sin\theta e^{i\phi}c^{\dagger}_{e,\sigma}c_{e,-\sigma} \\
&- \cos\theta c^{\dagger}_{e,-\sigma}c_{e,-\sigma} - \cos\theta c_{h,\sigma}c^{\dagger}_{h,\sigma} - \sin\theta e^{-i\phi}c_{h,\sigma}c^{\dagger}_{h,-\sigma} \\
&- \sin\theta e^{i\phi}c_{h,-\sigma}c^{\dagger}_{h,\sigma} + \cos\theta c_{h,-\sigma}c^{\dagger}_{h,-\sigma})\Theta(z) + \Delta(c^{\dagger}_{e,\sigma}c^{\dagger}_{h,-\sigma} \\
&+ c_{h,-\sigma}c_{e,\sigma} + c^{\dagger}_{e,-\sigma}c^{\dagger}_{h,\sigma} + c_{h,\sigma}c_{e,-\sigma})\Theta(-z) \\
&+ k_{\parallel}[(i\lambda_R e^{-i\phi} + \lambda_D e^{i\phi})c^{\dagger}_{e,-\sigma}c_{e,\sigma} + (-i\lambda_R e^{i\phi} + \lambda_D e^{-i\phi})c^{\dagger}_{e,\sigma}c_{e,-\sigma} \\
&- (i\lambda_R e^{-i\phi} + \lambda_D e^{i\phi})c_{h,\sigma}c^{\dagger}_{h,-\sigma} - (-i\lambda_R e^{i\phi} + \lambda_D e^{-i\phi})c_{h,-\sigma}c^{\dagger}_{h,\sigma}]\delta(z) \\
&+ Vd(c^{\dagger}_{e,\sigma}c_{e,\sigma} + c^{\dagger}_{e,-\sigma}c_{e,-\sigma} - c_{h,\sigma}c^{\dagger}_{h,\sigma} - c_{h,-\sigma}c^{\dagger}_{h,-\sigma})\delta(z).
\end{aligned}
\tag{4.11}
$$

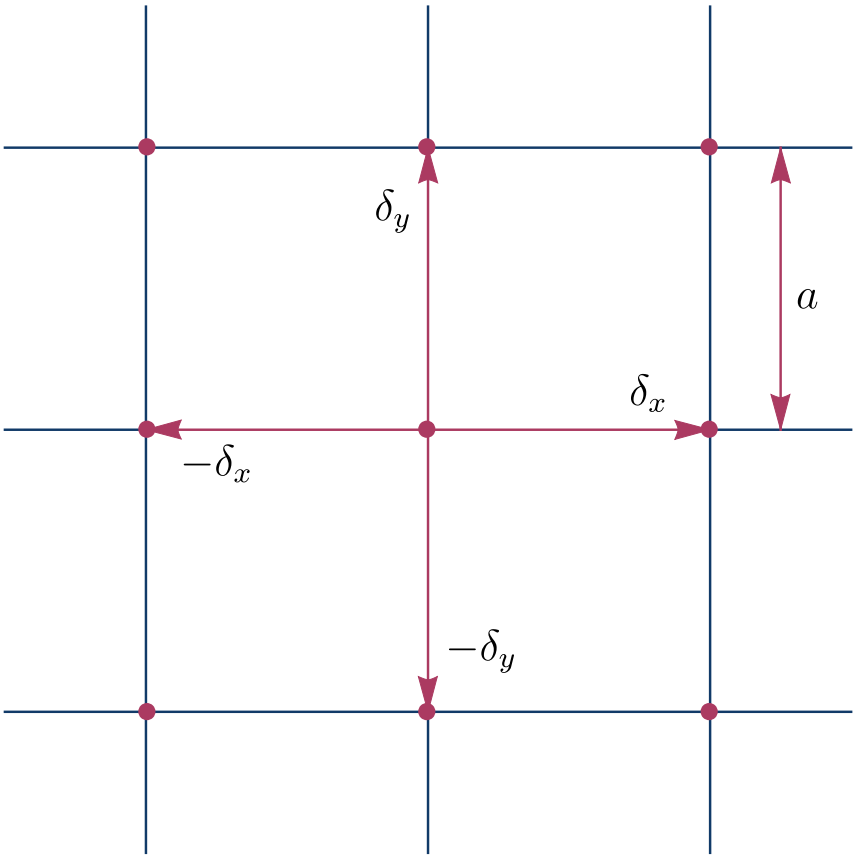

Figure 4.3: A 2D schematic of a square lattice. Here $\delta_x = a(1,0,0)$, $\delta_y = a(0,1,0)$ and $\delta_z = a(0,0,1)$. Further, a is the lattice spacing, and the lattice follow the same pattern in the $\hat{z}$-direction.

Equation 4.11 contains both kinetic energy $\gamma_{\boldsymbol{k}}$ and $\gamma_{-\boldsymbol{k}}$. In order to analyze the kinetic energy term in more detail, a square lattice will be assumed for the remainder of the calculations. In Figure 4.3, such a lattice is displayed. Lets proce that $\gamma_{\boldsymbol{k}} = \gamma_{-\boldsymbol{k}} = \gamma_{\boldsymbol{k}}^\dagger = \gamma_{-\boldsymbol{k}}^\dagger$ is valid,

$$\begin{aligned}
\gamma_{\boldsymbol{k}} &= -t_h \sum_{\boldsymbol{\delta}} e^{i\boldsymbol{k}\cdot\boldsymbol{\delta}} \\
&= -t_h[(e^{-ik_x a} + e^{ik_x a}) + (e^{-ik_y a} + e^{ik_y a}) + (e^{-ik_z a} + e^{ik_z a})] \\
&= -t_h[(e^{ik_x a} + e^{-ik_x a}) + (e^{ik_y a} + e^{-ik_y a}) + (e^{ik_z a} + e^{-ik_z a})] = \gamma_{-\boldsymbol{k}} \\
&= -2t_h(\cos k_x a + \cos k_y a + \cos k_z a) \\
&= -2t_h(1 - \frac{k_x^2 a^2}{2} + 1 - \frac{k_y^2 a^2}{2} + 1 - \frac{k_z^2 a^2}{2}) \\
&= t_h(k^2 a^2 - 6) = a^2 t_h(k^2 - \frac{6}{a^2}) = a^2 t_h(k^2 - k_0^2) = \gamma_{\boldsymbol{k}}^\dagger,
\end{aligned} \tag{4.12}$$

where $k_0 = \frac{\sqrt{6}}{a}$. Next, set $Vd\gamma\mu_{sc-}^- = \gamma_{\boldsymbol{k}} - \mu\Theta(z) - \mu_{sc}\Theta(-z) + Vd\delta(z)$, $P_s^- = -\frac{\Delta_{xc}}{2}\sin\theta e^{-i\phi}\Theta(z)$, $P_s^+ = -\frac{\Delta_s}{2}\sin\theta e^{i\phi}\Theta(z)$, $P_c = -\frac{\Delta_{xc}}{2}\cos\theta\Theta(z)$, $R_-^+ L_+^- = k_\parallel(-i\lambda_R e^{i\phi} + \lambda_D e^{-i\phi})\delta(z)$, and $R_+^- L_+^+ = k_\parallel(i\lambda_R e^{-i\phi} + \lambda_D e^{i\phi})\delta(z)$ and write the Hamiltonian in matrix form,

$$\mathcal{H}_m = \begin{bmatrix} Vd\gamma\mu_-^- + P_c & P_s^- + R_+^- L_+^+ & \Delta\Theta(-z) & 0 \\ P_s^+ + R_-^+ L_+^- & Vd\gamma\mu_-^- - P_c & 0 & \Delta\Theta(-z) \\ \Delta\Theta(-z) & 0 & -Vd\gamma\mu_-^- - P_c & -P_s^- - R_+^- L_+^+ \\ 0 & \Delta\Theta(-z) & -P_s^+ - R_-^+ L_+^- & -Vd\gamma\mu_-^- + P_c \end{bmatrix}, \tag{4.13}$$

such that $\mathcal{H}_{FS} = \boldsymbol{\chi}_{FS}\mathcal{H}_m\boldsymbol{\chi}_{FS}^\dagger$. Here k_0 has been omitted from the equation because it only represent a shift in energy in correspondence with $\mathcal{H}_{k_0} = -\frac{\hbar^2 k_0^2}{2m}$.

4.4 Blonder-Tinkham-Klapwijk Formalism

Two types of particle transport in systems are ballistic and diffusive. Usually ballistic transport is considered in the case of a clean system, while diffusive transport is the case for dirty systems. A system is considered clean if the electron mean free path is greater than the coherence length, and

dirty if the coherence length is greater than the electron mean free path [17]. In 1982, Blonder, Tinkham and Klapwijk formulated their famous BTK formalism [10], which is widely used for clean superconductors. In the dirty limit, theory developed by Klaus D. Usadel is used. Utilizing his Usadel equation, which is a diffusionlike equation, it is possible to obtain all information about a dirty superconductor [64]. In the following calculations, a high purity superconductor is assumed, therefore a closer look at the BTK approach is presented here. An example of such a superconductor is the s-wave superconductor Nb, in which high purity films are considered clean [17]. It should be noted that the following method will work for all clean s-wave superconductors, and that the reader is free to choose a superconductor of his or her choice.

BTK theory utilizes the BdG equation, model the interface between a normal metal and a superconductor as a delta function of arbitrary strength and investigate the scattering mechanisms at the interface, as described in Subchapter 4.2. The formalism predicts the reflection and transmission coefficients which are used in the final expressions for TC, SkC and FOM, see Chapter 6. BTK is a mean-field theory, and does not take residual interactions, such as quasiparticle scattering and coupling with the bosonic modes in the system, into account.

In this thesis, a modified BTK approach will be used. A FS junction will be examined instead of a normal metal-superconductor junction, which the BTK formalism was originally designed for. Theory developed by Nikolay Bogoliubov and Pierre-Gilles deGennes [26] is utilized as the starting point of the analysis. To arrive at the BdG equation, start by looking at BCS theory. As mentioned in Subsection 3.3.1, there are many similarities between BCS and Hartree-Fock theory. Modifying the BCS Hamiltonian in equation 3.4 it can be shown that [1],

$$\mathcal{H}_0 = \int d\boldsymbol{r} \left\{ \sum_{\delta} \psi_{\delta}^{\dagger} \mathcal{H}_K \psi_{\delta} + \frac{1}{2} \sum_{\delta,\gamma} \left(\Delta \psi_{\delta}^{\dagger} \psi_{\gamma}^{\dagger} + \Delta^* \psi_{\delta} \psi_{\gamma} + \psi_{\delta}^{\dagger} \boldsymbol{h} \cdot \boldsymbol{\tau} \psi_{\gamma} \right) \right\}. \tag{4.14}$$

Here, the ψ's are wave functions, Δ describes the superconducting gap, $\boldsymbol{h}$ is describing the magnetic exchange field, and $\boldsymbol{\tau}$ is the 4×4 Pauli matrices. Now, introduce the Bogoliubov-deGennes transformations given by,

$$\psi_{\uparrow}(\boldsymbol{r}) = \sum_n (c_{n,\uparrow} u_n(\boldsymbol{r}) - c_{n,\downarrow}^{\dagger} v_n^*(\boldsymbol{r})) \tag{4.15}$$

and

$$\psi_{\downarrow}(\boldsymbol{r}) = \sum_n (c_{n,\downarrow} u_n(\boldsymbol{r}) + c_{n,\uparrow}^{\dagger} v_n^*(\boldsymbol{r})), \tag{4.16}$$

where $c^{\dagger}_{n,\uparrow/\downarrow}$ is the creation operator, $c_{n,\uparrow/\downarrow}$ is the annihilation operator, $u_n(\boldsymbol{r})$ is a position dependent complex coefficient, and $v_n(\boldsymbol{r})$ is a position dependent complex coefficient. Calculating the commutation relations $[\psi_{\uparrow}(\boldsymbol{r}), \mathcal{H}]$ and $[\psi_{\downarrow}(\boldsymbol{r}), \mathcal{H}]$ and presenting them in matrix form, the well-known BdG equation is obtained,

$$\begin{bmatrix} \mathcal{H}_e & \Delta_s \\ \Delta_s^{\dagger} & \mathcal{H}_h \end{bmatrix} \Psi(\boldsymbol{r}) = E\Psi(\boldsymbol{r}), \tag{4.17}$$

where $\Delta_s = \Delta\sigma_0\Theta(-z)$. The single-particle Hamiltonian for the electrons in equation 4.17, including interface effects, is given by,

$$\mathcal{H}_e = -\frac{\hbar^2}{2m}\sigma_0\nabla^2 - \mu\sigma_0 - \frac{\Delta_{xc}}{2}\Theta(z)\boldsymbol{M}\cdot\boldsymbol{\sigma} + \mathcal{H}_{int}, \tag{4.18}$$

where m is particle mass, μ is the chemical potential and $\boldsymbol{M} = [\sin\theta\cos\phi, \sin\theta\sin\phi, \cos\theta]$ is the uniform magnetization. Here, θ is the polar angle and ϕ is the azimuthal angle seen in Figure 4.1. The interfacial barrier is $\mathcal{H}_{int} = (Vd\sigma_0 + \boldsymbol{\omega}\cdot\boldsymbol{\sigma})\delta(z)$, where V is describing the potential at the barrier and d is the width of the barrier. The spin-orbit coupling field is $\boldsymbol{\omega} = \big[\lambda_R k_y + \lambda_D k_x, -\lambda_R k_x - \lambda_D k_y, 0\big]$, in which λ_R is the effective strength of the Rashba field and λ_D is the effective strength of the Dresselhaus field. Δ_{xc} is the exchange spin splitting, $\boldsymbol{\sigma}$ is the Pauli spin matrix vector, and σ_0 is the 2×2 identity matrix.

The single-particle Hamiltonian for the holes is given by,

$$\mathcal{H}_h = -\sigma_y\mathcal{H}_e^*\sigma_y. \tag{4.19}$$

By writing out the BdG expression utilizing equation 4.18 and 4.19 the same expression that was derived from the tight binding model in equation 4.13 will be obtained. The step-wise calculation can be found in Appendix B.

4.4.1 Ferromagnet

Now, take a look at the ferromagnetic region ($z > 0$) in order to find the particle wave function in that part of the material composition. The hopping energy is given by $t_h = \frac{\hbar^2}{2m}$ for a square

lattice, making $\gamma_k = \frac{\hbar^2 k^2}{2m}$. Insert this into equation 4.13, set $k\mu = \frac{\hbar^2 k^2}{2m} - \mu$, $z > 0$, and rewrite as a wave equation,

$$\begin{bmatrix} k\mu - \frac{\Delta_{xc}\cos\theta}{2} & -\frac{\Delta_{xc}\sin\theta e^{-i\phi}}{2} & 0 & 0 \\ -\frac{\Delta_{xc}\sin\theta e^{i\phi}}{2} & k\mu + \frac{\Delta_{xc}\cos\theta}{2} & 0 & 0 \\ 0 & 0 & -k\mu + \frac{\Delta_{xc}\cos\theta}{2} & \frac{\Delta_{xc}\sin\theta e^{-i\phi}}{2} \\ 0 & 0 & \frac{\Delta_{xc}\sin\theta e^{i\phi}}{2} & -k\mu - \frac{\Delta_{xc}\cos\theta}{2} \end{bmatrix} \Psi^{\sigma}_{FM}(\boldsymbol{r}) = E\Psi^{\sigma}_{FM}(\boldsymbol{r}), \quad (4.20)$$

where $\Psi^{\sigma}_{FM}(\boldsymbol{r})$ is an linear combination of probability amplitudes, plane waves and eigenvectors of the Hamiltonian. Using Mathematica, the eigenvalues of the matrix is found,

$$E_k^{\eta,\nu} = \eta\frac{\hbar^2 k^2}{2m} - \eta\mu + \nu\frac{\Delta_{xc}}{2}, \quad (4.21)$$

where $\eta = 1$ for electrons, $\eta = -1$ for holes and $\nu = \pm 1$. The eigenvalues are displayed in Figure 4.4 for $\eta = 1$, $\nu = 1$ and $\mu = E_F$.

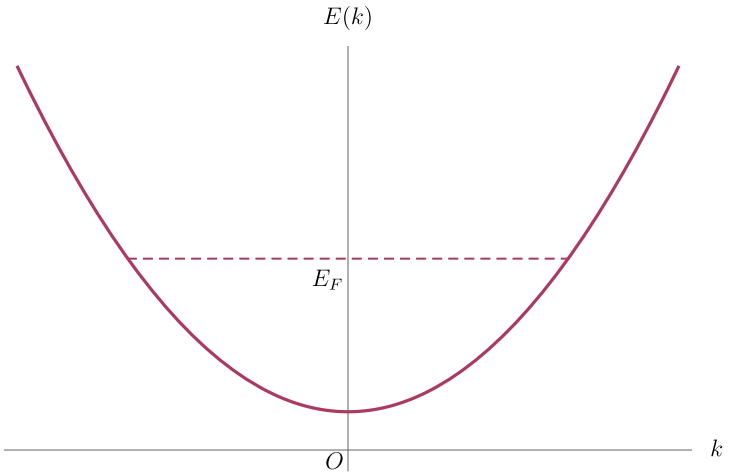

Figure 4.4: The eigenvalues for the ferromagnetic region with $\eta = 1$ and $\nu = 1$. Here, E_F denotes the Fermi energy and O is the origin.

From the eigenvalues, an expression for the wave vector in the z direction can be obtained. Here, set $k^2 = k_x^2 + k_y^2 + k_z^2$ and define $k_p^2 = k_x^2 + k_y^2$, giving $k^2 = k_p^2 + k_z^2$. The wave vector is then given by,

$$k_z^{\eta,\sigma} = \sqrt{-k_\parallel^2 + 2m\left(\frac{\frac{\sigma\Delta_{xc}}{2} + \eta E + \mu}{\hbar^2}\right)}, \tag{4.22}$$

where $\sigma = -\eta\nu = \pm 1$ is the spin of the particles. Next, use Mathematica to get the eigenvectors of the matrix,

$$\chi_{FM}^{e,\sigma} = \begin{bmatrix} \chi_{FM}^{\sigma} \\ \\ 0 \end{bmatrix}, \tag{4.23}$$

$$\chi_{FM}^{h,\sigma} = \begin{bmatrix} 0 \\ \\ \chi_{FM}^{-\sigma} \end{bmatrix} \tag{4.24}$$

and

$$\chi_{FM}^{\sigma} = \begin{bmatrix} \frac{\sigma\sqrt{1+\sigma\cos\theta}e^{-i\theta}}{\sqrt{2}} \\ \\ \frac{\sqrt{1-\sigma\cos\theta}}{\sqrt{2}} \end{bmatrix}. \tag{4.25}$$

With the eigenfunctions of the matrix, the solutions for the BdG equation in the ferromagnet can be found. The solutions will have to be built up of plane waves, and Figure 4.2 can therefore be used to find the solution. In the figure there are five possibilities for the electron in the ferromagnet. According to Section 4.2, there will be AR, SAR, NR, and SNR in addition to the incoming electron. $r^{\sigma,e(h)}$ gives the reflection amplitude for an electron (hole) being reflected with the same spin as it struck the interface with, while $r^{-\sigma,e(h)}$ gives the reflection amplitude for an electron (hole) having its spin flipped during the reflection. The wave function in the ferromagnet is given by,

$$\begin{aligned}\Psi^{\sigma}_{z,FM}(z) = \frac{1}{\sqrt{k_z^{e,\sigma}}} e^{ik_z^{e,\sigma}z}\chi^{e,\sigma}_{FM} + r^{e,\sigma}e^{-ik_z^{e,\sigma}z}\chi^{e,\sigma}_{FM} + r^{e,-\sigma}e^{-ik_z^{e,-\sigma}z}\chi^{e,-\sigma}_{FM} \\ + r^{h,-\sigma}e^{ik_z^{h,-\sigma}z}\chi^{h,-\sigma}_{FM} + r^{h,\sigma}e^{ik_z^{h,\sigma}z}\chi^{h,\sigma}_{FM}.\end{aligned} \tag{4.26}$$

In the xy plane, the wave vector is conserved. This is because incoming electrons has velocity only in the $-\hat{z}$ direction. Taking this into account the total position dependent wave function in the ferromagnet is given by,

$$\Psi^{\sigma}_{FM}(\boldsymbol{r}) = \Psi^{\sigma}_{z,FM}(z)e^{i(k_x x + k_y y)}. \tag{4.27}$$

4.4.2 Superconductor

Now, move back to the total Hamiltonian and solve it for the superconducting region where $z < 0$. From now on $k \to q$, where $q = |\boldsymbol{q}|$, will be used to signify the difference between the wave vectors in the superconductor and the ferromagnet. The hopping energy is here given by $t_h = \frac{\hbar^2}{2m}$ for a square lattice, making $\gamma_q = \frac{\hbar^2 q^2}{2m}$. Inserting this into equation 4.13 the wave equation is given as,

$$\begin{bmatrix} \frac{\hbar^2q^2}{2m} - \mu_{sc} & 0 & \Delta & 0 \\ 0 & \frac{\hbar^2q^2}{2m} - \mu_{sc} & 0 & \Delta \\ \Delta^\dagger & 0 & \mu_{sc} - \frac{\hbar^2q^2}{2m} & 0 \\ 0 & \Delta^\dagger & 0 & \mu_{sc} - \frac{\hbar^2q^2}{2m} \end{bmatrix} \Psi^{\sigma}_S(\boldsymbol{r}) = E\Psi^{\sigma}_S(\boldsymbol{r}), \tag{4.28}$$

where $\Psi^{\sigma}_S(\boldsymbol{r})$ is a linear combination of probability amplitudes, plane waves and eigenvectors of the Hamiltonian. Again, it is desirable to find the eigenvalues and eigenvectors for the matrix. These will be used to find the fermionic wavefunction of a particle in the superconducting side of the junction. Looking back at Subsection 3.3.1, the eigenvalues for the superconducting Hamiltonian were given by equation 3.25, and displayed below in Figure 4.5. Inserting $\xi_q = \frac{\hbar^2q^2}{2m} - \mu_{sc}$, the eigenvalues are given as,

$$E_q^{\upsilon} = \upsilon\sqrt{\left(\frac{\hbar^2 q^2}{2m} - \mu_{sc}\right)^2 + |\Delta|^2}. \tag{4.29}$$

The upper band with $\upsilon = 1$ is described by equation 4.29 and displayed with $\mu_{sc} = E_F$ in Figure 4.5.

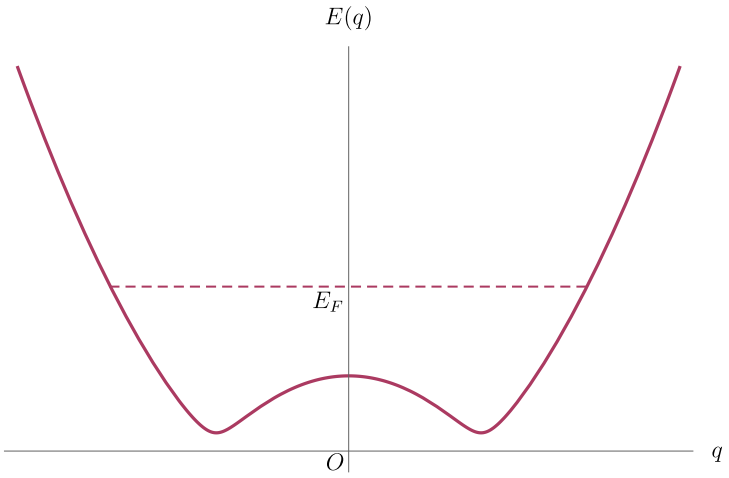

Figure 4.5: The eigenvalues for the superconducting region in the FS junction with $\upsilon = 1$. Here, E_F denotes the Fermi energy and O is the origin.

The eigenvalues can be rewritten as,

$$q_z^{\eta} = \sqrt{-q_p^2 + \eta\frac{2m\sqrt{E^2 - \Delta^2}}{\hbar^2} + \frac{2m\mu_{sc}}{\hbar^2}}, \tag{4.30}$$

where $\eta = 1$ for electrons, $\eta = -1$ for holes and $q^2 = q_z^2 + q_p^2$. Next, the eigenvectors are needed to build up the wave function inside the superconductor. In the normal metal-superconductor case, the eigenvectors in the superconductor will be,

$$\chi_S^e = \begin{bmatrix} u_q \\ \\ v_q \end{bmatrix}, \text{ and } \chi_S^h = \begin{bmatrix} v_q \\ \\ u_q \end{bmatrix}, \tag{4.31}$$

where u_q is given by equation 3.22 and v_q is given by equation 3.23, see Subsection 3.3.1. In the AS junction, there is spin degree of freedom too, making the total eigenvectors $\chi_S^{\eta,\sigma}$,

$$\begin{aligned}
\chi_S^{e,\sigma} &= \begin{bmatrix} u_q & v_q \end{bmatrix} \otimes \begin{bmatrix} 1 \\ 0 \end{bmatrix} = \begin{bmatrix} u_q \\ 0 \\ v_q \\ 0 \end{bmatrix}, \qquad \chi_S^{e,-\sigma} = \begin{bmatrix} u_q & v_q \end{bmatrix} \otimes \begin{bmatrix} 0 \\ 1 \end{bmatrix} = \begin{bmatrix} 0 \\ u_q \\ 0 \\ v_q \end{bmatrix}, \\
\chi_S^{h,\sigma} &= \begin{bmatrix} v_q & u_q \end{bmatrix} \otimes \begin{bmatrix} 1 \\ 0 \end{bmatrix} = \begin{bmatrix} v_q \\ 0 \\ u_q \\ 0 \end{bmatrix}, \text{ and } \quad \chi_S^{h,-\sigma} = \begin{bmatrix} v_q & u_q \end{bmatrix} \otimes \begin{bmatrix} 0 \\ 1 \end{bmatrix} = \begin{bmatrix} 0 \\ v_q \\ 0 \\ u_q \end{bmatrix}.
\end{aligned} \tag{4.32}$$

Next, look at the superconducting region in Figure 4.2. It is known that the solutions to the BdG will have to be plane waves, but their amplitudes are needed as well. From Section 4.2, it can be seen that TE, STE, TH and STH will be present. $t_{e(h),\sigma}$ gives the transmission amplitude for an electron (hole) being transmitted with the same spin as it struck the interface with, while $t_{e(h),-\sigma}$ gives the transmission amplitude for an electron (hole) having its spin flipped during the transmission. Using this information, the superconductor wave function is obtained as,

$$\Psi_{z,S}^{\sigma}(z) = t_{e,\sigma} e^{iq_z^e z} \begin{bmatrix} u_q \\ 0 \\ v_q \\ 0 \end{bmatrix} + t_{e,-\sigma} e^{iq_z^e z} \begin{bmatrix} 0 \\ u_q \\ 0 \\ v_q \end{bmatrix} + t_{h,\sigma} e^{-iq_z^h z} \begin{bmatrix} v_q \\ 0 \\ u_q \\ 0 \end{bmatrix} + t_{h,-\sigma} e^{-iq_z^h z} \begin{bmatrix} 0 \\ v_q \\ 0 \\ u_q \end{bmatrix}. \tag{4.33}$$

In the xy plane, the wave vector is conserved. This is because incoming electrons is sent only in the $-\hat{z}$ direction. Utilizing this, the position dependent wave function becomes,

$$\Psi_S^\sigma(\boldsymbol{r}) = \Psi_{z,S}^\sigma(z) e^{i(k_x x + k_y y)}. \tag{4.34}$$

4.4.3 Boundary Conditions

To find the coefficients in equation 4.26 and 4.33, the boundary conditions for a delta function interface [27] is used,

$$\Psi_{z,F}^\sigma|_{z=0^+} = \Psi_{z,S}^\sigma|_{z=0^-}. \tag{4.35}$$

To find the boundary condition for the first order derivative, the Schrödinger equation is integrated from $-b$ to b,

$$\int_{-b}^{b} \mathcal{H}_m \Psi(z) = \int_{-b}^{b} E\Psi(z), \tag{4.36}$$

where $\mathcal{H}_m$ is given by equation 4.13. To proceed with the calculations, divide the Hamiltonian into its respective elements,

$$\mathcal{H}_m = \begin{bmatrix} Vd\gamma\mu_- + P_c & P_s^- + R_+^- L_+^+ & \Delta\Theta(-z) & 0 \\ P_s^+ + R_-^+ L_+^- & Vd\gamma\mu_- - P_c & 0 & \Delta\Theta(-z) \\ \Delta\Theta(-z) & 0 & -Vd\gamma\mu_- - P_c & -P_s^- - R_+^- L_+^+ \\ 0 & \Delta\Theta(-z) & -P_s^+ - R_-^+ L_+^- & -Vd\gamma\mu_- + P_c \end{bmatrix}$$

$$= \begin{bmatrix} 1 & 0 & 0 & 0 \\ 0 & 1 & 0 & 0 \\ 0 & 0 & -1 & 0 \\ 0 & 0 & 0 & -1 \end{bmatrix} \frac{\hbar^2 k^2}{2m} + \begin{bmatrix} -\frac{\Delta_{xc}}{2}\cos\theta & -\frac{\Delta_{xc}}{2}\sin\theta e^{-i\phi} & 0 & 0 \\ -\frac{\Delta_{xc}}{2}\sin\theta e^{i\phi} & \frac{\Delta_{xc}}{2}\cos\theta & 0 & 0 \\ 0 & 0 & \frac{\Delta_{xc}}{2}\cos\theta & \frac{\Delta_{xc}}{2}\sin\theta e^{-i\phi} \\ 0 & 0 & \frac{\Delta_{xc}}{2}\sin\theta e^{i\phi} & -\frac{\Delta_{xc}}{2}\cos\theta \end{bmatrix} \Theta(z)$$

$$+\begin{bmatrix}1&0&0&0\\0&1&0&0\\0&0&-1&0\\0&0&0&-1\end{bmatrix}(Vd\delta(z)-\mu\Theta(z)-\mu_{sc}\Theta(-z))+\begin{bmatrix}0&0&1&0\\0&0&0&1\\1&0&0&0\\0&1&0&0\end{bmatrix}\Delta\Theta(-z) \tag{4.37}$$

$$+\begin{bmatrix}0&i\lambda_R e^{-i\phi}+\lambda_D e^{i\phi}&0&0\\-i\lambda_R e^{i\phi}+\lambda_D e^{-i\phi}&0&0&0\\0&0&0&i\lambda_R e^{-i\phi}+\lambda_D e^{i\phi}\\0&0&-i\lambda_R e^{i\phi}+\lambda_D e^{-i\phi}&0\end{bmatrix}k_{\|}\delta(z).$$

Now, integrate from $-b$ to b,

$$\begin{bmatrix}1&0&0&0\\0&1&0&0\\0&0&-1&0\\0&0&0&-1\end{bmatrix}\left(-\frac{\hbar^2}{2m}\right)\int_{-b}^{b}\frac{d^2\Psi(z)}{dz^2}dz-\begin{bmatrix}1&0&0&0\\0&1&0&0\\0&0&-1&0\\0&0&0&-1\end{bmatrix}\mu\int_{-b}^{b}\Theta(z)\Psi(z)dz-$$

$$\begin{bmatrix}1&0&0&0\\0&1&0&0\\0&0&-1&0\\0&0&0&-1\end{bmatrix}\mu_{sc}\int_{-b}^{b}\Theta(-z)\Psi(z)dz+\begin{bmatrix}1&0&0&0\\0&1&0&0\\0&0&-1&0\\0&0&0&-1\end{bmatrix}Vd\int_{-b}^{b}\delta(z)\Psi(z)dz+$$

$$\begin{bmatrix} -\frac{\Delta_{xc}}{2}\cos\theta & -\frac{\Delta_{xc}}{2}\sin\theta e^{-i\phi} & 0 & 0 \\ -\frac{\Delta_{xc}}{2}\sin\theta e^{i\phi} & \frac{\Delta_{xc}}{2}\cos\theta & 0 & 0 \\ 0 & 0 & \frac{\Delta_{xc}}{2}\cos\theta & \frac{\Delta_{xc}}{2}\sin\theta e^{-i\phi} \\ 0 & 0 & \frac{\Delta_{xc}}{2}\sin\theta e^{i\phi} & -\frac{\Delta_{xc}}{2}\cos\theta \end{bmatrix} \int_{-b}^{b} \Theta(z)\Psi(z)dz +$$

$$\begin{bmatrix} 0 & i\lambda_R e^{-i\phi} + \lambda_D e^{i\phi} & 0 & 0 \\ -i\lambda_R e^{i\phi} + \lambda_D e^{-i\phi} & 0 & 0 & 0 \\ 0 & 0 & 0 & i\lambda_R e^{-i\phi} + \lambda_D e^{i\phi} \\ 0 & 0 & -i\lambda_R e^{i\phi} + \lambda_D e^{-i\phi} & 0 \end{bmatrix} k_{\|} \int_{-b}^{b} \delta(z)\Psi(z)dz \tag{4.38}$$

$$+ \begin{bmatrix} 0 & 0 & 1 & 0 \\ 0 & 0 & 0 & 1 \\ 1 & 0 & 0 & 0 \\ 0 & 1 & 0 & 0 \end{bmatrix} \int_{-b}^{b} \Delta\Theta(-z)\Psi(z)dz = \int_{-b}^{b} E\Psi(z)dz.$$

Let $b \to 0$, and do the integration,

$$\begin{bmatrix} 0 \\ 0 \\ 0 \\ 0 \end{bmatrix} = -\frac{\hbar^2}{2m} \begin{bmatrix} 1 & 0 & 0 & 0 \\ 0 & 1 & 0 & 0 \\ 0 & 0 & -1 & 0 \\ 0 & 0 & 0 & -1 \end{bmatrix} \left(\frac{\partial \Psi^{\sigma}_{S_{FM}}}{\partial z}|_{z=0^+} - \frac{\partial \Psi^{\sigma}_{F_{FM}}}{\partial z}|_{z=0^-} \right) +$$

$$\begin{bmatrix} Vd & k_\parallel(i\lambda_R e^{-i\phi} + \lambda_D e^{i\phi}) & 0 & 0 \\ k_\parallel(-i\lambda_R e^{i\phi} + \lambda_D e^{-i\phi}) & Vd & 0 & 0 \\ 0 & 0 & -Vd & k_\parallel(i\lambda_R e^{-i\phi} + \lambda_D e^{i\phi}) \\ 0 & 0 & k_\parallel(-i\lambda_R e^{i\phi} + \lambda_D e^{-i\phi}) & -Vd \end{bmatrix} \Psi^\sigma_{F_{FM}}|_{z=0^-}. \quad (4.39)$$

The boundary conditions displayed in equation 4.35 and 4.39 give four equations each, resulting in a total of eight equations. These eight equations can most easily be solved numerically. Using Mathematica, start by writing in the expressions for the wave functions $\Psi^\sigma_{F_{FM}}$ and $\Psi^\sigma_{S_{FM}}$, as well as the wave vectors and interface elements in terms of the spin-orbit coupling and scalar barrier expressions. Then differentiate the wave functions and insert numerical values for all the parameter values that are not to be varied later during plotting or integration. The results are presented using the dimensionless variables $Z = \frac{Vdm}{\hbar^2 k_F}$, $\lambda_{RSO} = \frac{2m\lambda_R}{\hbar^2}$, $\lambda_{DSO} = \frac{2m\lambda_D}{\hbar^2}$, and $P = \frac{\Delta_{xc}}{2E_F}$.

With values set, use *NSolve* to get an expression for all the probability amplitudes in $\boldsymbol{P}_a = \left[r_{e,\sigma}, r_{e,-\sigma}, r_{h,\sigma}, r_{h,-\sigma}, t_{e,\sigma}, t_{e,-\sigma}, t_{h,\sigma}, t_{h,-\sigma}\right]$. The terms of $\boldsymbol{P}_a$ will have to be squared to get $|r_{e(h),\sigma}|^2$, $|r_{e(h),-\sigma}|^2$, $|t_{e(h),\sigma}|^2$, and $|t_{e(h),-\sigma}|^2$, and then multiplied with their respective $\hat{z}$-directional wave vectors to yield the probabilities for the different scattering processes [21],

$$R_{e(h)}(E, k_p) = \mathrm{Re}[k_z^{e(h),\sigma}|r_{e(h),\sigma}|^2 + k_z^{e(h),-\sigma}|r_{e(h),-\sigma}|^2] \quad (4.40)$$

and

$$T_{e(h)}(E, k_p) = \mathrm{Re}[q_z^{e(h)}|t_{e(h),\sigma}|^2 + q_z^{e(h)}|t_{e(h),-\sigma}|^2]. \quad (4.41)$$

Here $R_{e,\sigma}$ is the NR probability, $R_{h,\sigma}$ is the AR probability, $T_{e,\sigma}$ is the TE probability, and $T_{h,\sigma}$ is the TH probability.

4.5 Reflection and Transmission Probabilities

In this section the chemical potential in the ferromagnet and superconductor are set equal to $\mu = \mu_{sc} = E_F$, which will be correct at $T = 0K$. This assumption is usually reasonable since most

superconductors will need very low temperatures to be superconducting. Since the ferromagnet is connected to the superconductor it is also reasonable to assume that the temperature around it will be very low. Further, it is assumed that $E_F = \frac{\hbar^2 k_F^2}{2m}$. All the wave vectors and eigenvectors are then normalized by E_F, and $\epsilon = \frac{E}{E_F}$ and $k_p = \frac{k_\parallel}{k_F}$. The polarization $P = \frac{\Delta_{xc}}{2E_F}$ is chosen in between $P = 0$ (normal metal) and $P = 0.6$, with the aim of avoiding any non-trivial behavior. By changing the material composition other values for the constants could have been chosen.

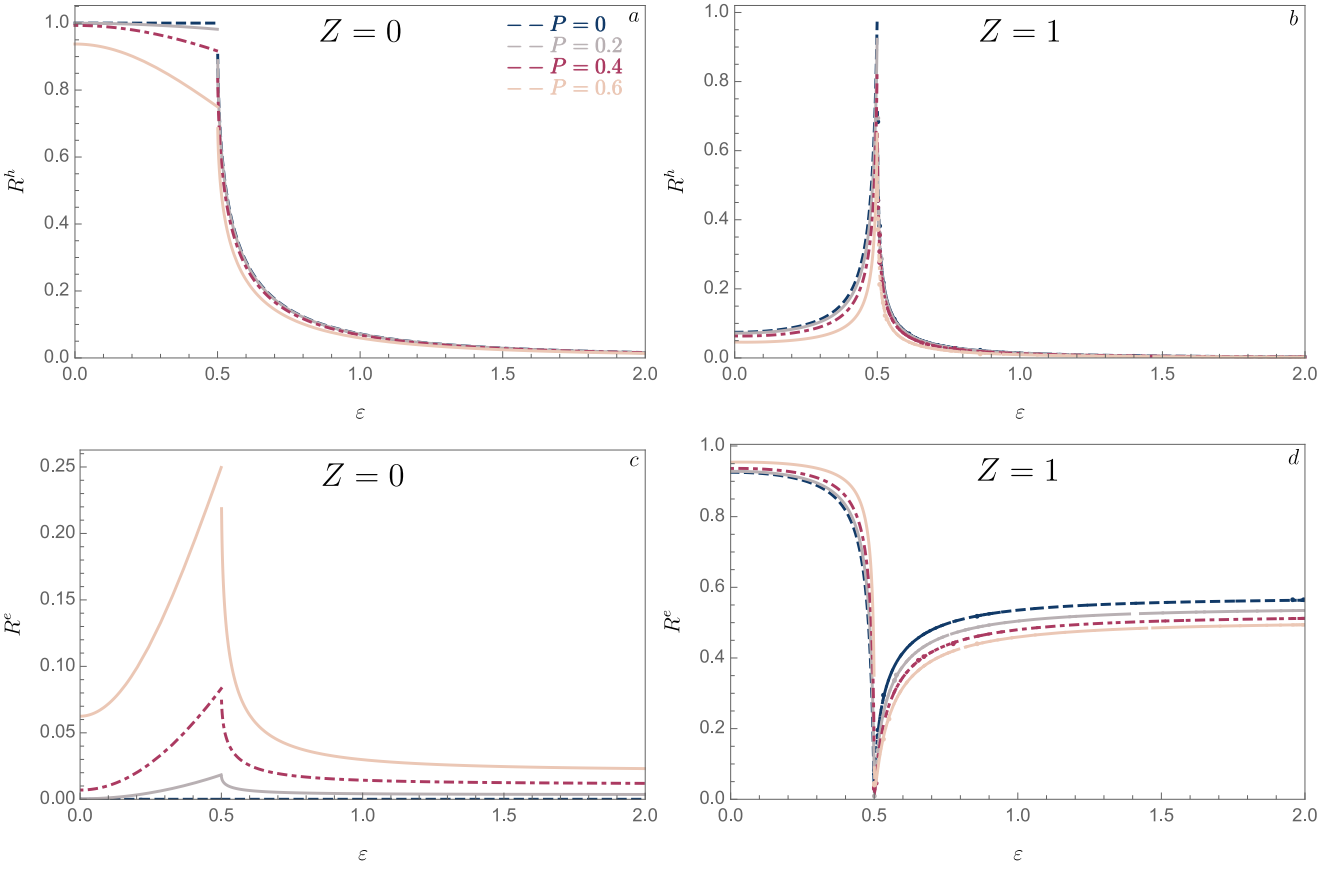

Figure 4.6: The AR and NR probability for varying energies and polarizations. The normalized parallel wave vector is chosen to be $k_p = 0.5$, the Rashba spin-orbit coupling $\lambda_{RSO} = 0$, the polar angle is $\theta = \frac{\pi}{2}$, the azimuthal angle is $\phi = 0$ and the normalized superconducting gap is $\Delta = 0.5$.

In Figure 4.6 the probabilities for AR (R^h) and NR (R^e) for varying conditions are displayed. First notice that the probability for AR is 1 and NR is 0 in the case of $P = 0$ and $Z = 0$. This is a normal metal superconductor junction with no scalar barrier. Without scalar barrier and polarization there will be no NR, and since the electrons will need a given energy to tunnel

through the interface the AR probability will have to be 1 up to a given critical energy, which in this case is $\epsilon \approx 0.5$. Next notice that a higher polarization makes the AR probability decrease towards the critical limit, but for higher energies it behaves as in the case of $P = 0$. The decrease in AR probability seems to result in a subsequent increase in NR probability such that the total reflection amplitude is 1 up to the critical energy limit. This means that in this case the polarization does not affect the ratio between reflection and tunneling, but rather the ratio between AR and NR.

In the case of $Z = 1$, the probability for NR is close to 1, while the AR probability is very low in the low energy regime. This is in accordance with what is previously known about the relationship between NR and scalar barrier; the stronger the scalar barrier the more NR. Further, observe a maximum point at $\epsilon \approx 0.5$ in the AR behavior. This means that for a given parallel wave vector, it seems to be a particular energy that is very favorable for AR. Summing together the reflection probabilities it can be seen that the total probability for reflection is 1 at energies below the critical energy. This means that the electrons still need a given energy to be able to tunnel through the interface, and that the scalar barrier does not reduce that energy. Contrary to the case of $Z = 0$, non-zero NR probabilities in the high energy regime can be observed, which reinforce the fact that a higher scalar barrier means more NR.

In Figure 4.7 the Andreev and NR probabilities for varying polarizations, scalar barriers and parallel wave vectors are displayed. First, notice that, in the case of $P = 0$ and $Z = 0$, the probability for AR is 1 up to a parallel wave vector cutoff at $k_p = 1$. This cutoff is because the parallel wave vector has to be between 0 and $\sqrt{1 \pm P}$, which becomes evident from Figure 4.7. Looking back at Figure 4.6, one can compare the numbers seen at $\epsilon = 0.5$ with the ones seen at at $k_p = 0.5$ in Figure 4.7; they are the same. Next, observe that for $P = 0$ there will be zero probability for NR for all values of the parallel wave vector. However, at higher polarizations the NR probability grow exponentially towards the cutoff wave vector making the total reflection probability equal to 1, which is in agreement with Figure 4.6.

In the case of $Z = 1$, the probabilities look exactly the same as in the case of $Z = 0$. This may appear strange at first, but looking back at Figure 4.6 one can confirm the numbers at $k_p = 0.5$. Another key insight from Figure 4.6 is that $\epsilon = 0.5$ is a special case for which the probabilities for $Z = 0$ and $Z = 1$ match. By looking at the probabilities at for example $\epsilon = 0.4$ in Figure 4.7 the graphs for $Z = 0$ and $Z = 1$ would have looked different.

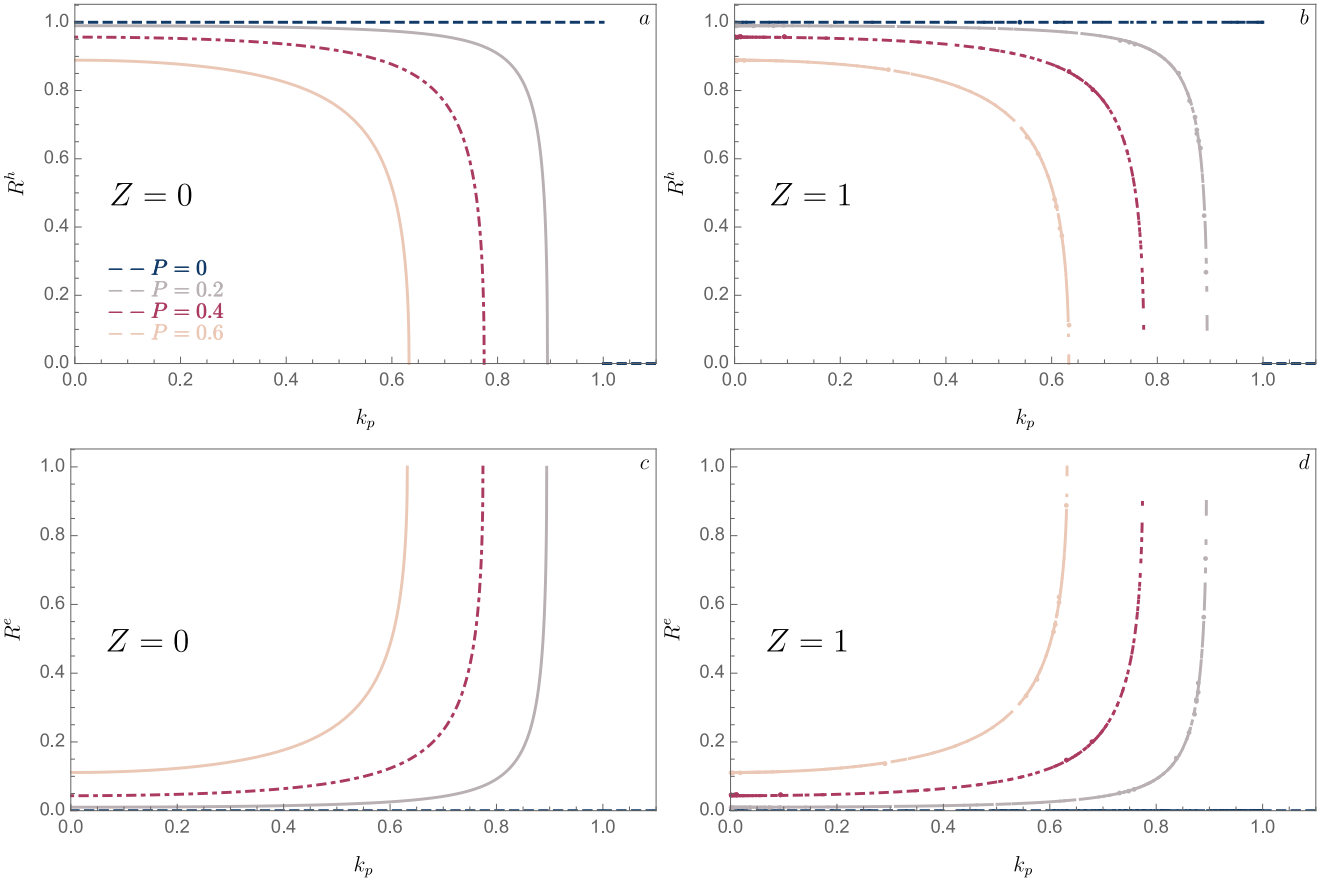

Figure 4.7: The AR and NR probability for varying parallel wave vectors and polarizations. The normalized energy is chosen to be $\epsilon = 0.5$, the Rashba spin-orbit coupling $\lambda_{RSO} = 0$, the polar angle is $\theta = \frac{\pi}{2}$, the azimuthal angle is $\phi = 0$ and the normalized superconducting gap is $\Delta = 0.5$.

4.6 Thermal Conductivity

To get a broader foundation for assessing the quality of the FS junction, TC will be calculated. TC describes a material's ability to transfer heat, and can be calculated using [21],

$$\kappa = \sum_{\sigma} \int_0^{\infty} \int_s \frac{d^2k_{\parallel}}{2\pi k_F^2} [1 - R_{e,\sigma} - R_{h,\sigma}] \frac{(E - E_F)^2}{T^2 \cosh^2\left(\frac{E-E_F}{2k_B T}\right)} dE, \tag{4.42}$$

where the integration with respect to $k_{\parallel}$ is taken over the entire xy-interface. Equation 4.42 is solved for varying values of polarization, spin-orbit field strength, scalar barrier strength and temperature to assess whether a certain set of conditions can make the FS hybrid junction a suitable thermoelectric material.

In figure 4.8, TC at changing conditions can be seen. First, observe that increasing temperature will increase TC exponentially. This is due to the superconducting gap, which decreases with increasing temperature. The greater the superconducting gap, the more AR there will be in the material. At $Z = 0$, there is no NR, and when the temperature increases there will be a lower superconducting gap, and hence less AR and more TE. These factors make the thermal resistance drop exponentially, and thereby the thermal conductance increase exponentially [21]. A similar behavior is seen for higher Z, were also the reduction in the superconducting gap results in a higher ratio of tunneling over reflection. In general, the higher the ratio of tunneling over reflection the higher the TC will be, see equation 4.42, since the total probability for reflection plus the total probability for tunneling has to be 1.

Next, observe that increasing the scalar barrier strength Z will decrease TC. A higher scalar barrier means more NR, so it is natural to assume that increasing Z will make a portion of the otherwise transmitted electrons being normal reflected back into the ferromagnet. Further, a cross-over temperature can be observed where the lines cross each other. At lower temperatures, higher polarization means higher TC, while at higher temperatures lower polarizations means higher TC. The cross-over temperature seems to move towards higher temperatures as the scalar barrier strength is increased.

In the case of $P = 0$, the FS hybrid junction will be equivalent to a normal metal-superconductor junction. In such a material combination, the sub-gap contribution to the TC is 0 [21]. This is because the AR probability is 1 in the sub-gap regime, making the probability for tunneling 0. Looking at equation 4.42, it becomes evident that a higher probability for tunneling will increase TC, and that a 0 probability for tunneling means 0 TC. Taking all this into account, it becomes evident that the sub-gap regime contributions to the TC has to be 0.

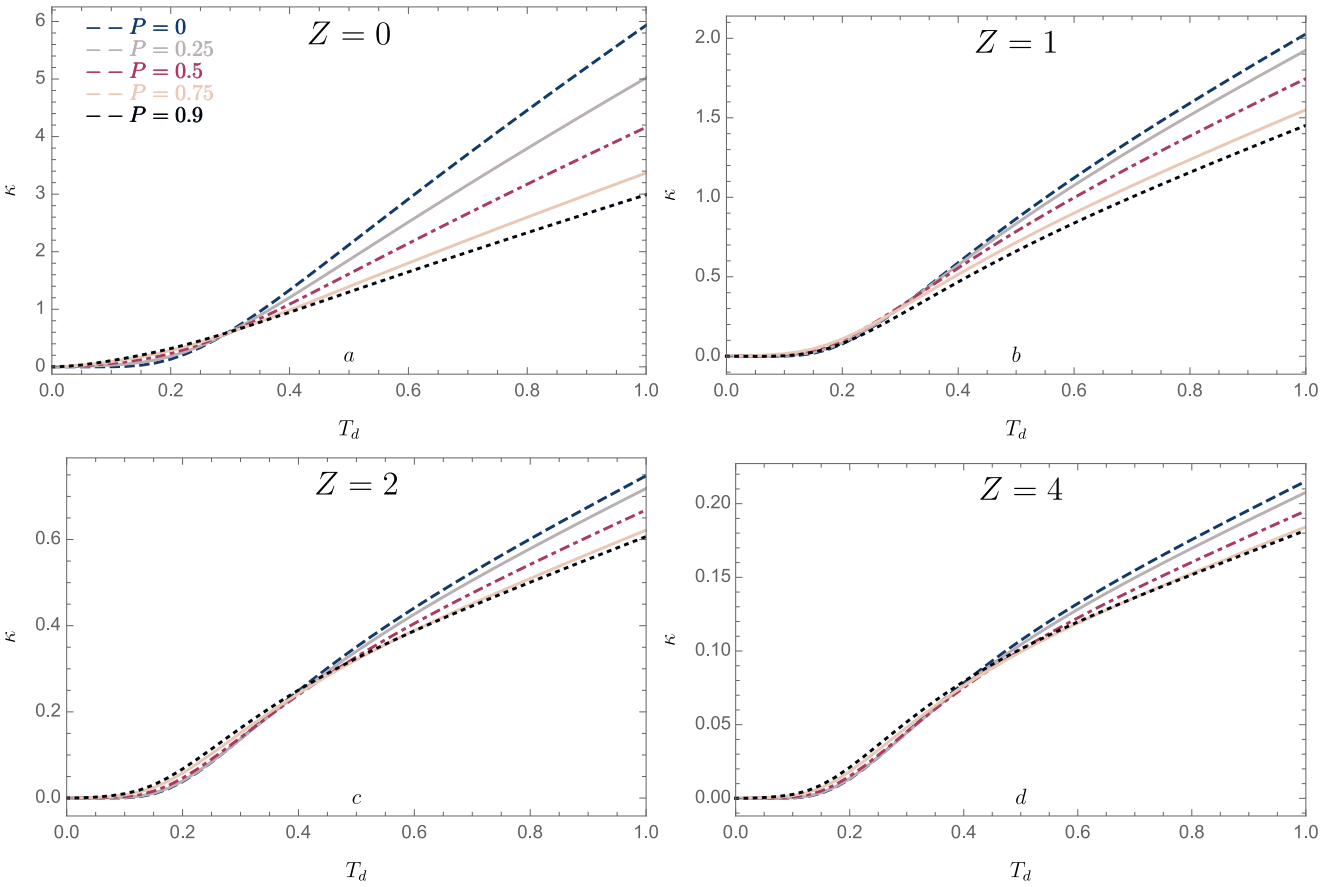

Figure 4.8: The TC for varying temperature, scalar barrier strengths, spin-orbit coupling strengths and polarizations. The Rashba spin-orbit coupling is $\lambda_R = 0$, the Dresselhaus spin-orbit coupling is $\lambda_D = 0$, the polar angle is $\theta = \pi/2$, the Fermi wave vector is $k_F = 1$, the superconducting gap is $\Delta = 1$, the azimuthal angle is $\phi = 0$, and the dimensionless temperature is $T_d = \frac{T}{T_{crit}}$.

From Figure 4.9 it can be learned that the behaviour of TC differ with varying scalar barrier strength. In the case of $Z = 0$, a decrease in TC is observed as the ratio of Rashba spin-orbit interaction (RSOI) over Dresselhaus spin-orbit interaction (DSOI) is increased. Increasing RSOI while keeping the DSOI at 1 means more spin-orbit coupling in total. Including spin-orbit coupling makes the probabilities for the spin-flipping processes non-zero.

Now, setting $Z = 1$, the TC is reduced. This is because the total reflection probability will increase due to an increase in NR probability. The same behavior can be found also when going

from $Z = 1$ to $Z = 2$, and then further to $Z = 4$. In most cases for $Z > 0$, it can be seen that the TC increases with increasing λ_R. This means that at some value for Z, the interplay between Z and the ratio between Rashba and Dresselhaus SOI will make TC go from being decreasing in nature to become increasing in nature.

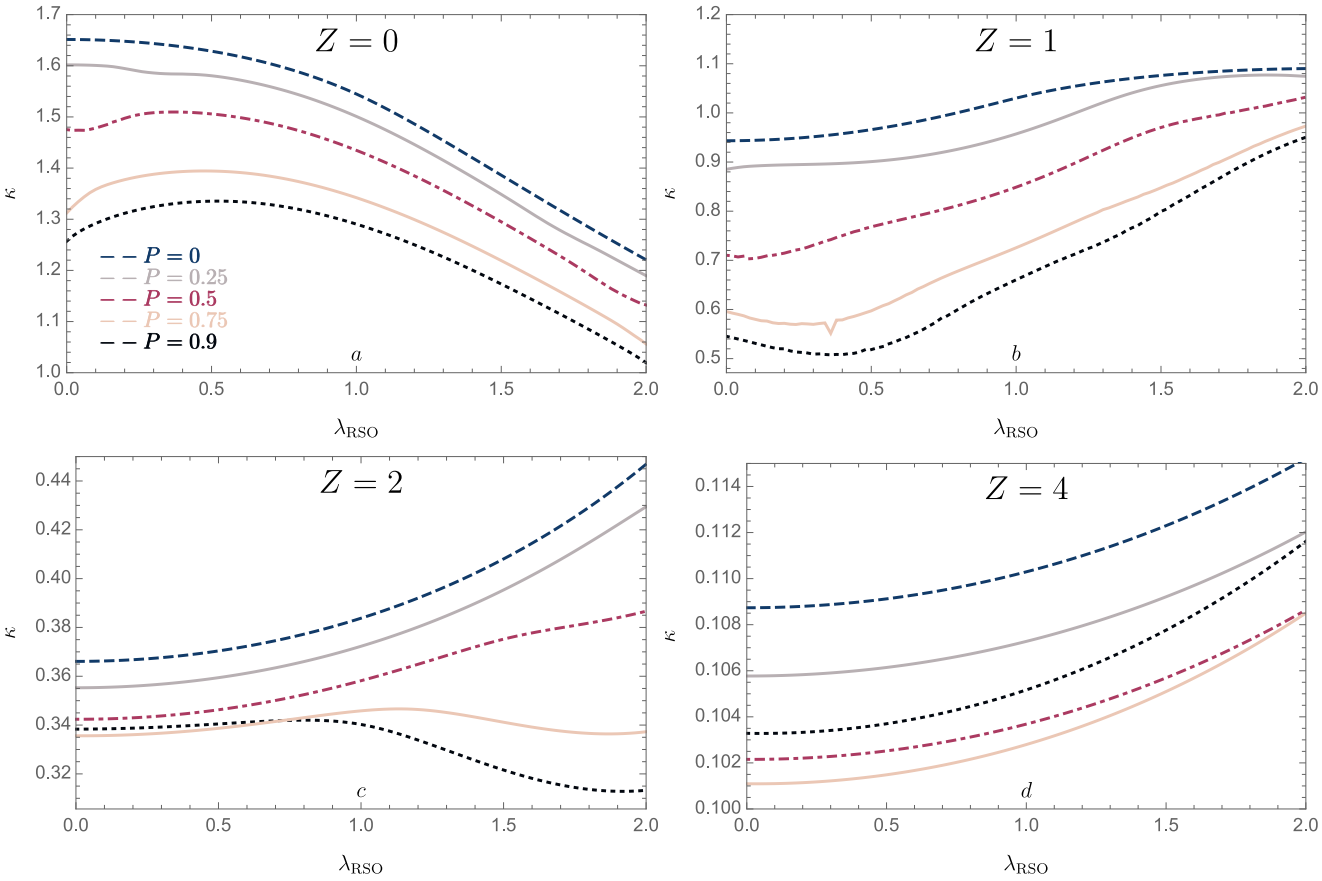

Figure 4.9: The TC for varying scalar barrier strengths, spin-orbit coupling strengths and polarizations. Here, the Dresselhaus spin-orbit coupling strength is $\lambda_D = 1$, the polar angle is $\theta = \frac{\pi}{2}$, the Fermi wave vector is $k_F = 1$, the azimuthal angle is $\phi = 0$, the superconducting gap is $\Delta = 1$, and the normalized temperature $T_d = 0.5$.

To investigate how the polarization affect TC, it can be recognized that a higher value for the polarization means a reduction in AR due to the minority spin subband [21]. Further, tunneling corresponding to the minority spin subband reduces, which consequently reduces the TC. One can therefore observe that usually the greater the P the lower the κ.

By plotting TC for $\lambda_R = 1$ and varying Dresselhaus spin-orbit coupling strengths, a plot identical with Figure 4.9 will be obtained, see Appendix C. This means that a similar increase in $\frac{\lambda_D}{\lambda_R}$ and $\frac{\lambda_R}{\lambda_D}$ will affect the probabilities for NR and AR equally much.

4.7 Seebeck Coefficient

Electrons are both carriers of electricity and heat, and SkC takes that into account. It describes the thermoelectrical voltage that is induced in a material as a result of a temperature difference across it. If a higher voltage is induced, there will be more electrons moving across the material, and hence a stronger current. It is therefore apparent that a high SkC is crucial for devices that convert heat to electricity, since a device with a high SkC will be able to convert more heat to energy. By looking at the linear response regime, the SkC can be found as [21],

$$SkC = -\left(\frac{V}{\delta T}\right)_{I=0} = -\frac{\alpha}{T_d G}. \tag{4.43}$$

Here, α is the thermoelectric coefficient, G is the electrical conductance in units of $G_0(\frac{e^2}{h})$, the integration with respect to $k_\parallel$ is taken over the entire xy-interface, and $T_d = \frac{T}{T_{crit}}$.

$$\alpha = \sum_\sigma \int_0^\infty \int_s \frac{d^2k_\parallel}{2\pi k_F^2}[1 - R_{e,\sigma} - R_{h,\sigma}] \left[\frac{(E - E_F)}{T\cosh^2(\frac{E-E_F}{2k_BT})}\right] dE \tag{4.44}$$

and

$$G = \sum_\sigma \int_0^\infty \int_s \frac{d^2k_\parallel}{2\pi k_F^2} \left[\frac{1 + R_{e,\sigma} - R_{h,\sigma}}{T\cosh^2(\frac{E-E_F}{2k_BT})}\right] dE, \tag{4.45}$$

where the thermoelectric coefficient is given in terms of units $\frac{G_0 k_B T}{e} = \frac{k_B e T}{h}$.

In Figure 4.10, notice that the SkC is negative for the majority of the conditions displayed. This is because the contributions are solely from electrons [21]. From equation 4.43, it is obvious that the less AR that is present, the more negative the SkC will be. Higher temperatures decreases the magnitude of the superconducting gap, which again decreases AR. Therefore, it makes sense that SkC becomes more negative for increasing temperatures in the case of $Z = 0$. For $Z > 0$,

there will be a non-zero NR probability. A higher probability for NR will decrease both α and G in equation 4.43, and therefore the effect on the SkC will depend on their relative magnitudes.

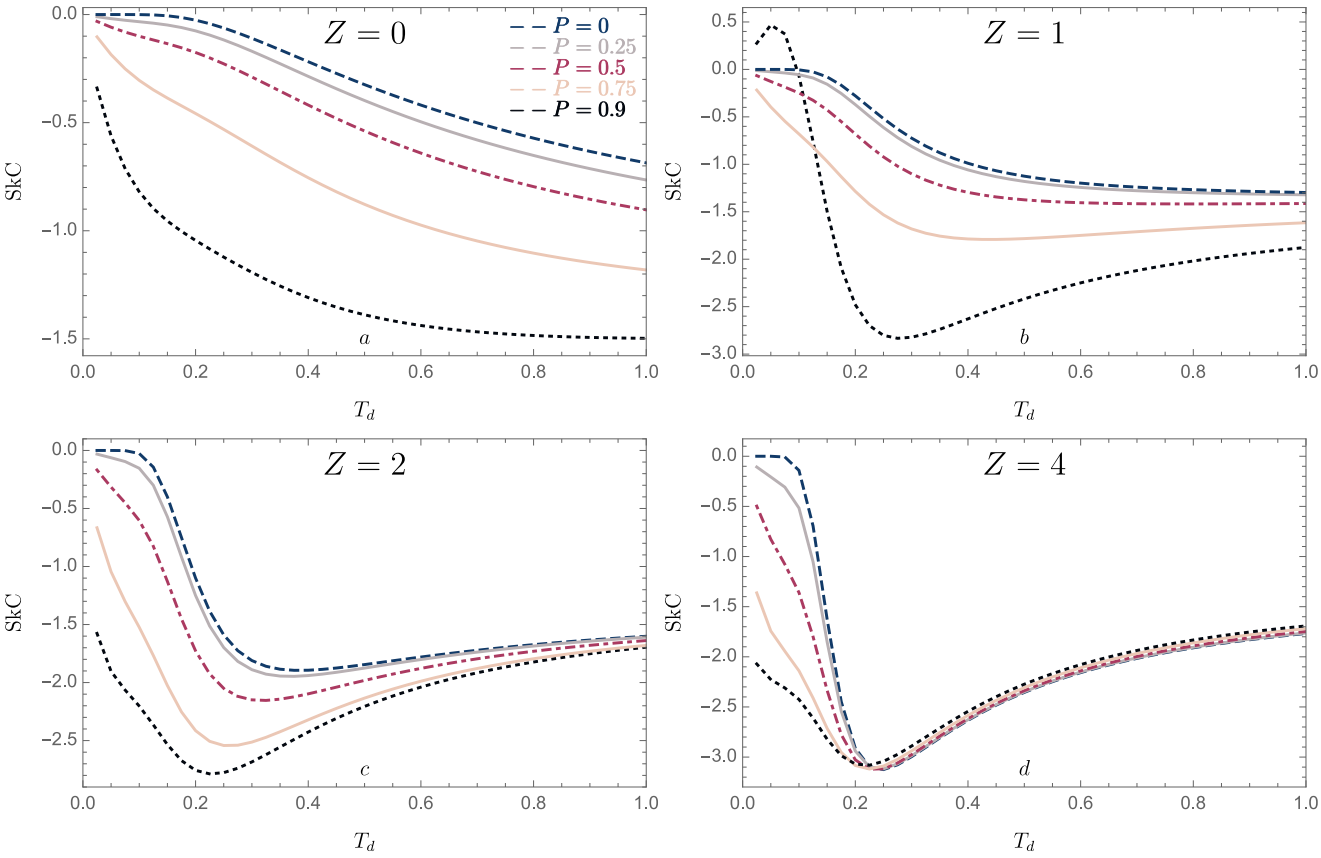

Figure 4.10: Here, the Rashba spin-orbit coupling strength is $\lambda_R = 0$, the Dresselhaus spin-orbit coupling strength is $\lambda_D = 0$, the polar angle is $\theta = \pi/2$, the Fermi wave vector is $k_F = 1$, the superconducting gap is $\Delta = 1$, the azimuthal angle is $\phi = 0$, and the normalized temperature $T_d = \frac{T}{T_{crit}}$.

Looking at the effect the polarization has on the SkC, it can be observed that a higher polarization tend to make the SkC more negative in the low temperature regime. At high temperatures the superconducting gap is reduced considerably, resulting in an increase in conductance. After a certain temperature, G will not increase with a pronounced amount anymore due to the absence of a minority spin band. This makes SkC less negative towards higher temperatures. The presented behavior is more pronounced in the case of a high scalar barrier, for which an extremum point is found. It seems like a higher scalar barrier, and therefore higher probability of NR, tend to make

the extremum point in the Seebeck profile more negative. Further, it can be noticed that, while approaching higher temperatures, the values for the SkC saturates towards a given magnitude irrespective of the polarization.

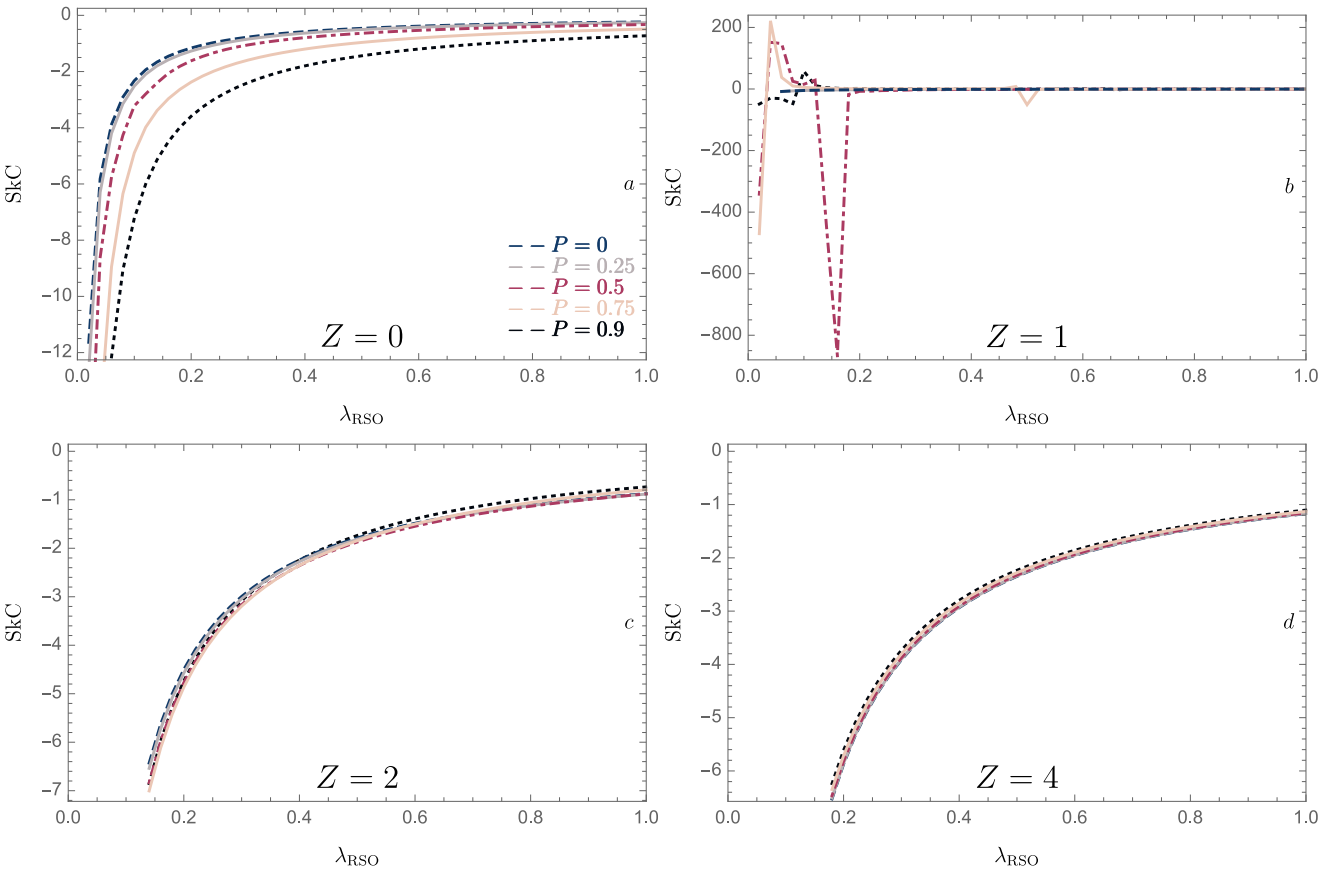

Figure 4.11: The SkC for varying scalar barrier strengths, spin-orbit coupling strengths and polarizations. Here, the Dresselhaus spin-orbit coupling strength is $\lambda_D = 1$, the polar angle is $\theta = \frac{\pi}{2}$, the Fermi wave vector is $k_F = 1$, the azimuthal angle is $\phi = 0$, the superconducting gap is $\Delta = 1$, and the normalized temperature $T_d = 0.5$.

In figure 4.11 the SkC for varying conditions is shown. First, observe that for even Z, the SkC is negative for all values of P and λ_R. This is most likely because all of the contributions are from electrons. Since a more negative SkC imply that a material is able to convert more heat to energy, a low value for Rashba spin-orbit coupling is desirable when making a heat to energy converter. By looking at Figure 4.11, it can be seen that SkC becomes more negative towards lower values of λ_R, which exemplify that spin-orbit coupling in general seems to be unfavorable

in cases where a highly negative SkC is sought for. This is also supported by the results from [21]. Next, observe that at greater values for Z the graphs seems to move slightly towards higher RSOI values.

For $Z = 0$, an increase in polarization seems to make SkC more negative. This is because a higher polarization will give more AR. Looking at equation 4.43, 4.44 and 4.45, it can be understood that a higher probability for AR will decrease the thermoelectric coefficient and increase the electric conductance, resulting in a more negative SkC. At higher Z, NR becomes important, and TC seems to be more or less independent of polarization.

In the case of $Z = 1$, it seems like SkC has a highly irregular behavior. At low ratios of RSOI to DSOI, SkC varies from about approximately -850 to 200, while at higher ratios it becomes 0. Also in the case of the SkC, it seems like there is no difference if you plot it against $\frac{\lambda_D}{\lambda_R}$ or $\frac{\lambda_R}{\lambda_D}$, see Figure C.2.

4.8 Figure of Merit

Recently there has been tremendous effort into producing better thermoelectric devices [32, 72], devices that can convert heat to electricity or electricity to heat. The world experiences a continually increasing demand for energy, and more efficient thermoelectric materials can help us extract more energy from waste heat. The efficiency of a thermoelectric material is determined by the FOM, which can be calculated combining equation 4.42, 4.43, 4.44 and 4.45,

$$FOM = SkC^2 \frac{GT}{K}, \tag{4.46}$$

where $K = \kappa - \frac{\alpha^2}{TG}$ and is expressed in units $\frac{k_B^2 T}{h}$.

As is evident from Figure 4.12, FOM is increasing with increasing temperature in the low temperature regime. However, in the high temperature regime FOM is decreasing for $Z > 0$. The maxima appear at approximately the same temperature for all four values of Z. Looking a the polarization, it can be demonstrated that higher polarization means higher FOM, and the same trend can be found for an increase in scalar barrier strength. In the search for good thermoelectric materials, scientist have been looking for materials with $FOM > 1$, and from Figure 4.12 it can be seen that the FS junction has multiple conditions that satisfy this. Further, FOM seems to become less sensitive to polarization for higher scalar barrier strengths.

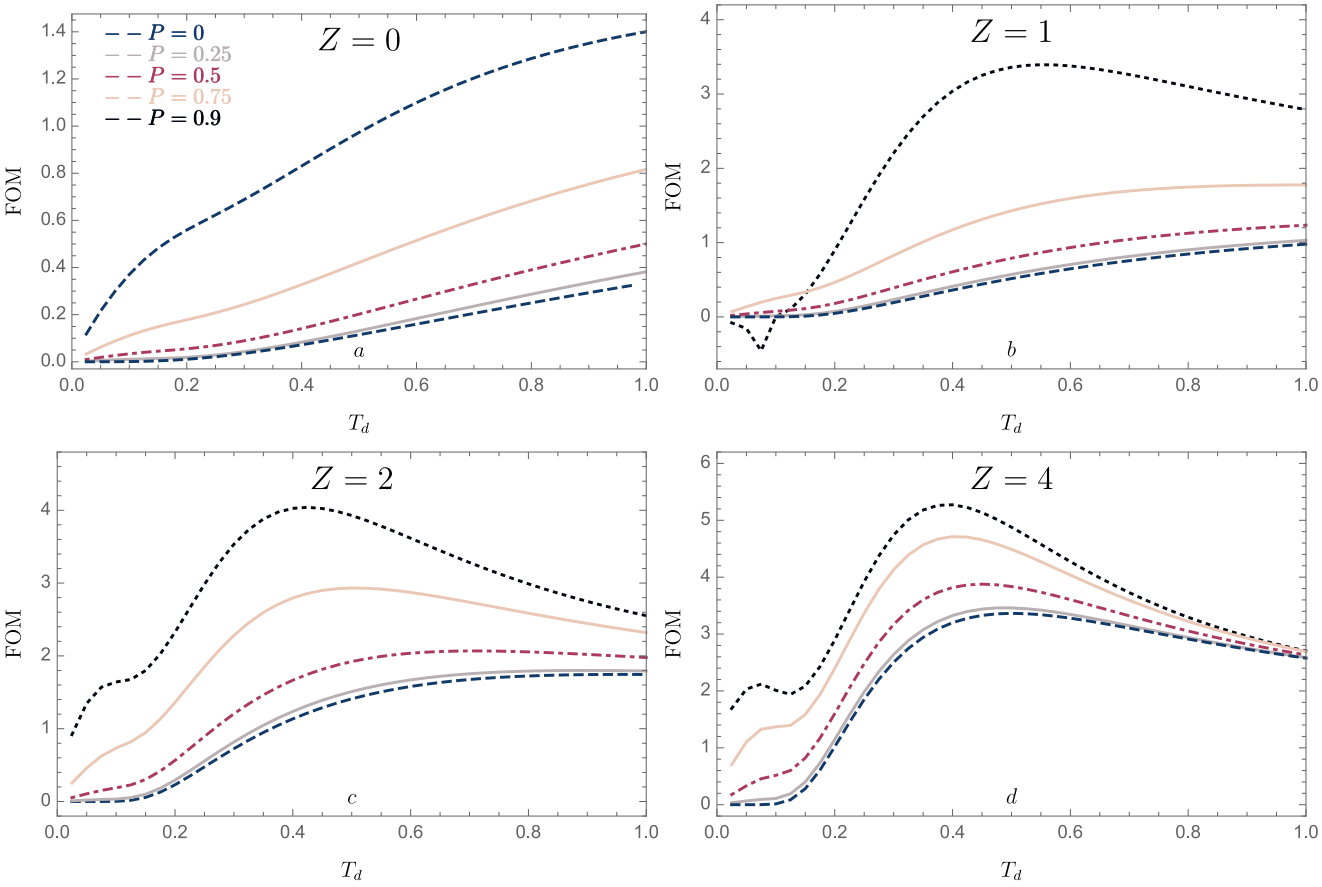

Figure 4.12: The FOM for varying scalar barrier strengths, spin-orbit coupling strengths and polarizations. Here, Rashba spin-orbit coupling strength is set to $\lambda_R = 0$, Dresselhaus spin-orbit coupling strength is $\lambda_D = 0$, the polar angle is $\theta = \pi/2$, the Fermi wave vector is $k_F = 1$, the superconducting gap is $\Delta = 1$, the azimuthal angle is $\phi = 0$, and the normalized temperature $T_d = \frac{T}{T_{crit}}$.

In Figure 4.13 the FOM for varying values of λ_R is displayed. First, observe that the FOM is close to zero for most choices of P, Z and λ_R. This imply that in order to have an effective thermoelectrical material, it is extremely important to have the correct ratio of Rashba spin-orbit coupling to Dresselhaus spin-orbit coupling. Typically, it decreases exponentially toward a given value for λ_R, before it increases sharply and then again decreases exponentially towards 0. Further, it seems to be a loose trend towards higher deviations from $FOM = 0$ for higher values of P, with a few exceptions. At higher scalar barrier strengths, the curves for the different polarizations seems to move closer to each other and be nonzero for a shorter range of λ_R

values. This signify that by choosing a low scalar barrier, it will be easier to tune the material combination in such a way that a high FOM will be achieved, and thereby a good thermoelectric material. The range for FOM values goes from approximately -60 to 80 throughout the four plots. Also for FOM a similar increase in $\frac{\lambda_D}{\lambda_R}$ and $\frac{\lambda_R}{\lambda_D}$ will affect the probabilities of NR and AR equally, see Figure C.3, given that their start values are equal.

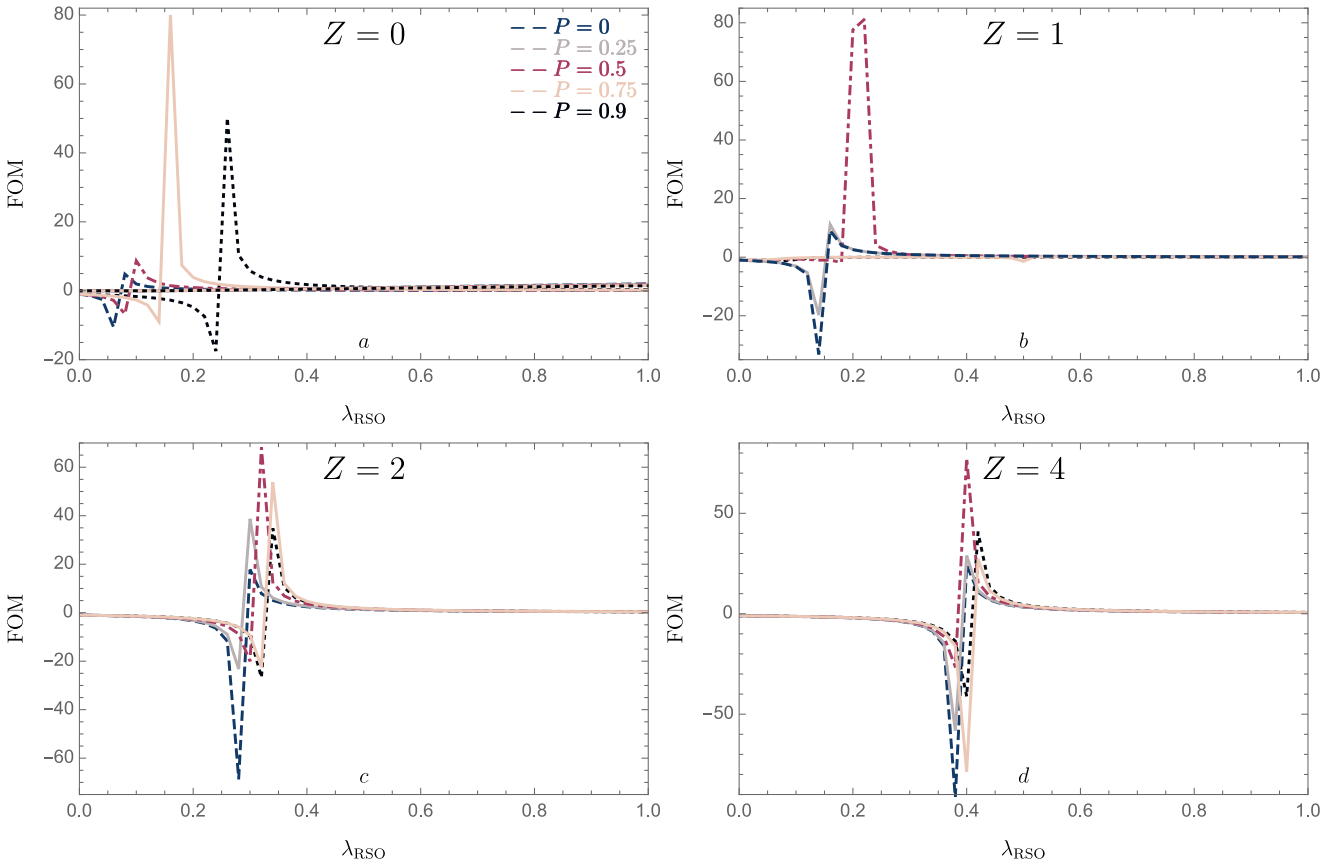

Figure 4.13: The FOM for varying scalar barrier strengths, Rashba spin-orbit coupling strengths and polarizations. Here, Dresselhaus spin-orbit coupling strength is $\lambda_D = 1$, the polar angle is $\theta = \frac{\pi}{2}$, the Fermi wave vector is $k_F = 1$, the azimuthal angle is $\phi = 0$, the superconducting gap is $\Delta = 1$, and the normalized temperature $T_d = 0.5$.

4.9 Ferromagnet-Superconductor Hybrid Junction

The behaviour of TC, SkC and FOM under different circumstances has been investigated. In the production of thermoelectric devices, engineers usually look for materials with high a FOM. Looking back at Figure 4.12 and 4.13, a high degree of polarization and scalar barrier is wanted if the ratio of Rashba and Dresselhaus spin-orbit coupling can be tuned precisely. If that is not the case, a lower Z should be chosen. Temperature wise, to make the FS hybrid junction a good thermometric material, the person that operates the thermoelectric device should aim for $T \approx 0.5T_{crit}$ given that $Z > 0$. The strength of the Rashba and Dresselhaus spin-orbit coupling should be tuned in order with Figure 4.13 so that the weakest of them is approximately 0.4 of the other one, given a high Z, see Figure 4.13 and C.3.

There might be situations where a high FOM is not what is wanted. Whether aiming for a high TC, SkC, FOM or any combination of the preceding, these figures will work as a toolbox for any person who want to make a thermoelectric device.

Chapter 5

Antiferromagnet-Superconductor Hybrid Junction

Scientists have taken interest in material compositions made up of superconductors and magnetic materials because many non-trivial phenomena occur at the interface between such materials. At present, most of the scientific effort have been focused on the FS junction, and less insight can be found on the AS junction. However, researchers have observed supercurrent in antiferromagnets [6, 67]. This might not be that surprising, since antiferromagnets do not create an internal field strong enough to destroy superconductivity [47]. It has actually been proposed that the antiferromagnetic interaction is crucial for pairing electrons in the superconducting state [49]. In the quaternary compound $HoNi_2B_2C$, it has been shown that the magnetic order that forms on cooling is oscillatory in nature and connected to the superconducting gap parameter. This oscillatory state is unfavorable to superconductivity, and the superconducting state only survives due to a first-order transition to a compensated antiferromagnet at low temperature [28].

In hybrid junctions made up of magnetic materials and superconductors, the proximity effect and inverse proximity effect are important phenomena [5]. These effects includes interactions between the order parameters of the magnet and superconductor. In an antiferromagnet, the Néel vector is often recognized as the order parameter, see Subsection 2.3.2. For a superconductor the magnitude of the superconducting gap is often considered the order parameter. The observation of weak superconductivity inside the magnet in an AS junction is referred to as the proximity effect. This phenomenon is quite surprising since a too strong magnetic field is well known for destroying superconductivity [39]. The inverse proximity effect include changes in the critical temperature and the superconducting energy gap, or an induction of antiferromagnetic order

inside the superconductor. The latter is often called the triplet proximity effect, since it result in spin mixing and spin rotation of singlet Cooper pairs, ultimately converting them into spin triplet Cooper pairs. Both proximity effects have been observed in hybrid structures of antiferromagnets and superconductors [7].

In this chapter, a schematic overview of the AS junction is presented together with an explanation of how the thermoelectric properties can be calculated. Invaluable in the derivation of the thermoelectric properties is the tight binding model which is used to derive a matrix Hamiltonian for the AS junction. This Hamiltonian is then used to find the eigenvectors and wave vectors of fermions in both the antiferromagnet and superconductor side. These are important elements of the wave function describing the particle behavior in the junction. By using the wave function and boundary conditions presented, the probabilities for four different scattering processes may be found and used to calculate thermoelectric properties such as TC, SkC and FOM.

5.1 Schematic Overview of the Junction

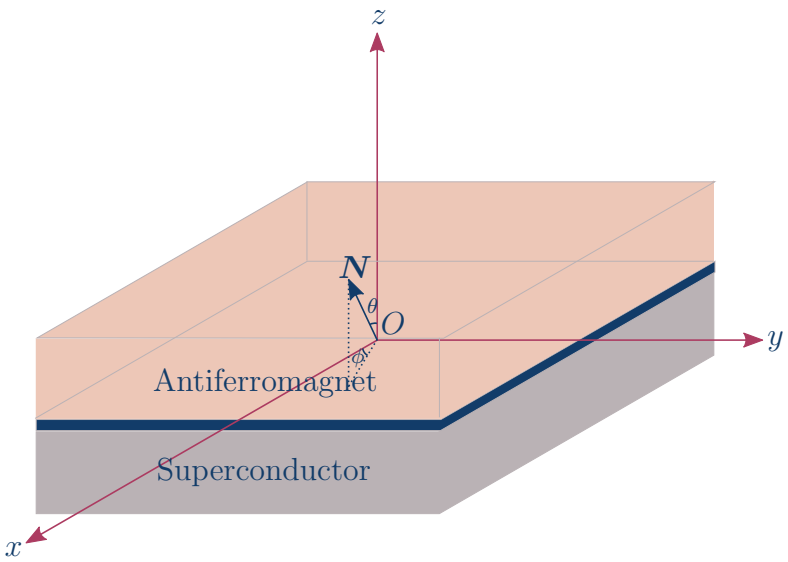

Figure 5.1: The model used in the calculations. Here, θ is the polar angle, ϕ is the azimuthal angle and O is the origin. Depicted from reference [33].

Here, the thermoelectric properties of AS hybrid junctions will be examined. The model is shown in Figure 5.1, and $z = 0$ is at the interface between the antiferromagnet and superconductor. Modified BTK theory is utilized to calculate the TC, FOM and SkC of this AS junction.

5.2 Scattering Mechanisms

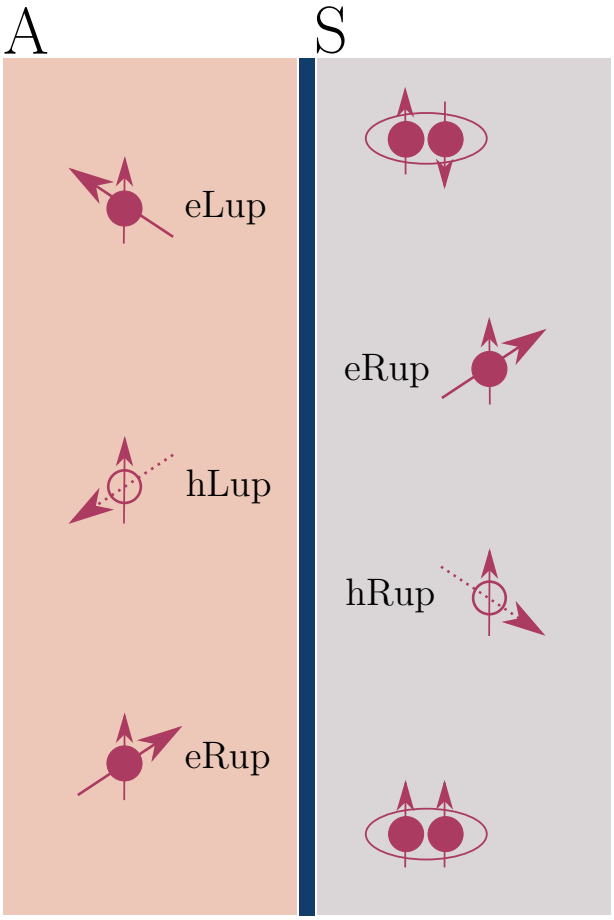

Figure 5.2: The possible scattering mechanisms in a FS hybrid structure. Here, e stand for electron and h for hole. L means that the particle is moving to the left, while R means that it moves to the right. Further, up means that the particle has spin up, and dn means that the particle has spin down. Depicted from reference [21, 33].

In the AS junction electrons with spin up (eRup) are shot into the antiferromagnet, where they scatter their way towards the interface between the antiferromagnet and superconductor. Also in this case there are four possible scattering mechanisms happening at the interface; AR, NR, TE, and TH. These processes are all displayed in Figure 5.2, and explained in greater detail in Section 4.2.

In the ferromagnetic case, spin-orbit interactions were included in the model, making the spin-flipping equivalents of the four above-mentioned processes possible. In the tight binding model described in Section 5.3, spin-orbit interactions are not included and the spin-flipping processes will therefore not occur. The spin-flipping processes are accordingly not included in Figure 5.2.

5.3 Tight Binding Model

The total Hamiltonian for the system is given by,

$$\mathcal{H}_{AS} = \mathcal{H}_K + \mathcal{H}_{AFM}\Theta(z) + \mathcal{H}_{sc}\Theta(-z), \tag{5.1}$$

where $\mathcal{H}_{AFM} = \mathcal{H}_{sd} + \mathcal{H}_\mu$ and $\mathcal{H}_{sc} = \mathcal{H}_\Delta + \mathcal{H}_{\mu_{sc}}$. Here $\mathcal{H}_K = -t_h \sum_{<i,j>,\delta,\sigma} c^\dagger_{i,\sigma} c_{j,\sigma}$, $\mathcal{H}_{sd} = J\sum_{i,\sigma} \boldsymbol{\sigma}\cdot\boldsymbol{M}_i c^\dagger_{i,\sigma} c_{i,\sigma}$, $\mathcal{H}_\mu = \mu \sum_{i,\sigma} c^\dagger_{i,\sigma} c_{i,\sigma}$, $\mathcal{H}_\Delta = (\sigma\Delta c^\dagger_{i,\sigma} c^\dagger_{i,-\sigma} + \sigma\Delta^\dagger c_{i,\sigma} c_{i,-\sigma})$, and $\mathcal{H}_{\mu_{sc}} = \mu_{sc}\sum_{i,\sigma} c^\dagger_{i,\sigma} c_{i,\sigma}$ [42]. Further, σ means spin up and $-\sigma$ means spin down. Now, set $\boldsymbol{M}_i = M^z_i \hat{z}$, and write the Hamiltonian utilizing creation and annihilation operators,

$$\begin{aligned}\mathcal{H}_{AS} = &- t_h \sum_{<i,j>,\delta,\sigma} c^\dagger_{i,\sigma} c_{j,\sigma} - \mu \sum_{i,\sigma} c^\dagger_{i,\sigma} c_{i,\sigma}\Theta(z) - \mu_{sc}\sum_{i,\sigma} c^\dagger_{i,\sigma} c_{i,\sigma}\Theta(-z) \\ &+ J\sum_{i,\sigma} M^z_i c^\dagger_{i,\sigma} c_{i,\sigma}\Theta(z) + \sum_{i,\sigma}(\sigma\Delta c^\dagger_{i,\sigma} c^\dagger_{i,-\sigma} + \sigma\Delta^\dagger c_{i,\sigma} c_{i,-\sigma})\Theta(-z),\end{aligned} \tag{5.2}$$

where t_h is the hopping energy, μ is the chemical potential of the ferromagnet, μ_{sc} is the chemical potential of the superconductor, Δ is the superconducting gap, $c^\dagger$ is the creation operator, and c is the annihilation operator. Further,

$$\Theta(z) = \begin{cases} 1, & \text{if } z > 0 \\ 0, & \text{if } z \leq 0 \end{cases}.$$

To keep the calculations simple, simulation times short and get a basic understanding of the AS junction, a metallic interface is assumed, meaning that interface effects are omitted from the

calculations. See Chapter 6 for information about how these effects can be included. Because many superconductors are antiferromagnets at temperatures greater than the critical temperature, it is possible to build up an AS junction with an antiferromagnet and superconductor with similar lattice structures. With similar lattice structures it will be easier to make a junction with a low scalar barrier, and hence the calculations in this thesis should give a realistic picture of how an actual device operates. Next, rewrite equation 5.2, setting $\Delta^\dagger = \Delta$ and recognizing that an antiferromagnet has 2 neighbouring sublattice sites, A and B,

$$\begin{aligned}\mathcal{H}_{AS} =& -t_h \sum_{i,\delta,\sigma}(A^\dagger_{i,\sigma}B_{i+\delta,\sigma} + B^\dagger_{i+\delta,\sigma}A_{i,\sigma}) - \mu\sum_{i,\delta,\sigma}(A^\dagger_{i,\sigma}A_{i,\sigma} + B^\dagger_{i+\delta,\sigma}B_{i+\delta,\sigma})\Theta(z) \\ &- \mu_{sc}\sum_{i,\delta,\sigma}(A^\dagger_{i,\sigma}A_{i,\sigma} + B^\dagger_{i+\delta,\sigma}B_{i+\delta,\sigma})\Theta(-z) + J\sum_{i,\delta,\sigma}(M^z_A A^\dagger_{i,\sigma}A_{i,\sigma} + M^z_B B^\dagger_{i+\delta,\sigma}B_{i+\delta,\sigma})\Theta(z) \\ &+ \Delta\sum_{i,\delta,\sigma}\sigma(A^\dagger_{i,\sigma}A^\dagger_{i,-\sigma} + B^\dagger_{i+\delta,\sigma}B^\dagger_{i+\delta,-\sigma} + A_{i,\sigma}A_{i,-\sigma} + B_{i+\delta,\sigma}B_{i+\delta,-\sigma})\Theta(-z),\end{aligned} \tag{5.3}$$

where the creation and annihilation operators are replaced with sublattice sites A and B. Now, use $m^z = \frac{M^z_A + M^z_B}{2}$ and $n^z = \frac{M^z_A - M^z_B}{2}$, which makes $M^z_A = m^z + n^z$ and $M^z_B = m^z - n^z$. Further, assume that $m^z = 0$ and $n^z = 1$, which makes $M^z_A = 1$ and $M^z_B = -1$. This is effectively saying that electrons in neighbouring sublattice sites is required to have opposite spin, a principle that is already familiar from Subsection 2.3.2. Next the Fourier transforms are given by,

$$A_{i,\sigma} = \sum_{\boldsymbol{k}} A_{\boldsymbol{k}\sigma}e^{i\boldsymbol{k}\cdot\boldsymbol{r}_i}, \text{ and} \tag{5.4}$$

$$B_{i+\delta,\sigma} = \sum_{\boldsymbol{k}} B_{\boldsymbol{k}\sigma}e^{i\boldsymbol{k}\cdot(\boldsymbol{r}_i+\boldsymbol{\delta})}. \tag{5.5}$$

Now, insert equation 5.4 and 5.5 into the Hamiltonian,

$$\begin{aligned}\mathcal{H}_{AS} =& -t_h \sum_{i,\delta,\sigma}\sum_{\boldsymbol{k},\boldsymbol{k}'}(A^\dagger_{\boldsymbol{k},\sigma}B_{\boldsymbol{k}',\sigma}e^{-i\boldsymbol{k}\cdot\boldsymbol{r}_i}e^{i\boldsymbol{k}'\cdot(\boldsymbol{r}_i+\boldsymbol{\delta})} + B^\dagger_{\boldsymbol{k},\sigma}A_{\boldsymbol{k}',\sigma}e^{-i\boldsymbol{k}\cdot(\boldsymbol{r}_i+\boldsymbol{\delta})}e^{i\boldsymbol{k}'\cdot\boldsymbol{r}_i}) \\ &- \mu\sum_{i,\delta,\sigma}\sum_{\boldsymbol{k},\boldsymbol{k}'}(A^\dagger_{\boldsymbol{k},\sigma}A_{\boldsymbol{k}',\sigma}e^{-i\boldsymbol{k}\cdot\boldsymbol{r}_i}e^{i\boldsymbol{k}'\cdot\boldsymbol{r}_i} + B^\dagger_{\boldsymbol{k},\sigma}B_{\boldsymbol{k}',\sigma}e^{-i\boldsymbol{k}\cdot(\boldsymbol{r}_i+\boldsymbol{\delta})}e^{i\boldsymbol{k}'\cdot(\boldsymbol{r}_i+\boldsymbol{\delta})})\Theta(z)\end{aligned}$$

$$
\begin{aligned}
&- \mu_{sc} \sum_{i,\delta,\sigma} \sum_{\boldsymbol{k},\boldsymbol{k'}} (A^{\dagger}_{\boldsymbol{k},\sigma} A_{\boldsymbol{k'},\sigma} e^{-i\boldsymbol{k}\cdot\boldsymbol{r}_i} e^{i\boldsymbol{k'}\cdot\boldsymbol{r}_i} + B^{\dagger}_{\boldsymbol{k},\sigma} B_{\boldsymbol{k'},\sigma} e^{-i\boldsymbol{k}\cdot(\boldsymbol{r}_i+\boldsymbol{\delta})} e^{i\boldsymbol{k'}\cdot(\boldsymbol{r}_i+\boldsymbol{\delta})}) \Theta(-z) \\
&+ J \sum_{i,\delta,\sigma} \sum_{\boldsymbol{k},\boldsymbol{k'}} (A^{\dagger}_{\boldsymbol{k},\sigma} A_{\boldsymbol{k'},\sigma} e^{-i\boldsymbol{k}\cdot\boldsymbol{r}_i} e^{i\boldsymbol{k'}\cdot\boldsymbol{r}_i} - B^{\dagger}_{\boldsymbol{k},\sigma} B_{\boldsymbol{k'},\sigma} e^{-i\boldsymbol{k}\cdot(\boldsymbol{r}_i+\boldsymbol{\delta})} e^{i\boldsymbol{k'}\cdot(\boldsymbol{r}_i+\boldsymbol{\delta})}) \Theta(z) \\
&+ \Delta \sum_{i,\delta,\sigma} \sum_{\boldsymbol{k},\boldsymbol{k'}} \sigma (A^{\dagger}_{\boldsymbol{k},\sigma} A^{\dagger}_{\boldsymbol{k'},-\sigma} e^{-i\boldsymbol{k}\cdot\boldsymbol{r}_i} e^{-i\boldsymbol{k'}\cdot\boldsymbol{r}_i} + B^{\dagger}_{\boldsymbol{k},\sigma} B^{\dagger}_{\boldsymbol{k'},-\sigma} e^{-i\boldsymbol{k}\cdot(\boldsymbol{r}_i+\boldsymbol{\delta})} e^{-i\boldsymbol{k'}\cdot(\boldsymbol{r}_i+\boldsymbol{\delta})} \\
&+ A_{\boldsymbol{k},\sigma} A_{\boldsymbol{k'},-\sigma} e^{i\boldsymbol{k}\cdot\boldsymbol{r}_i} e^{i\boldsymbol{k'}\cdot\boldsymbol{r}_i} + B_{\boldsymbol{k},\sigma} B_{\boldsymbol{k'},-\sigma} e^{i\boldsymbol{k}\cdot(\boldsymbol{r}_i+\boldsymbol{\delta})} e^{i\boldsymbol{k'}\cdot(\boldsymbol{r}_i+\boldsymbol{\delta})}) \Theta(-z).
\end{aligned} \tag{5.6}
$$

By doing algebra, the Hamiltonian becomes,

$$
\begin{aligned}
\mathcal{H}_{AS} = &- t_h \sum_{i,\delta,\sigma} \sum_{\boldsymbol{k},\boldsymbol{k'}} (A^{\dagger}_{\boldsymbol{k},\sigma} B_{\boldsymbol{k'},\sigma} e^{i\boldsymbol{r}_i\cdot(\boldsymbol{k'}-\boldsymbol{k})} e^{i\boldsymbol{k'}\cdot\boldsymbol{\delta}} + B^{\dagger}_{\boldsymbol{k},\sigma} A_{\boldsymbol{k'},\sigma} e^{i\boldsymbol{r}_i\cdot(\boldsymbol{k'}-\boldsymbol{k})} e^{-i\boldsymbol{k}\cdot\boldsymbol{\delta}}) \\
&- \mu \sum_{i,\delta,\sigma} \sum_{\boldsymbol{k},\boldsymbol{k'}} (A^{\dagger}_{\boldsymbol{k},\sigma} A_{\boldsymbol{k'},\sigma} e^{i\boldsymbol{r}_i\cdot(\boldsymbol{k'}-\boldsymbol{k})} + B^{\dagger}_{\boldsymbol{k},\sigma} B_{\boldsymbol{k'},\sigma} e^{i\boldsymbol{r}_i\cdot(\boldsymbol{k'}-\boldsymbol{k})} e^{i\boldsymbol{\delta}\cdot(\boldsymbol{k'}-\boldsymbol{k})}) \Theta(z) \\
&- \mu_{sc} \sum_{i,\delta,\sigma} \sum_{\boldsymbol{k},\boldsymbol{k'}} (A^{\dagger}_{\boldsymbol{k},\sigma} A_{\boldsymbol{k'},\sigma} e^{i\boldsymbol{r}_i\cdot(\boldsymbol{k'}-\boldsymbol{k})} + B^{\dagger}_{\boldsymbol{k},\sigma} B_{\boldsymbol{k'},\sigma} e^{i\boldsymbol{r}_i\cdot(\boldsymbol{k'}-\boldsymbol{k})} e^{i\boldsymbol{\delta}\cdot(\boldsymbol{k'}-\boldsymbol{k})}) \Theta(-z) \\
&+ J \sum_{i,\delta,\sigma} \sum_{\boldsymbol{k},\boldsymbol{k'}} (A^{\dagger}_{\boldsymbol{k},\sigma} A_{\boldsymbol{k'},\sigma} e^{i\boldsymbol{r}_i\cdot(\boldsymbol{k'}-\boldsymbol{k})} - B^{\dagger}_{\boldsymbol{k},\sigma} B_{\boldsymbol{k'},\sigma} e^{i\boldsymbol{r}_i\cdot(\boldsymbol{k'}-\boldsymbol{k})} e^{i\boldsymbol{\delta}\cdot(\boldsymbol{k'}-\boldsymbol{k})}) \Theta(z) \\
&+ \Delta \sum_{i,\delta,\sigma} \sum_{\boldsymbol{k},\boldsymbol{k'}} \sigma (A^{\dagger}_{\boldsymbol{k},\sigma} A^{\dagger}_{\boldsymbol{k'},-\sigma} e^{i\boldsymbol{r}_i\cdot(-\boldsymbol{k'}-\boldsymbol{k})} + B^{\dagger}_{\boldsymbol{k},\sigma} B^{\dagger}_{\boldsymbol{k'},-\sigma} e^{i\boldsymbol{r}_i\cdot(-\boldsymbol{k'}-\boldsymbol{k})} e^{i\boldsymbol{\delta}\cdot(-\boldsymbol{k'}-\boldsymbol{k})} \\
&+ A_{\boldsymbol{k},\sigma} A_{\boldsymbol{k'},-\sigma} e^{i\boldsymbol{r}_i\cdot(\boldsymbol{k'}+\boldsymbol{k})} + B_{\boldsymbol{k},\sigma} B_{\boldsymbol{k'},-\sigma} e^{i\boldsymbol{r}_i\cdot(\boldsymbol{k'}+\boldsymbol{k})} e^{i\boldsymbol{\delta}\cdot(\boldsymbol{k'}+\boldsymbol{k})}) \Theta(-z).
\end{aligned} \tag{5.7}
$$

Now, utilize the mathematical equality,

$$
\sum_i e^{i\boldsymbol{r_i}\cdot(\boldsymbol{k'}-\boldsymbol{k})} = \delta(\boldsymbol{k'}-\boldsymbol{k}), \tag{5.8}
$$

to progress with the derivation of the total Hamiltonian for the antiferro-superconductor hybrid junction. Using equation 5.8, the Hamiltonian is given by,

$$\begin{aligned}\mathcal{H}_{AS} = &- t_h \sum_{\delta}\sum_{\boldsymbol{k},\sigma}(A^{\dagger}_{\boldsymbol{k},\sigma}B_{\boldsymbol{k},\sigma}e^{i\boldsymbol{k}\cdot\boldsymbol{\delta}} + B^{\dagger}_{\boldsymbol{k},\sigma}A_{\boldsymbol{k},\sigma}e^{-i\boldsymbol{k}\cdot\boldsymbol{\delta}}) - \mu\sum_{\boldsymbol{k},\sigma}(A^{\dagger}_{\boldsymbol{k},\sigma}A_{\boldsymbol{k},\sigma} + B^{\dagger}_{\boldsymbol{k},\sigma}B_{\boldsymbol{k},\sigma})\Theta(z) \\ &- \mu_{sc}\sum_{\boldsymbol{k},\sigma}(A^{\dagger}_{\boldsymbol{k},\sigma}A_{\boldsymbol{k},\sigma} + B^{\dagger}_{\boldsymbol{k},\sigma}B_{\boldsymbol{k},\sigma})\Theta(-z) + J\sum_{\boldsymbol{k},\sigma}(A^{\dagger}_{\boldsymbol{k},\sigma}A_{\boldsymbol{k},\sigma} - B^{\dagger}_{\boldsymbol{k},\sigma}B_{\boldsymbol{k},\sigma})\Theta(z) \\ &+ \Delta\sum_{\boldsymbol{k},\sigma}\sigma(A^{\dagger}_{\boldsymbol{k},\sigma}A^{\dagger}_{-\boldsymbol{k},-\sigma} + B^{\dagger}_{\boldsymbol{k},\sigma}B^{\dagger}_{-\boldsymbol{k},-\sigma} + A_{\boldsymbol{k},\sigma}A_{-\boldsymbol{k},-\sigma} + B_{\boldsymbol{k},\sigma}B_{-\boldsymbol{k},-\sigma})\Theta(-z).\end{aligned} \tag{5.9}$$

Using equation 4.8, the total Hamiltonian is given by,

$$\begin{aligned}\mathcal{H}_{AS} = &\sum_{\boldsymbol{k},\sigma}\gamma_{\boldsymbol{k}}A^{\dagger}_{\boldsymbol{k},\sigma}B_{\boldsymbol{k},\sigma} + \gamma_{-\boldsymbol{k}}B^{\dagger}_{\boldsymbol{k},\sigma}A_{\boldsymbol{k},\sigma} - \mu\sum_{\boldsymbol{k},\sigma}(A^{\dagger}_{\boldsymbol{k},\sigma}A_{\boldsymbol{k},\sigma} + B^{\dagger}_{\boldsymbol{k},\sigma}B_{\boldsymbol{k},\sigma})\Theta(z) \\ &- \mu_{sc}\sum_{\boldsymbol{k},\sigma}(A^{\dagger}_{\boldsymbol{k},\sigma}A_{\boldsymbol{k},\sigma} + B^{\dagger}_{\boldsymbol{k},\sigma}B_{\boldsymbol{k},\sigma})\Theta(-z) + J\sum_{\boldsymbol{k},\sigma}(A^{\dagger}_{\boldsymbol{k},\sigma}A_{\boldsymbol{k},\sigma} - B^{\dagger}_{\boldsymbol{k},\sigma}B_{\boldsymbol{k},\sigma})\Theta(z) \\ &+ \Delta\sum_{\boldsymbol{k},\sigma}(\sigma A^{\dagger}_{\boldsymbol{k},\sigma}A^{\dagger}_{-\boldsymbol{k},-\sigma} + \sigma B^{\dagger}_{\boldsymbol{k},\sigma}B^{\dagger}_{-\boldsymbol{k},-\sigma} + \sigma A_{\boldsymbol{k},\sigma}A_{-\boldsymbol{k},-\sigma} + \sigma B_{\boldsymbol{k},\sigma}B_{-\boldsymbol{k},-\sigma})\Theta(-z).\end{aligned} \tag{5.10}$$

For the upcoming calculations, the following basis is used,

$$\boldsymbol{\chi}_{AS_{8\times1}} = \begin{bmatrix} A^{\dagger}_{\boldsymbol{k},\sigma} \\ B^{\dagger}_{\boldsymbol{k},\sigma} \\ A_{-\boldsymbol{k},-\sigma} \\ B_{-\boldsymbol{k},-\sigma} \\ A^{\dagger}_{\boldsymbol{k},-\sigma} \\ B^{\dagger}_{\boldsymbol{k},-\sigma} \\ A_{-\boldsymbol{k},\sigma} \\ B_{-\boldsymbol{k},\sigma} \end{bmatrix}. \tag{5.11}$$

Rewriting, using the anticommutation relations and $\gamma_{\boldsymbol{k}} = \gamma_{-\boldsymbol{k}}$, the Hamiltonian is given by,

$$\begin{aligned}
\mathcal{H}_{AS} = \gamma_{\boldsymbol{k}}(&A^{\dagger}_{\boldsymbol{k},\sigma}B_{\boldsymbol{k},\sigma} + B^{\dagger}_{\boldsymbol{k},\sigma}A_{\boldsymbol{k},\sigma} - B_{-\boldsymbol{k},\sigma}A^{\dagger}_{-\boldsymbol{k},\sigma} - A_{-\boldsymbol{k},\sigma}B^{\dagger}_{-\boldsymbol{k},\sigma} + A^{\dagger}_{\boldsymbol{k},-\sigma}B_{\boldsymbol{k},-\sigma} \\
&+ B^{\dagger}_{\boldsymbol{k},-\sigma}A_{\boldsymbol{k},-\sigma} - B_{-\boldsymbol{k},-\sigma}A^{\dagger}_{-\boldsymbol{k},-\sigma} - A_{-\boldsymbol{k},-\sigma}B^{\dagger}_{-\boldsymbol{k},-\sigma}) - \mu(A^{\dagger}_{\boldsymbol{k},\sigma}A_{\boldsymbol{k},\sigma} + B^{\dagger}_{\boldsymbol{k},\sigma}B_{\boldsymbol{k},\sigma} \\
&- A_{-\boldsymbol{k},\sigma}A^{\dagger}_{-\boldsymbol{k},\sigma} - B_{-\boldsymbol{k},\sigma}B^{\dagger}_{-\boldsymbol{k},\sigma} + A^{\dagger}_{\boldsymbol{k},-\sigma}A_{\boldsymbol{k},-\sigma} + B^{\dagger}_{\boldsymbol{k},-\sigma}B_{\boldsymbol{k},-\sigma} - A_{-\boldsymbol{k},-\sigma}A^{\dagger}_{-\boldsymbol{k},-\sigma} \\
&- B_{-\boldsymbol{k},-\sigma}B^{\dagger}_{-\boldsymbol{k},-\sigma})\Theta(z) - \mu_{sc}(A^{\dagger}_{\boldsymbol{k},\sigma}A_{\boldsymbol{k},\sigma} + B^{\dagger}_{\boldsymbol{k},\sigma}B_{\boldsymbol{k},\sigma} - A_{-\boldsymbol{k},\sigma}A^{\dagger}_{-\boldsymbol{k},\sigma} - B_{-\boldsymbol{k},\sigma}B^{\dagger}_{-\boldsymbol{k},\sigma} \\
&+ A^{\dagger}_{\boldsymbol{k},-\sigma}A_{\boldsymbol{k},-\sigma} + B^{\dagger}_{\boldsymbol{k},-\sigma}B_{\boldsymbol{k},-\sigma} - A_{-\boldsymbol{k},-\sigma}A^{\dagger}_{-\boldsymbol{k},-\sigma} - B_{-\boldsymbol{k},-\sigma}B^{\dagger}_{-\boldsymbol{k},-\sigma})\Theta(-z) \\
&+ J(A^{\dagger}_{\boldsymbol{k},\sigma}A_{\boldsymbol{k},\sigma} - B^{\dagger}_{\boldsymbol{k},\sigma}B_{\boldsymbol{k},\sigma} - A_{-\boldsymbol{k},\sigma}A^{\dagger}_{-\boldsymbol{k},\sigma} + B_{-\boldsymbol{k},\sigma}B^{\dagger}_{-\boldsymbol{k},\sigma} + A^{\dagger}_{\boldsymbol{k},-\sigma}A_{\boldsymbol{k},-\sigma} \\
&- B^{\dagger}_{\boldsymbol{k},-\sigma}B_{\boldsymbol{k},-\sigma} - A_{-\boldsymbol{k},-\sigma}A^{\dagger}_{-\boldsymbol{k},-\sigma} + B_{-\boldsymbol{k},-\sigma}B^{\dagger}_{-\boldsymbol{k},-\sigma})\Theta(z) + \Delta(A^{\dagger}_{\boldsymbol{k},\sigma}A^{\dagger}_{-\boldsymbol{k},-\sigma} \\
&+ B^{\dagger}_{\boldsymbol{k},\sigma}B^{\dagger}_{-\boldsymbol{k},-\sigma} + A_{-\boldsymbol{k},-\sigma}A_{\boldsymbol{k},\sigma} + B_{-\boldsymbol{k},-\sigma}B_{\boldsymbol{k},\sigma} - A^{\dagger}_{\boldsymbol{k},-\sigma}A^{\dagger}_{-\boldsymbol{k},\sigma} - B^{\dagger}_{\boldsymbol{k},-\sigma}B^{\dagger}_{-\boldsymbol{k},\sigma} \\
&- A_{-\boldsymbol{k},\sigma}A_{\boldsymbol{k},-\sigma} - B_{-\boldsymbol{k},\sigma}B_{\boldsymbol{k},-\sigma})\Theta(-z).
\end{aligned} \tag{5.12}$$

The total Hamiltonian is now written in matrix form, setting $\mu_{-}^{+J} = -\mu\Theta(z) - \mu_{sc}\Theta(-z) + J\Theta(z)$, $\mu_{+}^{+J} = \mu\Theta(z) + \mu_{sc}\Theta(-z) + J\Theta(z)$, $\mu_{-}^{-J} = -\mu\Theta(z) - \mu_{sc}\Theta(-z) - J\Theta(z)$, and $\mu_{+}^{-J} = \mu\Theta(z) + \mu_{sc}\Theta(-z) - J\Theta(z)$,

$$\mathcal{H}_m = \begin{bmatrix}
\mu_{-}^{+J} & \gamma_{\boldsymbol{k}} & \Delta\Theta(-z) & 0 & 0 & 0 & 0 & 0 \\
\gamma_{\boldsymbol{k}} & \mu_{-}^{-J} & 0 & \Delta\Theta(-z) & 0 & 0 & 0 & 0 \\
\Delta\Theta(-z) & 0 & \mu_{+}^{-J} & -\gamma_{\boldsymbol{k}} & 0 & 0 & 0 & 0 \\
0 & \Delta\Theta(-z) & -\gamma_{\boldsymbol{k}} & \mu_{+}^{+J} & 0 & 0 & 0 & 0 \\
0 & 0 & 0 & 0 & \mu_{-}^{+J} & \gamma_{\boldsymbol{k}} & -\Delta\Theta(-z) & 0 \\
0 & 0 & 0 & 0 & \gamma_{\boldsymbol{k}} & \mu_{-}^{-J} & 0 & -\Delta\Theta(-z) \\
0 & 0 & 0 & 0 & -\Delta\Theta(-z) & 0 & \mu_{+}^{-J} & -\gamma_{\boldsymbol{k}} \\
0 & 0 & 0 & 0 & 0 & -\Delta\Theta(-z) & -\gamma_{\boldsymbol{k}} & \mu_{+}^{+J}
\end{bmatrix}, \tag{5.13}$$

where $\mathcal{H}_{AS} = \boldsymbol{\chi}_{AS_{8\times1}}\mathcal{H}_m\boldsymbol{\chi}^{\dagger}_{AS_{8\times1}}$.

5.4 Blonder-Tinkham-Klapwijk Formalism

Assuming the scattering mechanisms described in Section 5.2, BTK looks at the effects of AR, NR, TE, and TH as electrons from $z \gg 0$ is sent into the hybrid junction. The calculations are started using a modified BTK formalism and the basis from equation 5.11. Looking at equation 5.13, it can be seen that the Hamiltonian is block-diagonal,

$$\mathcal{H}_m = \begin{bmatrix} \mathcal{H}_{\boldsymbol{k},\sigma} & 0 \\ 0 & \mathcal{H}_{\boldsymbol{k},-\sigma}, \end{bmatrix} \tag{5.14}$$

where,

$$\mathcal{H}_{\boldsymbol{k},\sigma} = \begin{bmatrix} \mu_-^{+J} & \gamma_{\boldsymbol{k}} & \sigma\Delta\Theta(-z) & 0 \\ \gamma_{\boldsymbol{k}} & \mu_-^{-J} & 0 & \sigma\Delta\Theta(-z) \\ \sigma\Delta\Theta(-z) & 0 & \mu_+^{-J} & -\gamma_{\boldsymbol{k}} \\ 0 & \sigma\Delta\Theta(-z) & -\gamma_{\boldsymbol{k}} & \mu_+^{+J} \end{bmatrix}. \tag{5.15}$$

Here the basis is,

$$\boldsymbol{\chi}_{AS} = \begin{bmatrix} A^\dagger_{\boldsymbol{k},\sigma} \\ B^\dagger_{\boldsymbol{k},\sigma} \\ A_{-\boldsymbol{k},-\sigma} \\ B_{-\boldsymbol{k},-\sigma} \end{bmatrix}. \tag{5.16}$$

Because the Hamiltonian is block diagonal, one block will store all the information needed to figure out the probabilities for the different reflection and scattering mechanisms.

5.4.1 Antiferromagnet

In the antiferromagnet, $z > 0$. Inserting this in equation 5.15 the Hamiltonian for the antiferromagnet is given by,

$$\begin{bmatrix} J-\mu & \gamma_{\boldsymbol{k}} & 0 & 0 \\ \gamma_{\boldsymbol{k}} & -J-\mu & 0 & 0 \\ o & 0 & -J+\mu & -\gamma_{\boldsymbol{k}} \\ 0 & 0 & -\gamma_{\boldsymbol{k}} & J+\mu \end{bmatrix} \Psi_{AFM}(\boldsymbol{r}) = E\Psi_{AFM}(\boldsymbol{r}), \tag{5.17}$$

where $\Psi_{AFM}(\boldsymbol{r})$ is a linear combination of probability amplitudes, plane waves and the eigenvectors of the Hamiltonian. By taking the eigenvalues of equation 5.17, using the *Eigenvalues* function in Mathematica, the following is obtained,

$$E^{,\iota}_{\boldsymbol{k}} = \zeta\sqrt{\gamma_k^2 + J^2} + \iota\mu, \tag{5.18}$$

where $\zeta = \pm 1$ and $\iota = \pm 1$. The eigenvalues for $= 1$ and $\iota = 1$ are displayed in Figure 5.3.

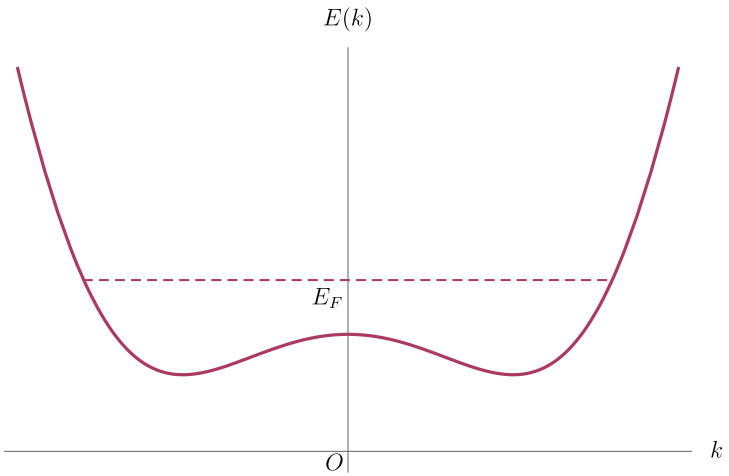

Figure 5.3: The eigenvalues for the antiferromagnetic region in the AS junction with $\zeta = 1$ and $\iota = 1$. Here, E_F denotes the Fermi energy and O is the origin.

Now, $\gamma_{\boldsymbol{k}} = a^2t(k_\parallel^2 + k_z^2 - k_0^2)$ is used to rewrite the eigenvalues, giving the wave vector in the antiferromagnet,

$$k_z^{\eta,\iota} = \sqrt{k_0^2 - k_\parallel^2 + \frac{\eta\sqrt{(E-\iota\mu)^2 - J^2}}{a^2t}}, \tag{5.19}$$

where $\eta = 1$ for electrons and $\eta = -1$ for holes. Here, k_0 can not be omitted because the γ_k terms does not appear on the diagonal in the Hamiltonian, hence k_0 does not simply represent a shift in energy. Using the *Eigenvectors* function in Mathematica and normalizing by $\frac{1}{\sqrt{2}}$, the eigenvectors $\chi_{AFM}^{\eta,\zeta,\iota}$ of the matrix in equation 5.17 are,

$$\chi_{AFM}^{e,1,-1} = \frac{1}{\sqrt{2}}\begin{bmatrix} \frac{J+\sqrt{J^2+\gamma_{\boldsymbol{k}}^2}}{\gamma_{\boldsymbol{k}}} \\ 1 \\ 0 \\ 0 \end{bmatrix}, \qquad \chi_{AFM}^{e,-1,-1} = \frac{1}{\sqrt{2}}\begin{bmatrix} \frac{J-\sqrt{J^2+\gamma_{\boldsymbol{k}}^2}}{\gamma_{\boldsymbol{k}}} \\ 1 \\ 0 \\ 0 \end{bmatrix},$$

$$\chi_{AFM}^{h,1,1} = \frac{1}{\sqrt{2}}\begin{bmatrix} 0 \\ 0 \\ \frac{J-\sqrt{J^2+\gamma_{\boldsymbol{k}}^2}}{\gamma_{\boldsymbol{k}}} \\ 1 \end{bmatrix}, \text{ and} \qquad \chi_{AFM}^{h,-1,1} = \frac{1}{\sqrt{2}}\begin{bmatrix} 0 \\ 0 \\ \frac{J+\sqrt{J^2+\gamma_{\boldsymbol{k}}^2}}{\gamma_{\boldsymbol{k}}} \\ 1 \end{bmatrix}.$$

With the eigenvectors at hand, the wave function inside the antiferromagnet can be found,

$$\begin{aligned}\Psi_{z,AFM}(z) = \frac{1}{\sqrt{k_z^{e,-1}}}e^{ik_z^{e,-1}z}\chi_{AFM}^{e,1,-1} + r_{e,1,-1}e^{-ik_z^{e,-1}z}\chi_{AFM}^{e,-1,1} + r_{e,-1,-1}e^{-ik_z^{e,-1}z}\chi_{AFM}^{e,-1,-1} \\ + r_{h,1,1}e^{-ik_z^{h,1}z}\chi_{AFM}^{h,1,1} + r_{h,-1,1}e^{-ik_z^{h,1}z}\chi_{AFM}^{h,-1,1}\end{aligned} \tag{5.20}$$

In the xy plane, the wave vector is conserved. This is because the incoming electrons are sent

with velocity only in the $\hat{z}$-direction. The final position-dependent antiferromagnet wave function is then given by,

$$\Psi_{AFM}(\boldsymbol{r}) = \Psi_{z,AFM}(z)e^{i(k_x x + k_y y)}. \tag{5.21}$$

5.4.2 Superconductor

In the superconductor $z < 0$. Inserting this into equation 5.15, using $q = |\boldsymbol{q}|$ instead of k to distinguish from the antiferromagnetic case and rewrite as a wave equation one arrive at,

$$\begin{bmatrix} -\mu_{sc} & \gamma_q & \sigma\Delta & 0 \\ \gamma_q & -\mu_{sc} & 0 & \sigma\Delta \\ \sigma\Delta & 0 & \mu_{sc} & -\gamma_q \\ 0 & \sigma\Delta & -\gamma_q & \mu_{sc} \end{bmatrix} \Psi_S(\boldsymbol{r}) = E\Psi_S(\boldsymbol{r}), \tag{5.22}$$

where $\Psi_S(\boldsymbol{r})$ is linear combination of probability amplitudes, plane waves and the eigenvectors of the Hamiltonian. This is the exact same Hamiltonian as for the ferromagnetic case, with the exception in terms of the σ in front of the superconducting gap. Looking back at the derivations from equation 3.8 to equation 3.24 it can be understood that σ will not change the result of the calculations of the superconducting coherence factors, and they will therefore still be given by,

$$|u_q^\iota| = \sqrt{\frac{1}{2}\left(1 + \frac{\gamma_q - \iota\mu_{sc}}{E_q^{\upsilon,\iota}}\right)} \tag{5.23}$$

and

$$|v_q^\iota| = \sqrt{\frac{1}{2}\left(1 - \frac{\gamma_q - \iota\mu_{sc}}{E_q^{\upsilon,\iota}}\right)}, \tag{5.24}$$

where $\xi_q = \gamma_q - \iota\mu_{sc}$ and $\iota = \pm 1$. Here, the eigenvalues are given by,

$$E_q^{\upsilon,\iota} = \upsilon\sqrt{(\gamma_q - \iota\mu_{sc})^2 + \Delta_q^2}. \tag{5.25}$$

The eigenvalues are plotted in Figure 5.4, setting $\mu_{sc} = E_F$.

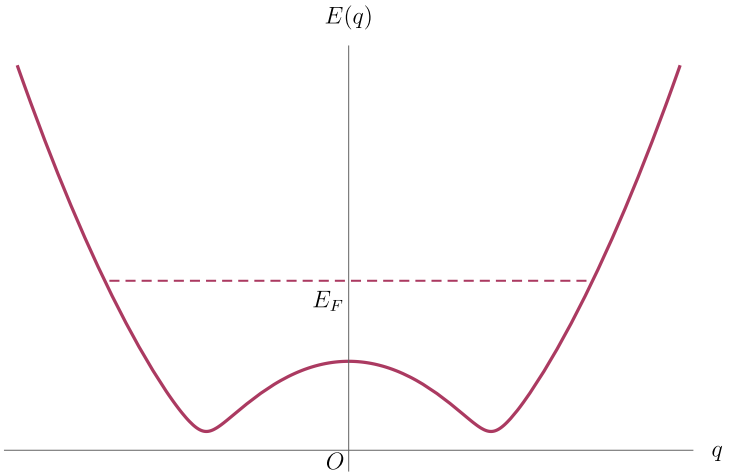

Figure 5.4: The eigenvalues for the superconducting region in the AS junction with $\upsilon = 1$ and $\iota = 1$. Here, E_F denotes the Fermi energy and O is the origin.

Rearranging the eigenvalues using $\gamma_q = a^2t(q_p^2 + q_z^2 - q_0^2)$ the wave vector can be written as,

$$q_z^{\eta,\iota} = \sqrt{q_0^2 - q_p^2 + \frac{\eta\sqrt{E^2 - \Delta^2} - \iota\mu_{sc}}{a^2t}}, \tag{5.26}$$

where $\eta = 1$ for electrons and $\eta = -1$ for holes. In the FS junction, the eigenvector for the superconductor in a normal metal-superconductor junction was given by equation 4.31. There will be two different options for the normal metal-superconductor eigenvectors χ_S^η,

$$\chi_S^e = \begin{bmatrix} u_q \\ \\ v_q \end{bmatrix} \text{ and } \chi_S^h = \begin{bmatrix} v_q \\ \\ u_q \end{bmatrix}. \tag{5.27}$$

To construct the eigenvectors for the superconductor in the antiferromagnet, first find the eigenvectors of the normal metal in a normal metal-superconductor hybrid junction. Looking back at equation 5.15 and inserting $z > 0$ and $J = 0$, the Hamiltonian for the normal metal is given by,

$$\mathcal{H}_{NM} = \begin{bmatrix} -\mu & \gamma_q & 0 & 0 \\ \gamma_q & -\mu & 0 & 0 \\ o & 0 & \mu & -\gamma_q \\ 0 & 0 & -\gamma_q & \mu \end{bmatrix}. \tag{5.28}$$

This is block diagonal, which means that only one of the blocks has to be investigated, and that block will then contain all the information in the matrix. The upper left quadrant is given by,

$$\mathcal{H}_{NM_B} = \begin{bmatrix} \iota\mu & \upsilon\gamma_q \\ \upsilon\gamma_q & \iota\mu \end{bmatrix}. \tag{5.29}$$

The eigenvectors χ^{υ}_{NM} of equation 5.29 is given by,

$$\chi^{1}_{NM} = \begin{bmatrix} -1 \\ 1 \end{bmatrix} \text{ and } \chi^{-1}_{NM} = \begin{bmatrix} 1 \\ 1 \end{bmatrix}. \tag{5.30}$$

Taking all this into account, four eigenvectors $\chi^{\eta,\upsilon,\iota}_{S}$ for the superconducting part of the junction is found,

$$\chi^{e,1,\iota}_{S} = \frac{1}{\sqrt{2}}\left[u^{\iota}_{q}, v^{\iota}_{q}\right] \otimes \begin{bmatrix} -1 \\ 1 \end{bmatrix} = \frac{1}{\sqrt{2}} \begin{bmatrix} -u^{\iota}_{q} \\ u^{\iota}_{q} \\ -v^{\iota}_{q} \\ v^{\iota}_{q} \end{bmatrix}, \qquad \chi^{e,-1,\iota}_{S} = \frac{1}{\sqrt{2}}\left[u^{\iota}_{q}, v^{\iota}_{q}\right] \otimes \begin{bmatrix} 1 \\ 1 \end{bmatrix} = \frac{1}{\sqrt{2}} \begin{bmatrix} u^{\iota}_{q} \\ u^{\iota}_{q} \\ v^{\iota}_{q} \\ v^{\iota}_{q} \end{bmatrix},$$

$$\chi_S^{h,1,\iota} = \frac{1}{\sqrt{2}}\left[v_q^\iota, u_q^\iota\right] \otimes \begin{bmatrix} -1 \\ \\ 1 \end{bmatrix} = \frac{1}{\sqrt{2}} \begin{bmatrix} -v_q^\iota \\ \\ v_q^\iota \\ \\ -u_q^\iota \\ \\ u_q^\iota \end{bmatrix}, \text{ and } \quad \chi_S^{h,-1,\iota} = \frac{1}{\sqrt{2}}\left[v_q^\iota, u_q^\iota\right] \otimes \begin{bmatrix} 1 \\ \\ 1 \end{bmatrix} = \frac{1}{\sqrt{2}} \begin{bmatrix} v_q^\iota \\ \\ v_q^\iota \\ \\ u_q^\iota \\ \\ u_q^\iota \end{bmatrix}.$$

The wave function will then be given by,

$$\begin{aligned} \Psi_{z,S}(z) = t_{e,1}e^{iq_z^{e,1,\iota}z}\chi_S^{e,1} + t_{e,-1}e^{iq_z^{e,1}z}\chi_S^{e,-1,\iota} + t_{h,1}e^{-iq_z^{h,1}z}\chi_S^{h,1,\iota} \\ + t_{h,-1}e^{-iq_z^{h,1}z}\chi_S^{h,-1,\iota}. \end{aligned} \tag{5.31}$$

In the xy plane, the wave vector is conserved. This is because incoming electrons are sent with velocity only in the $\hat{z}$-direction. Using this, the final wave function for the superconducting region is given by,

$$\Psi_S(\boldsymbol{r}) = \Psi_{z,S}(z)e^{i(k_x x + k_y y)}. \tag{5.32}$$

Combining equation 5.21 and 5.32 gives the final wave function for the entire material composition,

$$\Psi(\boldsymbol{r}) = \begin{cases} \Psi_{AFM}(\boldsymbol{r}) & \text{if } z \geq 0 \\ \Psi_S(\boldsymbol{r}) & \text{if } z < 0 \end{cases}.$$

5.4.3 Boundary Conditions

The wave functions in the antiferromagnet and superconductor has to be equal at the interface. This is the first boundary condition,

$$\Psi_{z,AFM}(0) = \Psi_{z,S}(0). \tag{5.33}$$

The second boundary condition is found by integrating equation 5.13 from $-b$ to b. In contrast to the FS case, interface effects are not included in the AS hybrid junction. Without interface effects, the second boundary condition will be given by,

$$\frac{\partial \Psi_{z,AFM}}{\partial z}|_{z=0^-} = \frac{\partial \Psi_{z,S}}{\partial z}|_{z=0^+}, \tag{5.34}$$

which is the famous equation for the second boundary condition of expressions that do not include a delta function. The entire derivation of the second boundary condition can be found in Appendix D.

Chapter 6

Further Research

There are still major areas to investigate related to thermoelectric properties of (anti)ferromagnet-superconductor hybrid junctions. Utilizing the boundary conditions in equation 5.33 and 5.34 and using the *NSolve* function in Mathematica one can solve the two equations to get the probability amplitudes. Then, combining these amplitudes with their respective wave vectors, the probabilities are given by,

$$R_{e(h),\sigma}(E, k_p) = \mathrm{Re}[k_z^{e(h),1}|r_{e(h),1}|^2 + k_z^{e(h),1}|r_{e(h),-1}|^2] \tag{6.1}$$

and

$$T_{e(h),\sigma}(E, k_p) = \mathrm{Re}[q_z^{e(h),1}|t_{e(h),1}|^2 + q_z^{e(h),1}|t_{e(h),-1}|^2]. \tag{6.2}$$

To proceed insert these probabilities into equation 4.42, 4.43 and 4.46 to get the final expressions for TC, SkC and FOM of the AS junction. In addition to knowing these material parameters, it will be interesting to investigate how AR is modified in the AS junction. This can be done by setting h in equation 6.1 and plotting the result against E and $k_\parallel$.

The analysis of the AS junction in this thesis has not included a scalar barrier or spin-orbit coupling at the interface. It will be difficult to design an AS junction in a laboratory without any scalar barrier at the interface at all, although many antiferromagnets and superconductors have a similar lattice structure. Further, the inclusion of spin-orbit coupling will render spin-flipping processes possible. Therefore, a complete discussion include these two phenomena in

addition to ones that are already included. The tight binding model describing Rashba and Dresselhaus spin-orbit coupling and scalar barrier is given by,

$$\mathcal{H}_{int} = \sum_{i,\sigma} \boldsymbol{\omega} \cdot \boldsymbol{\sigma} c^{\dagger}_{i,\sigma} c_{i,\sigma} + Vd \sum_{i,\sigma} c^{\dagger}_{i,\sigma} c_{i,\sigma}, \tag{6.3}$$

where $\boldsymbol{\omega} = \big[\lambda_R k_y + \lambda_D k_x, -\lambda_R k_x - \lambda_D k_y, 0\big]$. To include these interface effects, simply add equation 6.3 to equation 5.2 and continue the derivations. To add complexity, the Zeeman effect described in Subsection 2.4.3 could also be included.

With knowledge about the AR behavior, as well as TC, SkC and FOM, it should be possible to assess the thermoelectrical value of the AS junction on a satisfyingly broad basis. If the results are promising, it should, however, be noted that it takes a lot of energy to cool down present day's superconductors to the superconducting state. In order to commercialize heat-to-energy converters based on superconductors, it will therefore be necessary to invent stable room temperature superconductors.

Chapter 7

Conclusion

This master's thesis investigates the thermoelectrical properties of the (anti)ferromagnet-superconductor hybrid junction. The purpose of the thesis is to derive, plot and evaluate TC, SkC and FOM of the two hybrid junctions, in order to assess their value in thermoelectric devices. In the ferromagnet, the simultaneous inclusion of both Rashba and Dresselhaus spin-orbit coupling is of special interest as no one have investigated its effect on TC, SkC and FOM before. For the AS junction, the behavior of AR is still unknown, and insight into AR behavior, as well as TC, SkC and FOM of the junction serve as the main objective of the study.

The BTK formalism has been utilized in the research to find the wave functions for both the (anti)ferromagnet and superconductor regions. Using boundary conditions and the *NSolve* function in Mathematica, the probabilities for four different scattering processes were found; AR, NR, TE, and TH. These probabilities are then used in the expressions for TC, SkC and FOM.

The study shows that AR is reduced with the inclusion of polarization in the FS junction, thereby reducing TC. Further, TC increases with temperature, while the superconducting gap, and hence AR probability, is reduced. It is also shown that a higher scalar barrier gives higher NR probability. A good thermoelectric material is known for a high FOM, and for no spin-orbit coupling, a scalar barrier $Z = 4$, polarization $P = 0.9$, and normalized temperature $\frac{T}{T_{crit}} \approx 0.4$ the results showed that the FOM of the FS junction is approximately 5, a number that is a lot greater than what conventional thermoelectric devices has today. By including RSOI and DSOI, the results show that it is possible to achieve a FOM of 80, indicating that an intelligently designed FS junction can be a very good thermoelectric material.

For the AS junction the matrix Hamiltonian is found, together with the eigenvectors and wave function describing the particle behavior in the material. Although further research is needed to find the TC, SkC and FOM for the AS junction, the present findings will hopefully be of high value for further supplementary analysis of the AS junction.

Appendices

Appendix A

Variables and Constants

$\hbar$	Reduced Planck constant
m	Particle mass
V	Potential
$\Psi(\boldsymbol{r}, t)$	Wave function at position $\boldsymbol{r}$ and time t
E	Energy
c	Speed of light
$\boldsymbol{g}$	$\begin{bmatrix} 0 & \boldsymbol{\sigma} \\ \boldsymbol{\sigma} & 0 \end{bmatrix}$
$\boldsymbol{p}$	Momentum vector
e	Elementary charge
$\boldsymbol{A}_v$	Vector potential
h	$\begin{bmatrix} I & 0 \\ 0 & -I \end{bmatrix}$
m_e	Electron rest mass
$\boldsymbol{\sigma}$	Pauli spin matrix vector
ψ	Wave vector
n	Principal quantum number
l	Azimuthal quantum number
m_l	Magnetic quantum number
m_s	Spin quantum number
s	Spin
P	Polarization
$\chi_m(\boldsymbol{r})$	Unitless magnetic susceptibility
$M(\boldsymbol{r})$	Nonuniform magnetization amplitude at position $\boldsymbol{r}$
$B(\boldsymbol{r})$	Nonuniform magnetic field intensity at position $\boldsymbol{r}$

μ_0	Magnetic permeability in vacuum
$\mathcal{H}_H$	Heisenberg Hamiltonian
$S_{i/j}$	Spin operator
$J_{i,j}$	Exchange constant between electron i and j
$E_{\uparrow/\downarrow}(k)$	Dispersion relation for spin up/down electrons at k
$\zeta(k)$	Dispersion relation for spinless electrons at k
I	Stoner parameter
$\frac{N_{\uparrow/\downarrow}}{N}$	Density of spin up/down electrons
E_{pen}	Energy penalty
A_s	Exchange stiffness constant
dV	Incremental volume
T	Temperature
T_C	Curie temperature
$\mathcal{H}_{SO}$	Spin-orbit coupling Hamiltonian
$\boldsymbol{k}$	Wave vector
$\boldsymbol{E}_f$	Electric field
$\boldsymbol{S}$	Spin
$\boldsymbol{L}$	Angular momentum
$\mathcal{H}_R$	Rashba Hamiltonian
$k_{x/y/z}$	Wave vector in $\hat{x}/\hat{y}/\hat{z}$ direction
$\mathcal{H}_D$	Dresselhaus spin-orbit coupling Hamiltonians
$\mathcal{H}_Z$	Zeeman Hamiltonian
$\boldsymbol{\mu}_s$	$-\frac{e}{2m}\boldsymbol{S}$
$\boldsymbol{\mu}_l$	$-\frac{e}{2m}\boldsymbol{L}$
$\boldsymbol{B}_{ext}$	External magnetic field
μ_B	Bohr magneton $\frac{e\hbar}{2m}$
k_R	Shift in wave vector due to Rashba spin-orbit coupling
X_{ij}	Scattering matrix position row i, column j
W	Incoming wave amplitude from the right side of the barrier
U	Outgoing wave amplitude on the right side of the barrier
K	Incoming wave amplitude from the left side of the barrier
O	Outgoing wave amplitude on the left side of the barrier
$V(x)$	Potential barrier at point x
T_{crit}	Critical temperature
$\boldsymbol{B}$	Uniform magnetic flux density
$\boldsymbol{H}$	Uniform magnetic field strength
$\boldsymbol{M}$	Uniform magnetization
μ_m	Magnetic permeability
H_{crit}	Critical magnetic field
J_{crit}	Critical current density
V_{e-e}	Electron-electron interactions

V_{e-i}	Electron-ion interactions
$\Psi(\boldsymbol{r}_1, \boldsymbol{r}_2)$	Wave function of a two particle system
m_1	Mass of particle 1
m_2	Mass of particle 2
$\xi_{\boldsymbol{k}}$	Energy of electron with momentum $\boldsymbol{k}$
$c^\dagger_{\boldsymbol{k},\sigma}$	Creation operator
$c_{\boldsymbol{k},\sigma}$	Annihilation operator
N_p	Number of electrons
$V_{\boldsymbol{k},\boldsymbol{k'}}$	Coulomb interaction between two electrons
ω_{Dye}	Debye frequency
λ_{Dye}	Debye wavelength
V_0	Ground state potential
$\Delta_{\boldsymbol{k}}$	Superconducting gap
Δ_0	Ground state superconducting gap
Q	$c^\dagger_{\boldsymbol{k}\uparrow} c^\dagger_{-\boldsymbol{k}\downarrow}$
R	$c_{-\boldsymbol{k'}\downarrow} c_{\boldsymbol{k'}\uparrow}$
$f_{k\uparrow}$	Fermionic operator
$f_{-k\downarrow}$	Fermionic operator
$v_{\boldsymbol{k}}$	Complex coefficient
$u_{\boldsymbol{k}}$	Complex coefficient
$E_{\boldsymbol{k}}$	$\sqrt{\xi^2_{\boldsymbol{k}} + \lvert\Delta_{\boldsymbol{k}}\rvert^2}$
β	$\frac{1}{k_B T}$
$D(E_F)$	Density of states at the Fermi energy
μ	Chemical potential
$\boldsymbol{\tau}$	4×4 Pauli spin matrix vector
$\boldsymbol{h}$	Magnetic exchange field
$\mathcal{H}_e$	Electron Hamiltonian
$\mathcal{H}_h$	Hole Hamiltonian
$\mu(z)$	Chemical potential at z
Δ_{xc}	Exchange spin splitting
$\mathcal{H}_{int}$	Interfacial barrier
d	Width of scalar barrier
$\boldsymbol{\omega}$	Spin-orbit coupling field
λ_R	Rashba field strength
λ_D	Dresselhaus field strength
F	$\frac{\Delta_{xc}\Theta(z)}{2}$
$\Theta(z)$	Step function
σ	Spin
$r^{e/h}_{\pm\sigma}$	Reflection probability amplitude
$t^{e/h}_{\pm\sigma}$	Transmission probability amplitude
b	Integration limits for boundary conditions

$\boldsymbol{x}$	Probability amplitude vector
$q_{e/h}$	Superconductor wave vector
$R_{(e/h),\sigma}$	Normal/Andreev reflection
$T_{(e/h),\sigma}$	Tunneling as electron/hole like quasiparticles
ϵ	Normalized energy
k_p	Normalized parallel wave vector
κ	Thermal conductivity
k_p	Parallel wave vector
Z	Scalar barrier strength
SkC	Seebeck coefficient
TC	Thermal conductivity
FOM	Figure of merit
α	Thermoelectric coefficient
G	Electric conductance
k_B	Boltzmann constant
K	$\kappa - \frac{\alpha^2}{T_d G}$ and is expressed in units $\frac{k_B^2 T}{h}$
$\mathcal{H}_{AFM}$	Normalized antiferromagnet Hamiltonian
$\mathcal{H}_{SC}$	Normalized superconductor Hamiltonian
$\mathcal{H}_K$	Normalized kinetic energy Hamiltonian
t_h	Hopping energy
$\mathcal{H}_{sd}$	Interaction between the spins of the itinerant s electrons and localized d electrons Hamiltonian
$\mathcal{H}_\mu$	Antiferromagnet chemical potential Hamiltonian
$\mathcal{H}_\Delta$	Superconducting gap Hamiltonian
$\mathcal{H}_{\mu_{sc}}$	Superconductor chemical potential Hamiltonian
$\boldsymbol{M}_i$	$M_i^z \hat{z}$
J	Interaction between the spins of the itinerant s electrons and localized d electrons
A/B	Sublattice sites
$\gamma_{\boldsymbol{k}}$	Kinetic energy
a	Distance between lattice sites
δ	A step in the square lattice
Φ	Time reversal operator
k_0	Shift in wave vector
$\boldsymbol{N}$	Staggered order parameter
η	1 for electrons and -1 for holes

Appendix B

Ferromagnet-Superconductor Calculations

In this appendix, the matrix Hamiltonian for the FS junction is derived from the BdG equation instead of the tight binding model. As expected the final result for the matrix Hamiltonian is in agreement with the result achieved by using the tight binding model, see Section 4.3. The first few lines of the derivation can be found in Subchapter 4.4 together with an explanation of the variables. The BdG equation is still given by,

$$\begin{bmatrix} \mathcal{H}_e & \Delta_s \\ \Delta_s^\dagger & \mathcal{H}_h \end{bmatrix} \Psi(\boldsymbol{r}) = E\Psi(\boldsymbol{r}), \tag{B.1}$$

where $\mathcal{H}_e$ is given by,

$$\mathcal{H}_e = -\frac{\hbar^2}{2m}\sigma_0\nabla^2 - \mu(z)\sigma_0 - \frac{\Delta_{xc}}{2}\Theta(z)\boldsymbol{M}\cdot\boldsymbol{\sigma} + (Vd\sigma_0 + \boldsymbol{\omega}\cdot\boldsymbol{\sigma})\delta(z), \tag{B.2}$$

while the single-particle Hamiltonian for the holes is,

$$\mathcal{H}_h = -\sigma_y\mathcal{H}_e^*\sigma_y. \tag{B.3}$$

Now, calculate $\boldsymbol{M}\cdot\boldsymbol{\sigma}$ and $\boldsymbol{\omega}\cdot\boldsymbol{\sigma}$ to find $\mathcal{H}_e$,

$$\boldsymbol{M}\cdot\boldsymbol{\sigma} = \begin{bmatrix} 0 & \sin\theta\cos\phi \\ \sin\theta\cos\phi & 0 \end{bmatrix} + \begin{bmatrix} 0 & -i\sin\theta\sin\phi \\ i\sin\theta\sin\phi & 0 \end{bmatrix} + \begin{bmatrix} \cos\theta & 0 \\ 0 & -\cos\theta \end{bmatrix}$$

$$= \begin{bmatrix} \cos\theta & \sin\theta e^{-i\phi} \\ \sin\theta e^{i\phi} & -\cos\theta \end{bmatrix} \tag{B.4}$$

and

$$\boldsymbol{\omega}\cdot\boldsymbol{\sigma} = \begin{bmatrix} 0 & \lambda_R k_y + \lambda_D k_x \\ \lambda_R k_y + \lambda_D k_x & 0 \end{bmatrix} + \begin{bmatrix} 0 & i\lambda_R k_x + i\lambda_D k_y \\ -i\lambda_R k_x - i\lambda_D k_y & 0 \end{bmatrix}$$

$$= \begin{bmatrix} 0 & \lambda_R(k_y + ik_x) + \lambda_D(k_x + ik_y) \\ \lambda_R(k_y - ik_x) + \lambda_D(k_x - ik_y) & 0 \end{bmatrix}. \tag{B.5}$$

Adding these results to the remaining parts of the ferromagnetic electron Hamiltonian, an expression for $\mathcal{H}_e$ is found,

$$\mathcal{H}_e = \begin{bmatrix} Vd\gamma\mu_-^- + P_c & P_s^- + R_+^- L_+^+ \\ P_s^+ + R_-^+ L_+^- & Vd\gamma\mu_-^- - P_c \end{bmatrix}, \tag{B.6}$$

where $Vd\gamma\mu_-^- = \gamma_{\boldsymbol{k}} - \mu\Theta(z) - \mu_{sc}\Theta(-z) + Vd\delta(z)$, $P_s^- = -\frac{\Delta_{xc}}{2}\sin\theta e^{-i\phi}\Theta(z)$, $P_s^+ = -\frac{\Delta_s}{2}\sin\theta e^{i\phi}\Theta(z)$, $P_c = -\frac{\Delta_{xc}}{2}\cos\theta\Theta(z)$, $R_-^+ L_+^- = k_\parallel(-i\lambda_R e^{i\phi} + \lambda_D e^{-i\phi})\delta(z)$, and $R_+^- L_+^+ = k_\parallel(i\lambda_R e^{-i\phi} + \lambda_D e^{i\phi})\delta(z)$. Similarly, the hole Hamiltonian in the ferromagnet is given by,

$$\mathcal{H}_h = \begin{bmatrix} -Vd\gamma\mu_-^- - P_c & -P_s^- - R_+^- L_+^+ \\ -P_s^+ - R_-^+ L_+^- & -Vd\gamma\mu_-^- + P_c \end{bmatrix}. \tag{B.7}$$

Next, insert the electron and hole Hamiltonian into equation 4.17,

$$\mathcal{H}_m = \begin{bmatrix} Vd\gamma\mu_- + P_c & P_s^- + R_+^- L_+^+ & \Delta\Theta(-z) & 0 \\ P_s^+ + R_-^+ L_+^- & Vd\gamma\mu_- - P_c & 0 & \Delta\Theta(-z) \\ \Delta\Theta(-z) & 0 & -Vd\gamma\mu_- - P_c & -P_s^- - R_+^- L_+^+ \\ 0 & \Delta\Theta(-z) & -P_s^+ - R_-^+ L_+^- & -Vd\gamma\mu_- + P_c \end{bmatrix}. \tag{B.8}$$

Appendix C

Varying Dresselhaus Spin-Orbit Coupling Strengths

In this appendix, the TC, SkC and FOM is plotted for varying Dresselhaus spin-orbit coupling strengths to investigate the difference between Rashba and Dresselhaus spin-orbit coupling.

C.1 Thermal Conductivity

To see how a varying Dresselhaus spin-orbit coupling strength affects the TC, set $\lambda_R = 1$, $\theta = \frac{\pi}{2}$, $k_F = 1$, $\phi = 0$, and $\Delta = 1$.

From Figure C.1 it can be demonstrated that TC decreases for higher values of λ_D in the case of $Z = 0$. What will be achieved by increasing the amount of Dresselhaus spin-orbit coupling, is that there will more SOC in total, and hence more spin-flipping processes.

Next, by increasing the scalar barrier strength a reduction in TC will be observed. This is because an increase in Z will increase the probability for NR and thereby decrease the TC as described in equation 4.42. Further, at a given value for Z, the interplay between Z, P and λ_D makes the behavior for TC go from being decreasing in nature to being increasing in nature for higher ratios of DSOI over RSOI.

A higher polarization gives a reduction in AR due to minority spin subband. In addition there will be less tunneling corresponding to minority spin subband, giving a reduction in TC for

higher polarizations.

Next, observe that Figure C.1 looks exactly the same as Figure 4.9. Thinking back at what Rashba and Dresselhaus spin-orbit coupling does, it can be remembered that an increase in any of them will increase the probability for the spin flipping processes described in Subchapter 4.2. Based on what can be seen in the figures, it is safe to assume that a similar increase in $\frac{\lambda_D}{\lambda_R}$ and $\frac{\lambda_R}{\lambda_D}$ will affect the probabilities for NR and AR equally much.

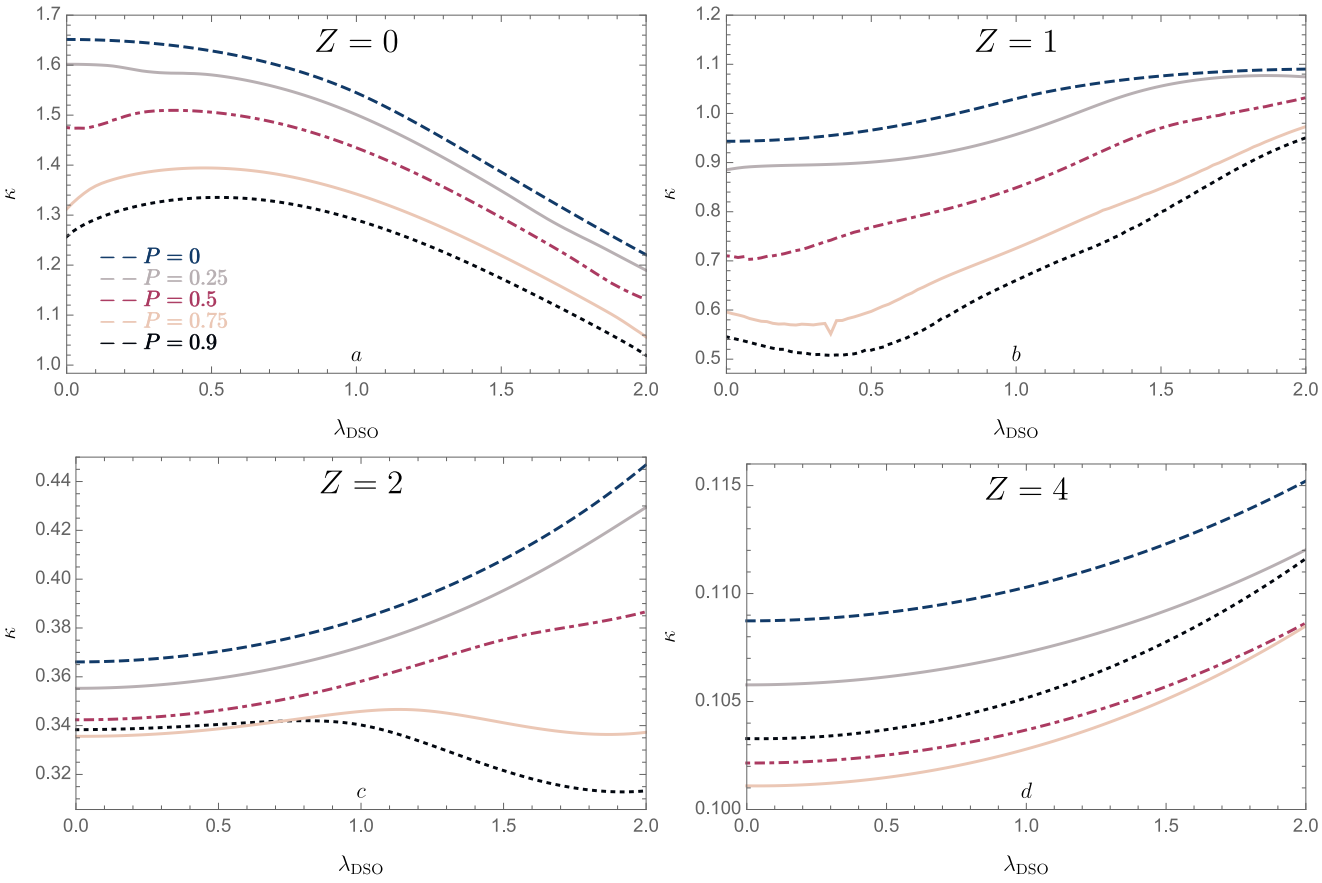

Figure C.1: The TC for varying scalar barrier strength, Dresselhaus spin-orbit coupling strength and polarization. Here, the Rashba spin-orbit coupling strength is $\lambda_R = 1$, the polar angle is $\theta = \frac{\pi}{2}$, the Fermi wave vector is $k_F = 1$, the azimuthal angle is $\phi = 0$, the superconducting gap is $\Delta = 1$, and the normalized temperature $T_d = 0.5$.

Although spin-orbit coupling increases the probability for the spin-flipping processes, it does not

change the total probability for AR or NR. Looking back at Equation 4.42, it can be understood that the TC should not differ if the DSOI or RSOI are increased equally much.

C.2 Seebeck Coefficient

To see how a varying Dresselhaus spin-orbit coupling strength affects the SkC, set $\lambda_R = 1$, $\theta = \frac{\pi}{2}$, $k_F = 1$, $\phi = 0$, and $\Delta = 1$.

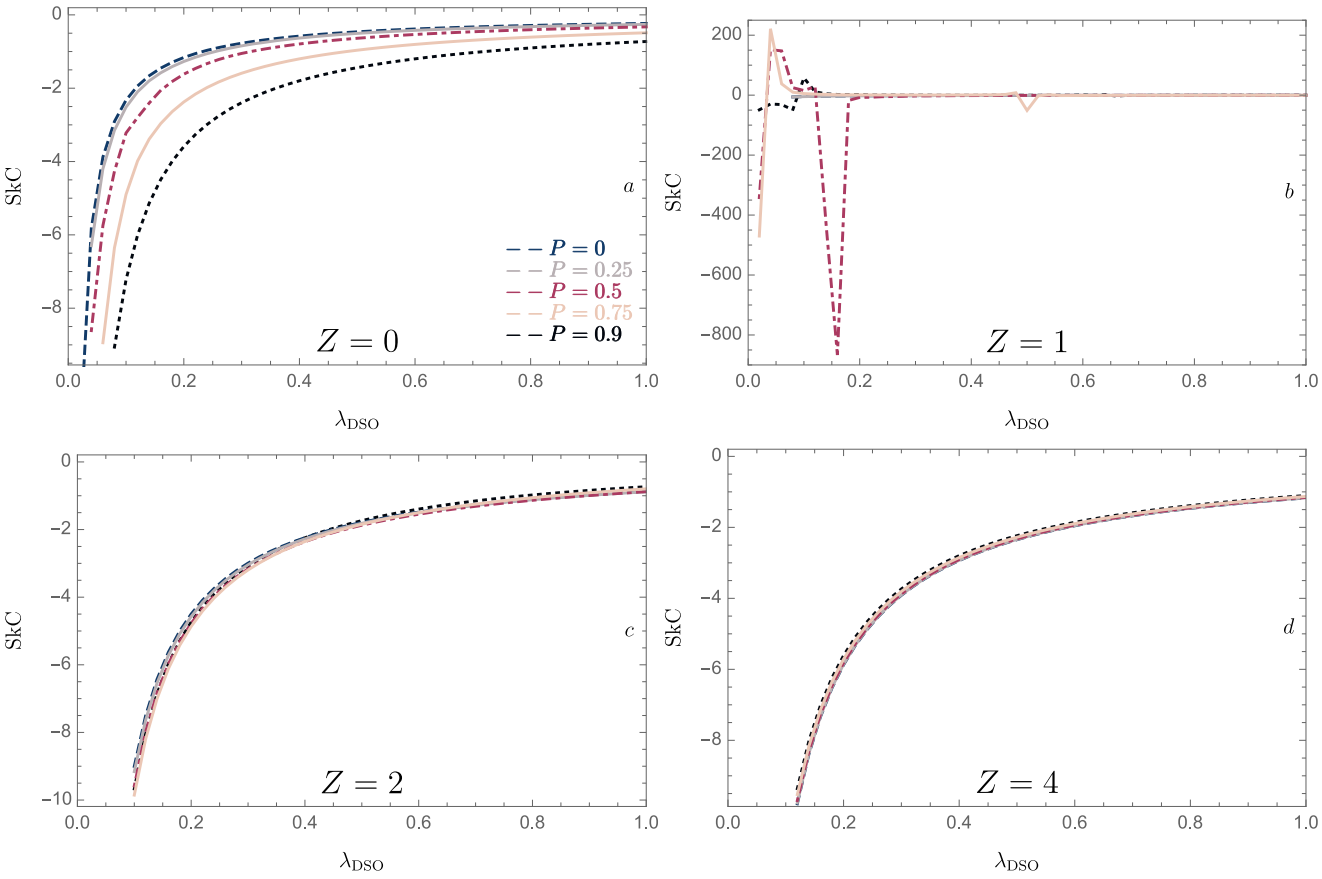

Figure C.2: The SkC for varying scalar barrier strengths, Dresselhaus spin-orbit coupling strengths and polarizations. Here, the Rashba spin-orbit coupling strength is $\lambda_R = 1$, the polar angle is $\theta = \frac{\pi}{2}$, the Fermi wave vector is $k_F = 1$, the azimuthal angle is $\phi = 0$, the superconducting gap is $\Delta = 1$, and the normalized temperature $T_d = 0.5$.

In Figure C.2 it might be seen that the SkC is negative for all values of λ_D in the case of even Z. For these values of Z, the SkC becomes more negative as lower values of λ_D are approached. Since a more negative SkC imply that a material is able to convert more heat to energy, a low value for Dresselhaus spin-orbit coupling is desirable in the production of a heat to energy converter. Looking back at Figure 4.11, for which the SkC is plotted for λ_R, one can understand that spin-orbit coupling in general seems to be unfavorable in cases where a highly negative SkC is desirable. This is also supported by the results from [21].

In the case of $Z = 0$, a stronger polarization makes SkC more negative, because of an increase in AR. This can be understood by looking into equation 4.43, 4.44 and 4.45. Here, it can be realized that a higher probability for AR increases the electric conductance, while at the same time decreasing the thermoelectric coefficient. This will make the SkC more negative. At $Z > 0$, NR will dominate and make the behavior of SkC more or less independent of polarization.

For $Z = 1$, SkC takes on a highly regular behavior, ranging from approximately -850 to 200 at low ratios for DSOI over RSOI, and then being 0 for higher ratios. Also in the case of the SkC, it seems like there is no difference if SkC is plotted against $\frac{\lambda_D}{\lambda_R}$ or $\frac{\lambda_R}{\lambda_D}$.

C.3 Figure of Merit

To see how a varying Dresselhaus spin-orbit coupling strength affects the FOM, set $\lambda_R = 1$, $\theta = \frac{\pi}{2}$, $k_F = 1$, $\phi = 0$, and $\Delta = 1$.

In Figure C.3 it is evident that FOM is almost 0 for most combinations of P, Z and λ_D. Towards higher values of λ_D, it can be remembered from Figure C.2 that SkC was close to 0. Looking at equation 4.43, it becomes evident that FOM also has to approach zero at these values for λ_D. Next, the FOM seems to decrease exponentially towards a given value for λ_D, before it increases sharply and then again decreases exponentially toward 0. The higher the scalar barrier, the closer together the deviation from 0 will be for the different polarizations. An increase in scalar barrier also seems to make the deviations be at higher λ_D values. The fact that also Figure 4.13 and C.3 look similar support the previous statement that a similar increase in $\frac{\lambda_D}{\lambda_R}$ and $\frac{\lambda_R}{\lambda_D}$ will affect the probabilities of NR and AR equally.

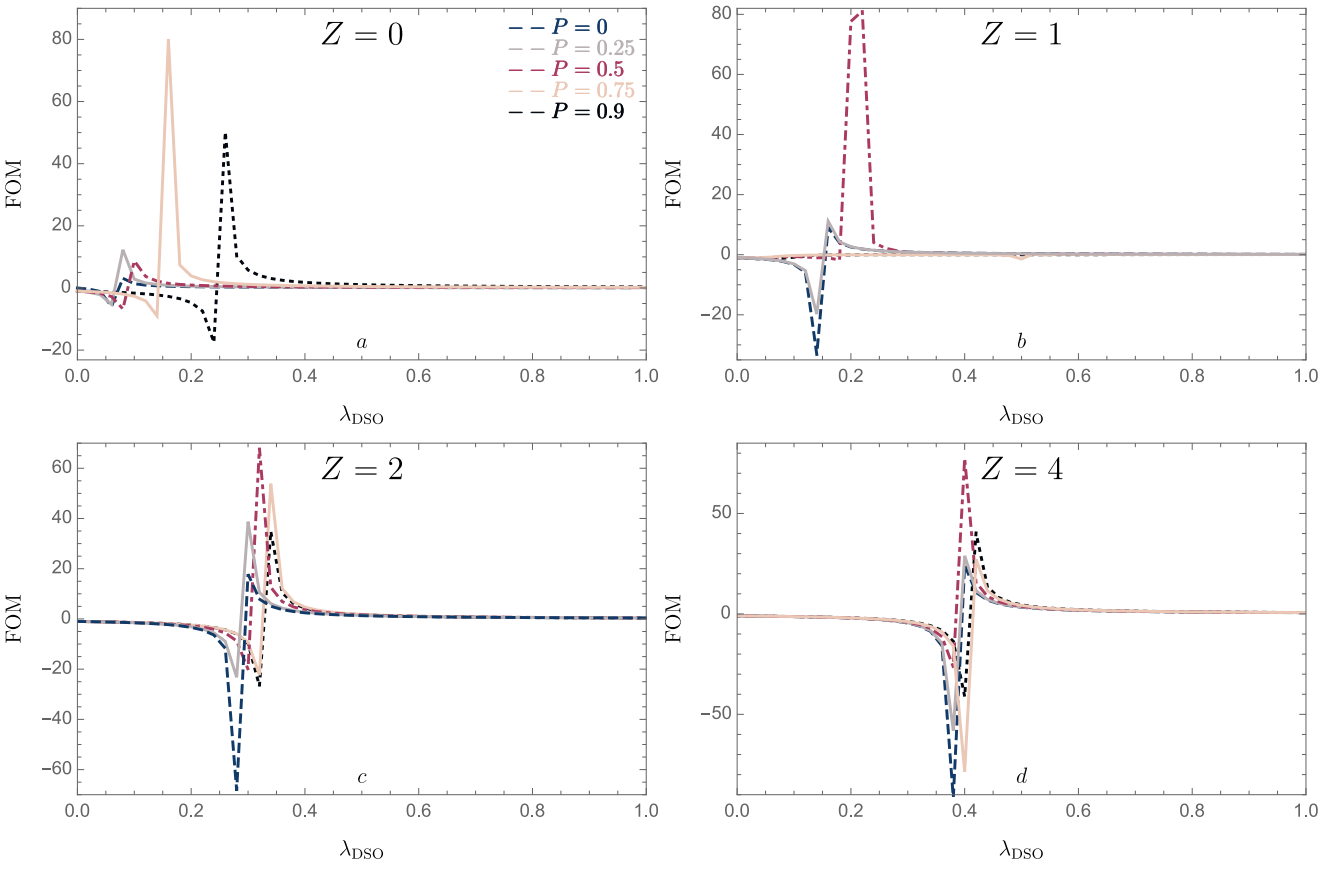

Figure C.3: The FOM for varying scalar barrier strength, Dresselhaus spin-orbit coupling strength and polarization. Here, Rashba spin-orbit coupling strength is $\lambda_R = 1$, the polar angle is $\theta = \frac{\pi}{2}$, the Fermi wave vector is $k_F = 1$, the azimuthal angle is $\phi = 0$, the superconducting gap is $\Delta = 1$, and the normalized temperature $T_d = 0.5$.

Appendix D

Second Boundary Condition

In this appendix, the second boundary condition for the AS junction is derived from equation 5.15 in detail. In case the reader wants to include a scalar barrier, spin orbit interactions or other interface effects, they can easily be added to the calculations in order to find the second boundary condition. First, break down the Hamiltonian into its components,

$$\mathcal{H}_m = \begin{bmatrix} \mu_-^{+J} & \gamma_{\boldsymbol{k}} & \sigma\Delta\Theta(-z) & 0 \\ \gamma_{\boldsymbol{k}} & \mu_-^{-J} & 0 & \sigma\Delta\Theta(-z) \\ \sigma\Delta\Theta(-z) & 0 & \mu_+^{-J} & -\gamma_{\boldsymbol{k}} \\ 0 & \sigma\Delta\Theta(-z) & -\gamma_{\boldsymbol{k}} & \mu_+^{+J} \end{bmatrix} = \begin{bmatrix} 0 & 1 & 0 & 0 \\ 1 & 0 & 0 & 0 \\ 0 & 0 & 0 & -1 \\ 0 & 0 & -1 & 0 \end{bmatrix} \gamma_{\boldsymbol{k}}$$

$$+ \begin{bmatrix} 1 & 0 & 0 & 0 \\ 0 & -1 & 0 & 0 \\ 0 & 0 & -1 & 0 \\ 0 & 0 & 0 & 1 \end{bmatrix} J\Theta(z) + \begin{bmatrix} -1 & 0 & 0 & 0 \\ 0 & -1 & 0 & 0 \\ 0 & 0 & 1 & 0 \\ 0 & 0 & 0 & 1 \end{bmatrix} \mu\Theta(z) + \begin{bmatrix} 0 & 0 & 1 & 0 \\ 0 & 0 & 0 & 1 \\ 1 & 0 & 0 & 0 \\ 0 & 1 & 0 & 0 \end{bmatrix} \Delta\Theta(z) \qquad \text{(D.1)}$$

$$+\begin{bmatrix} -1 & 0 & 0 & 0 \\ 0 & -1 & 0 & 0 \\ 0 & 0 & 1 & 0 \\ 0 & 0 & 0 & 1 \end{bmatrix} \mu_{sc}\Theta(-z).$$

Now, integrate Schrödinger's equation from $-b$ to b,

$$\begin{bmatrix} 0 & 1 & 0 & 0 \\ 1 & 0 & 0 & 0 \\ 0 & 0 & 0 & -1 \\ 0 & 0 & -1 & 0 \end{bmatrix} \int_{-b}^{b} \gamma_{\boldsymbol{k}}\Psi(z)dz + \begin{bmatrix} 1 & 0 & 0 & 0 \\ 0 & -1 & 0 & 0 \\ 0 & 0 & -1 & 0 \\ 0 & 0 & 0 & 1 \end{bmatrix} \int_{-b}^{b} J\Theta(z)\Psi(z)dz +$$

$$\begin{bmatrix} -1 & 0 & 0 & 0 \\ 0 & -1 & 0 & 0 \\ 0 & 0 & 1 & 0 \\ 0 & 0 & 0 & 1 \end{bmatrix} \int_{-b}^{b} \mu\Theta(z)\Psi(z)dz + \begin{bmatrix} 0 & 0 & 1 & 0 \\ 0 & 0 & 0 & 1 \\ 1 & 0 & 0 & 0 \\ 0 & 1 & 0 & 0 \end{bmatrix} \int_{-b}^{b} \sigma\Delta\Theta(z)\Psi(z)dz + \tag{D.2}$$

$$\begin{bmatrix} -1 & 0 & 0 & 0 \\ 0 & -1 & 0 & 0 \\ 0 & 0 & 1 & 0 \\ 0 & 0 & 0 & 1 \end{bmatrix} \int_{-b}^{b} \mu_{sc}\Theta(-z)\Psi(z)dz = \int_{-b}^{b} E\Psi(z)dz.$$

Solving these integrals at the limit where $b \to 0$, one arrive at,

$$\begin{bmatrix} 0 & 1 & 0 & 0 \\ 1 & 0 & 0 & 0 \\ 0 & 0 & 0 & -1 \\ 0 & 0 & -1 & 0 \end{bmatrix} \left(\frac{\partial \Psi^{\sigma}_{S_{AFM}}}{\partial z}|_{z=0^+} - \frac{\partial \Psi^{\sigma}_{F_{AFM}}}{\partial z}|_{z=0^-} \right) = \begin{bmatrix} 0 \\ 0 \\ 0 \\ 0 \end{bmatrix}, \tag{D.3}$$

which can only be true for,

$$\frac{\partial \Psi^{\sigma}_{S_{AFM}}}{\partial z}|_{z=0^+} = \frac{\partial \Psi^{\sigma}_{F_{AFM}}}{\partial z}|_{z=0^-}. \tag{D.4}$$

This is the final expression for the second boundary condition, a result that was expected since no interface effects were included in the calculations for the AS junction.

Bibliography

[1] Alidoust, M. "Proximity Effects and Transport Properties of Nano-Scale Systems with Multiple Broken Symmetries". PhD thesis. Norwegian University of Science and Technology, 2013.

[2] Annunziata, G. et al. Charge and Spin Transport Through a Ferromagnet/Insulator/Unconventional Superconductor Junction, *Physical Review B*, 83 (Mar. 2011), p. 094507. DOI: 10.1103/PhysRevB.83.094507. URL: https://link.aps.org/doi/10.1103/PhysRevB.83.094507.

[3] Aspect, A. and Villain, J. The Birth of Wave Mechanics (1923–1926), *Comptes Rendus Physique*, 18 (Nov. 2017), pp. 583–585. DOI: https://doi.org/10.1016/j.crhy.2017.10.007. URL: http://www.sciencedirect.com/science/article/pii/S1631070517300774.

[4] Bardeen, J., Cooper, L. N., and Schrieffer, J. R. Theory of Superconductivity, *Physical Review*, 108 (Dec. 1957), pp. 1175–1204. DOI: 10.1103/PhysRev.108.1175. URL: https://link.aps.org/doi/10.1103/PhysRev.108.1175.

[5] Bathen, M. E. and Linder, J. Spin Seebeck Effect and Thermoelectric Phenomena in Superconducting Hybrids With Magnetic Textures or Spin-Orbit Coupling, *Scientific Reports*, 7 (Jan. 2017). DOI: https://doi.org/10.1038/srep41409. URL: https://www.ncbi.nlm.nih.gov/pubmed/26239479.

[6] Bell, C. et al. Proximity and Josephson Effects in Superconductor/Antiferromagnetic Nb/$\gamma-Fe_{50}Mn_{50}$ Heterostructures, *Physical Review B*, 68 (Oct. 2003), p. 144517. DOI: 10.1103/PhysRevB.68.144517. URL: https://link.aps.org/doi/10.1103/PhysRevB.68.144517.

[7] Bell, C. et al. Proximity and Josephson Effects in Superconductor/Antiferromagnetic Nb/$\gamma-Fe_{50}Mn_{50}$ Heterostructures, *Physical Review B*, 68 (Oct. 2003), p. 144517. DOI: 10.1103/PhysRevB.68.144517. URL: https://link.aps.org/doi/10.1103/PhysRevB.68.144517.

[8] Bell, L. E. Cooling, Heating, Generating Power, and Recovering Waste Heat with Thermoelectric Systems, *Science*, 321 (Sept. 2008), pp. 1457–1461. DOI: 10.1126/science.1158899. URL: http://science.sciencemag.org/content/321/5895/1457.

[9] Bell, L. E. Cooling, Heating, Generating Power, and Recovering Waste Heat with Thermoelectric Systems, *Science*, 321 (Sept. 2008), pp. 1457–1461. DOI: 10.1126/science.1158899. URL: https://science.sciencemag.org/content/321/5895/1457.

[10] Blonder, G. E., Tinkham, M., and Klapwijk, T. M. Transition from Metallic to Tunneling Regimes in Superconducting Microconstrictions: Excess Current, Charge Imbalance, and Supercurrent Conversion, *Physical Review B*, 25 (Apr. 1982), pp. 4515–4532. DOI: 10.1103/PhysRevB.25.4515. URL: https://link.aps.org/doi/10.1103/PhysRevB.25.4515.

[11] Chang, M. *The Theory of Superconductor*. May 2013.

[12] Conover, E. Skyrmions Open a Door to Next-Level Data Storage, *Science News*, 193 (Feb. 2018). URL: https://www.sciencenews.org/sn-magazine/february-17-2018.

[13] Delft, D. and Kes, P. The Discovery of Superconductivity, *Physics Today*, 63 (Sept. 2010). DOI: 10.1126/science.1223586. URL: https://physicstoday.scitation.org/doi/10.1063/1.3490499.

[14] Demirel, Y. "Chapter 7 - Heat and Mass Transfer". In: *Nonequilibrium Thermodynamics (Third Edition)*. Ed. by Y. Demirel. Elsevier, 2014. DOI: https://doi.org/10.1016/B978-0-444-59557-7.00007-2. URL: http://www.sciencedirect.com/science/article/pii/B9780444595577000072.

[15] Derlet, P. M. Landau-Heisenberg Hamiltonian Model for FeRh, *Physical Review B*, 85 (May 2012), p. 174431. DOI: 10.1103/PhysRevB.85.174431. URL: https://link.aps.org/doi/10.1103/PhysRevB.85.174431.

[16] Dill, K. A. and Bromberg, S. *Molecular Driving Forces*. Taylor & Francis Group, 2011.

[17] Dobrovolskiy, O. V. and Huth, M. Crossover From Dirty to Clean Superconducting Limit in Dc Magnetron-Dputtered Thin Nb Films, *Thin Solid Films*, 520 (July 2012), pp. 5985–5990. DOI: https://doi.org/10.1016/j.tsf.2012.04.083. URL: http://www.sciencedirect.com/science/article/pii/S0040609012005718.

[18] Dogan, E. and Seker, F. The Influence of Real Output, Renewable and Non-Renewable Energy, Trade and Financial Development on Carbon Emissions in the Top Renewable Energy Countries, *Renewable and Sustainable Energy Reviews*, 60 (July 2016), pp. 1074–1085. DOI: https://doi.org/10.1016/j.rser.2016.02.006. URL: http://www.sciencedirect.com/science/article/pii/S1364032116002136.

[19] Donaldson, L. Spintronics Breakthrough Could Lead to Low-Energy Electronics, *Materials Today*, 110 (Dec. 2017), p. 047002. DOI: 10.1103/PhysRevLett.110.047002. URL: https://www.materialstoday.com/electronic-properties/news/spintronics-could-lead-to-lowenergy-electronics/.

[20] Dumitrescu, E. et al. Majorana Fermions in Chiral Topological Ferromagnetic Nanowires, *Physical Review B*, 91 (Mar. 2015), p. 094505. DOI: 10.1103/PhysRevB.91.094505. URL: https://link.aps.org/doi/10.1103/PhysRevB.91.094505.

[21] Dutta, P., Saha, A., and Jayannavar, A. Thermoelectric Properties of a Ferromagnet-Superconductor Hybrid Junction: Role of Interfacial Rashba Spin-Orbit Interaction, *Physical Review B*, 96 (Sept. 2017), p. 115404. DOI: 10.1103/PhysRevB.96.115404. URL: https://arxiv.org/abs/1611.00353.

[22] Feofanov, A. K. et al. Implementation of Superconductor/Ferromagnet/Superconductor π-Shifters in Superconducting Digital and Quantum Circuits, *Nature Physics*, 6 (June 2010), pp. 1657–1660. DOI: https://doi.org/10.1038/nphys1700. URL: https://www.nature.com/articles/nphys1700#supplementary-information.

[23] File, J. and Mills, R. G. Observation of Persistent Current in a Superconducting Solenoid, *Physical Review Letters*, 10 (Feb. 1963), pp. 93–96. DOI: 10.1103/PhysRevLett.10.93. URL: https://link.aps.org/doi/10.1103/PhysRevLett.10.93.

[24] Fitzpatrick, R. *Magnetization*. http://farside.ph.utexas.edu/teaching/em/lectures/node73.html. 2002.

[25] Fu, C. et al. Realizing High Figure of Merit in Heavy-Band p-type Half-Heusler Thermoelectric Materials, *Nature Communications* (Sept. 2015), p. 8144. DOI: 10.1038/ncomms9144. URL: https://www.ncbi.nlm.nih.gov/pmc/articles/PMC4569725/.

[26] Gennes, P. *Superconductivity of Metals and Alloys*. W. A. Benjamin, 1966.

[27] Griffiths, D. *Introduction to Quantum Mechanics*. Prentice Hall, Inc., 1995.

[28] Grigereit, T. E. et al. Observation of Oscillatory Magnetic Order in the Antiferromagnetic Superconductor $HoNi_2B_2C$, *Physical Review Letters*, 73 (Nov. 1994), pp. 2756–2759. DOI: 10.1103/PhysRevLett.73.2756. URL: https://link.aps.org/doi/10.1103/PhysRevLett.73.2756.

[29] Guo, Q., Assoud, A., and Kleinke, H. Improved Bulk Materials with Thermoelectric Figure-of-Merit Greater than 1: Tl10–xSnxTe6 and Tl10–xPbxTe6, *Advanced Energy Materials*, 4 (Oct. 2014), p. 1400348. DOI: 10.1002/aenm.201400348. URL: https://onlinelibrary.wiley.com/doi/abs/10.1002/aenm.201400348.

[30] Halbritter, A., Geresdi, A., and Mihaly, G. Spin Polarized Transport as Measured by Superconducting Andreev Spectroscopy, *Frontiers in Nanoscience and Nanotechnology*, 2 (Dec. 2016). DOI: 10.15761/FNN.1000137. URL: https://www.oatext.com/pdf/FNN-3-137.pdf.

[31] Harris, J. R. Forming Groups with 4 4 Matrices, *The Mathematical Gazette*, 94 (Nov. 2010), pp. 426–429. URL: http://www.jstor.org/stable/25759726.

[32] He, R., Schierning, G., and Nielsch, K. Thermoelectric Devices: A Review of Devices, Architectures, and Contact Optimization, *Advanced Materials Technologies*, 3 (Dec. 2017), p. 1700256. DOI: 10.1002/admt.201700256. URL: https://onlinelibrary.wiley.com/doi/abs/10.1002/admt.201700256.

[33] Högl, P. et al. Magnetoanisotropic Andreev Reflection in Ferromagnet-Superconductor Junctions, *Physical Review Letters*, 115 (Sept. 2015), p. 116601. DOI: 10.1103/PhysRevLett.115.116601. URL: https://link.aps.org/doi/10.1103/PhysRevLett.115.116601.

[34] Hubert, A. and Schäfer, R. *Magnetic Domains: The Analysis of Magnetic Microstructures*. Springer-Verlag Berlin Heidelberg, 1998. DOI: 10.1007/978-3-540-85054-0.

[35] Jong, M. J. M. de and Beenakker, C. W. J. Andreev Reflection in Ferromagnet-Superconductor Junctions, *Physical Review Letters*, 74 (Feb. 1995), pp. 1657–1660. DOI: 10.1103/PhysRevLett.74.1657. URL: https://link.aps.org/doi/10.1103/PhysRevLett.74.1657.

[36] Kalcheim, Y. et al. Inverse Proximity Effect at Superconductor-Ferromagnet Interfaces: Evidence for Induced Triplet Pairing in the Superconductor, *Physical Review B*, 92 (Aug. 2015), p. 060501. DOI: 10.1103/PhysRevB.92.060501. URL: https://link.aps.org/doi/10.1103/PhysRevB.92.060501.

[37] Kalenkov, M. S., Zaikin, A. D., and Kuzmin, L. S. Theory of a Large Thermoelectric Effect in Superconductors Doped with Magnetic Impurities, *Physical Review Letters*, 109 (Oct. 2012), p. 147004. DOI: 10.1103/PhysRevLett.109.147004. URL: https://link.aps.org/doi/10.1103/PhysRevLett.109.147004.

[38] Kawashima, Y. Observation of the Meissner Effect at Room Temperature in Single-Layer Graphene Brought Into Contact with Alkanes, *arXiv e-prints* (Jan. 2018).

[39] Kittel, C. *Introduction to Solid State Physics*. John Wiley & Sons, Inc., 2005.

[40] Kragh, H. Max Planck: The Reluctant Revolutionary, *Physics World*, 13 (Dec. 2000), p. 31. DOI: 10.1088/2058-7058/13/12/34. URL: http://stacks.iop.org/2058-7058/13/i=12/a=34.

[41] Krogen, A. S. "All-Optical Magnetisation Switching in Two-Dimensional Metallic Ferro- and Antiferromagnetic Systems". MA thesis. Norwegian University of Science and Technology, 2018.

[42] Linder, J. and Yokoyama, T. Superconducting Proximity Effect in Silicene: Spin-Valley-Polarized Andreev Reflection, Nonlocal Transport, and Supercurrent, *Physical Review B*, 89 (2014), p. 020504. DOI: 10.1103/PhysRevB.89.020504. URL: https://journals.aps.org/prb/abstract/10.1103/PhysRevB.89.020504.

[43] MacDonald, D. K. C. *Thermoelectricity: An Introduction to the Principles*. Dover Publications, Inc., 2006.

[44] Machon, P., Eschrig, M., and Belzig, W. Giant Thermoelectric Effects in a Proximity-Coupled Superconductor–Ferromagnet Device, *New Journal of Physics*, 16 (July 2014), p. 073002. DOI: 10.1038/nmat4360. URL: http://stacks.iop.org/1367-2630/16/i=7/a=073002.

[45] Machon, P., Eschrig, M., and Belzig, W. Nonlocal Thermoelectric Effects and Nonlocal Onsager Relations in a Three-Terminal Proximity-Coupled Superconductor-Ferromagnet Device, *Physical Review Letters*, 110 (Jan. 2013), p. 047002. DOI: 10.1103/PhysRevLett.110.047002. URL: https://link.aps.org/doi/10.1103/PhysRevLett.110.047002.

[46] Manchon, A. et al. New Perspectives for Rashba Spin–Orbit Coupling, *Nature Materials*, 14 (Aug. 2015). DOI: 10.1103/PhysRevB.25.4515. URL: https://doi.org/10.1038/nmat4360.

[47] Mani, A., Kumary, T. G., and Lin, J. G. Thickness Controlled Proximity Effects in C-Type Antiferromagnet/Superconductor Heterostructure, *Scientific Reports*, 5 (Apr. 2015). DOI: 10.1038/srep12780. URL: https://www.ncbi.nlm.nih.gov/pubmed/26239479.

[48] Marcus, P. M. and Moruzzi, V. L. Stoner Model of Ferromagnetism and Total-Energy Band Theory, *Physical Review B*, 38 (Oct. 1988), pp. 6949–6953. DOI: 10.1103/PhysRevB.38.6949. URL: https://link.aps.org/doi/10.1103/PhysRevB.38.6949.

[49] Matsui, H. et al. Angle-Resolved Photoemission Spectroscopy of the Antiferromagnetic Superconductor $Nd_{1.87}Ce_{0.13}CuO_4$: Anisotropic Spin-Correlation Gap, Pseudogap, and the Induced Quasiparticle Mass Enhancement, *Physical Review Letters*, 94 (Feb. 2005), p. 047005. DOI: 10.1103/PhysRevLett.94.047005. URL: https://link.aps.org/doi/10.1103/PhysRevLett.94.047005.

[50] Naess, K. "Thermoelectric Properties of Ferromagnet - Superconductor Hybrid Junctions". MA thesis. Dec. 2018.

[51] Nolting, W. and Ole ś, A. M. Conduction-Band Structure of a Ferromagnetic Semiconductor, *Physical Review B*, 22 (Dec. 1980), pp. 6184–6195. DOI: 10.1103/PhysRevB.22.6184. URL: https://link.aps.org/doi/10.1103/PhysRevB.22.6184.

[52] Parkin, S. et al. Magnetically Engineered Spintronic Sensors and Memory, *Proceedings of the IEEE*, 91 (May 2003), pp. 661–680. DOI: 10.1109/JPROC.2003.811807. URL: https://ieeexplore.ieee.org/document/1200120.

[53] Sachdev, S. Entangling Superconductivity and Antiferromagnetism, *Science*, 336 (June 2012), pp. 1510–1511. DOI: 10.1126/science.1223586. URL: http://science.sciencemag.org/content/336/6088/1510.

[54] Saleem, M. "The Failure of Classical Physics and the Advent of Quantum Mechanics". In: *Quantum Mechanics*. IOP Publishing, 2015. DOI: 10.1088/978-0-7503-1206-6ch1. URL: http://dx.doi.org/10.1088/978-0-7503-1206-6ch1.

[55] Santra, S. *Phase transitions and critical phenomena*. 1972.

[56] Schrieffer, J. R. *Theory of Superconductivity*. Taylor & Francis Group, 1999.

[57] Service, R. F. Search for Majorana Fermions Nearing Success at Last?, *Science*, 332 (Apr. 2011). DOI: 10.1126/science.332.6026.193. URL: http://science.sciencemag.org/content/332/6026/193.

[58] Shafiei, S. and Salim, R. A. Non-Renewable and Renewable Energy Consumption and CO_2 Emissions in OECD Countries: A Comparative Analysis, *Energy Policy*, 66 (2014), pp. 547–556. DOI: https://doi.org/10.1016/j.enpol.2013.10.064. URL: http://www.sciencedirect.com/science/article/pii/S0301421513010872.

[59] Shankar, R. *Principles of Quantum Mechanics*. Springer, 1994.

[60] Singh, N. The Story of Magnetism: From Heisenberg, Slater, and Stoner to Van Vleck, and the Issues of Exchange and Correlation, *arXiv e-prints* (July 2018). URL: https://arxiv.org/abs/1807.11291.

[61] The National High Magnetic Field Laboratory *Low-Temperature Superconductors*. https://nationalmaglab.org/magnet-development/applied-superconductivity-center/research-areas/low-temperature-superconductivity. 2014.

[62] Timm, C. *Theory of Superconductivity*. TU Dresden, 2016.

[63] Twaha, S. et al. A Comprehensive Review of Thermoelectric Technology: Materials, Applications, Modelling and Performance Improvement, *Renewable and Sustainable Energy Reviews*, 65 (Nov. 2016), pp. 698–726. DOI: https://doi.org/10.1016/j.rser.2016.07.034. URL: http://www.sciencedirect.com/science/article/pii/S1364032116303653.

[64] Usadel, K. D. Generalized Diffusion Equation for Superconducting Alloys, *Physical Review Letters*, 25 (Aug. 1970), pp. 507–509. DOI: 10.1103/PhysRevLett.25.507. URL: https://link.aps.org/doi/10.1103/PhysRevLett.25.507.

[65] Vatanparast, M. "Low-Energy Electronic Properties of Graphene". MA thesis. Norwegian University of Science and Technology, 2013.

[66] Wang, K. L., Alzate, J. G., and Amiri, P. K. Low-Power Non-Volatile Spintronic Memory: STT-RAM and Beyond, *Journal of Physics D: Applied Physics*, 46 (Feb. 2013), p. 074003. DOI: 10.1088/0022-3727/46/7/074003. URL: https://iopscience.iop.org/article/10.1088/0022-3727/46/7/074003/pdf.

[67] Weides, M. et al. Observation of Josephson Coupling Through an Interlayer of Antiferromagnetically Ordered Chromium, *Physical Review B*, 80 (Aug. 2009), p. 064508. DOI: 10.1103/PhysRevB.80.064508. URL: https://link.aps.org/doi/10.1103/PhysRevB.80.064508.

[68] Wolf, S. A. et al. Spintronics: A Spin-Based Electronics Vision for the Future, *Science*, 294 (Nov. 2001), pp. 1488–1495. DOI: 10.1126/science.1065389. URL: https://science.sciencemag.org/content/294/5546/1488.

[69] Yokoyama, T., Linder, J., and Sudbø, A. Heat Transport by Dirac Fermions in Normal/-Superconducting Graphene Junctions, *Physical Review B*, 77 (Apr. 2008), p. 132503. DOI: 10.1103/PhysRevB.77.132503. URL: https://link.aps.org/doi/10.1103/PhysRevB.77.132503.

[70] Young, H. D. and Freedman, R. A. *University Physics with Modern Physics*. Pearson, 2015.

[71] Žuti ć, I., Fabian, J., and Das Sarma, S. Spintronics: Fundamentals and Applications, *Reviews of Modern Physics*, 76 (Apr. 2004), pp. 323–410. DOI: 10.1103/RevModPhys.76.323. URL: https://link.aps.org/doi/10.1103/RevModPhys.76.323.

[72] Zhang, Q. H. et al. Thermoelectric Devices for Power Generation: Recent Progress and Future Challenges, *Advanced Engineering Materials*, 18 (Sept. 2015), pp. 194–213. DOI: 10.1002/adem.201500333. URL: https://onlinelibrary.wiley.com/doi/abs/10.1002/adem.201500333.